Università degli Studi di Cagliari

DOTTORATO DI RICERCA

Progettazione Meccanica

Ciclo XXVIII

Modelling, design and analysis of innovative thermal energy storage systems using PCM for industrial processes, heat and power generation.

ING-IND/09

Author	Arena Simone
PhD coordinator	Prof. Mandas Natalino
Supervisor	Prof. Cau Giorgio

Esame finale anno accademico 2014 – 2015

Acknowledgements

First of all, I would like to thank my supervisor, Prof. Giorgio Cau, for the possibility of undertaking this PhD, and for his support and advice during these three years at the Department of Mechanical, Chemical and Materials Engineering (DIMCM), University of Cagliari, Italy.

I wish to remember Prof. Chiara Palomba, who left us prematurely, for her fundamental support and advices at the beginning my research project.

I would also like to thank my Spanish supervisor, Dr. Loreto Valenzuela, for her help during my stay at the Plataforma Solar de Almeria (Ciemat) - Almeria, Spain.

Another special thanks to Prof. Luisa Cabeza for hosting me in Grea Innovació Cuncurrent, University of Lleida.

Thanks to my colleagues at the Department of Mechanical, Chemical and Materials Engineering, the PSA researcher group and the Grea researcher group, for the wonderful time spent together and for being good friends.

Special thanks to Federica for the love, joy and constant support she give me during this experience.

Last, I am grateful to my family, who has always believed in me, and this has permitted me to be what I am, and therefore to reach this important goal.

Abstract

The topic of this PhD thesis is framed on the study and the analysis of thermal energy storage (TES) systems based on phase change materials (PCM) to be used as a back-up for intermediate temperature applications (up to 250 °C). The work is divided in two part: the first part presents the development of numerical models of the latent heat thermal energy storage (LHTES) devices. Different models are developed by means of a 2D and 3D numerical simulation codes specifically implemented in the COMSOL Multiphysics environment. Design of LHTES requires knowledge of the heat transfer process within them, as well as the phase change behaviour of the PCM used. For simulate the PCM, two approaches are used: the first approach takes only into account heat transfer by conduction during the entire process, also when the PCM is in the liquid phase. In the second, the energy equation considering both heat conduction and natural convection is solved to predict the behaviour of the PCM. Different PCM materials, geometries and configurations of the storage device are considered and tested in order to evaluate the effectiveness of the adopted numerical codes under different working conditions. Finally, the models are validated using experimental data obtained from tests carried out on a double tube heat exchanger with fins and with Rubitherm® RT35 paraffin as PCM. The tests are conducted in the laboratories of the University of Lleida (Spain) by the research group GREA Innovació Concurrent.

The second part of this work concerns the design and implementation of a test rig, specifically built for experimental investigation of heat storage devices in the laboratory for TES technologies of the University of Cagliari. An accurate study and selection of both the test rig layout and all the needed equipment is carried out to perform experimental analysis.

The test bench is composed of an electrical heater, which heats the HTF up to the operating temperature, an air cooler, which simulate the thermal demand during the discharge phase, a HTF circulating pump, two test sections for thermal energy storage systems, and a preliminary TES device which consists in a shell and tube heat exchanger, where the HTF flows in the tubes while the PCM is placed in the shell side. At this stage, the thermal energy storage system, the measuring devices and the data acquisition system are under implementation.

Contents

List of figures

List of Tables

Chapter 1

Introduction

1.1 Motivation and objective

In the last decades, the increase in energy demand, together with a growing awareness of the limitation of emissions of greenhouse gases and pollutants, resulted in a significant impulse to the development of technologies aimed at energy saving and at the production of energy from renewable sources. The Intergovernmental Panel on Climate Change (IPCC) report [1] shows that humankind plays a fundamental role on climate change owing to CO_2 emissions from energy consumption, and that a significant reduction in CO_2 emissions is necessary within next decades. The use of renewable energy sources and increased energy efficiency are the main strategies to reduce the dependency of fossil fuels and CO_2 emissions. However, as it is known, renewable energy sources such as solar and wind energy in particular, are not only characterized by discontinuous availability but are also affected by random variations due to local weather conditions.

In this scenario, the availability of energy storage would be essential allowing a large number of solutions and combination of different technologies from already existing power generation systems [2]. Energy storage not only reduces the mismatch between supply and demand but also improves the performance and reliability of energy systems and plays an important role in conserving the energy. The energy storage could also be used to offset the temporary decreases of production from conventional energy sources, ensuring the expected level of demand, allowing a reduction of the peak and an improvement of the efficiency of the plant, with the result of fuel savings [3]. The different forms of energy that can be stored include mechanical, electrical and thermal energy (Fig. 1.1).

Mechanical	*Electrochemical*	*Electrical*
Pumped Hydro-PHS	Secondary battery Lead-acid/NaS/Li-ion	Capacitor Supercapacitor
Compressed Air-CAES		
	Flow battery Redox flow/Hybrid flow	Superconducting Magnetic-SMES
Flywheel-FES		

Thermochemical	*Chemical*	*Thermal*
Solar fuels Solar hydrogen	Hydrogen Fuel cell/Electrolyser	Sensible/Latent heat storage

Fig. 1.1 - Classification of energy storage technologies by the form of stored energy [4].

The most common mechanical storage systems are pumped hydroelectric storage (PHS) power plants, compressed air energy storage (CAES) and flywheel energy storage (FES) as reported in Table 1.1 [5]. The PHS and CAES technologies can be used for large-scale utility energy storage while flywheels are more suitable for intermediate storage [6].

Table 1.1 - A summary of mechanical energy storage technologies [5].

Technology	Advantages	Disadvantages
PHS	Mature technology, high energy and power capacity, least cost for large-scale power, long life.	Requires special sites for upper and lower water reservoirs, high capital cost, long construction time
CAES	Mature technology, high energy and power capacity, least cost for large-scale power, long life.	Requires special geological sites, high capital cost, long construction time, need gas fuel input
FES	High power density, flat voltage profile, better life cycle than batteries	Low energy density, short term power, large standby losses high initial cost

Electrical Energy Storage (EES) refers to a process of converting electrical energy from a power network into a form that can be stored for converting back to electrical energy when needed. The use of batteries is an option for storing the electrical energy. Potential applications of batteries are utilization of off-peak power, load levelling, and storage of electrical energy generated by wind turbine or photovoltaic plants. The most common type of storage batteries is the lead acid and Ni–Cd [6], but for medium and large scale stationary applications new technologies are available, such as nickel–metal hydride (Ni-MH) and lithium-ion (Li-ion) batteries. The flow batteries, as shown in Fig. [7], are a form of a battery in which the electrolyte contains one or more dissolved electro-active species flowing through a power cell/reactor in which the chemical energy is converted to electricity.
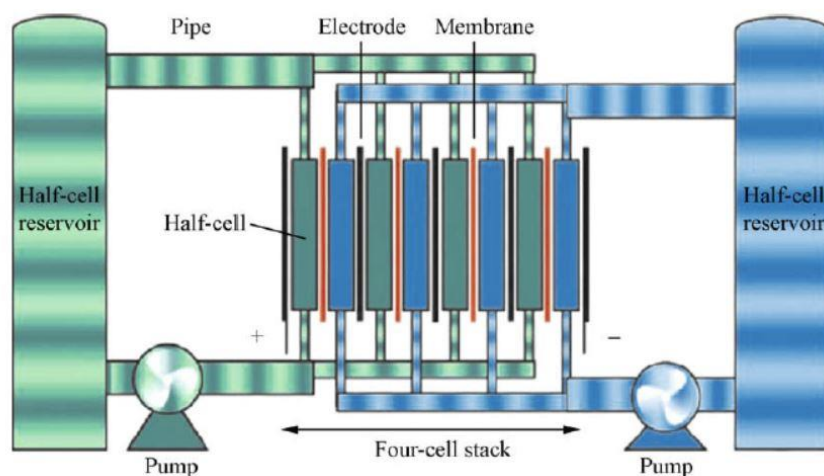
Fig. 1.2 - Schematic of flow battery [7]

Additional electrolyte is stored externally, generally in tanks, and is usually pumped through the reactor cells. The reaction is reversible allowing the battery to be charged, discharged and recharged [7]. The most common type of flow battery is zinc–bromine (ZnBr). A summary of battery storage technologies is shown in Table 1.2 [5].

Table 1.2 - Summary of battery storage technologies [5].

Technology	Advantages	Disadvantages
NaS	High energy and power density, relatively matured, high efficiency and excellent life cycle	High initial cost, safety concerns
ZnBr	High energy and power density, flat voltage profile	Relatively new and untested
Regenerative zinc air Li ion	High energy and power density	Relatively new and untested
Li ion	High energy and power density, long life, high efficiency	High initial cost, requires sophisticated management (balancing and charge control electronics)
VRB	Relatively high energy and power density, easily upgradeable	Not yet proven for cycle life or maintenance cost, relatively expensive
Lithium metal polymer batteries	High energy and power density, relatively tolerant to temperature extremes	Requires balancing and charge control electronics, high initial cost, relatively untested
Vented Ni-Cg	Mature and well known, high efficiency high energy and power density, better lifecycle than lead acid, relatively tolerant to temperature extremes	Float effetc makes capacity testing difficult, more expensive than lead acid, toxic components (cadmium), low cell voltage
NiMH	Less toxic than Ni-Cd, mature technology, high energy and power density, better cycle life than lead acid	Float effect makes capacity testing difficult, more expensive than lead acid, low cell voltage, intolerant of temperature extremes
Valve regulated Pb acid	Low maintenance, low initial cost	Low life, intolerant of temperature extremes
Vented Pb acid	mature and well known, low cost, high reliability and efficiency	poor low temperature performance, high maintenance cost, low energy density and cycle life, can't handle temperature extremes

Thermal energy storage can be based on a change in internal energy of a material as sensible heat, latent heat, thermochemical or combination of these. In the first case, the storage is based on the temperature change of a liquid or a solid material. In the second case, thermal energy is stored as latent heat during a phase transition. The third type uses an endothermic chemical reaction, where the energy associated with a reversible reaction is required for the dissociation of the chemicals [8].

The main objective of this PhD research project is the modelling, the design and the analysis of TES devices based on latent heat storage for renewable energy and other non programmable

energy sources, industrial processes and heat and power generation for intermediate temperature applications (150-250 °C).

Real applications of Latent Heat Thermal Energy Storage (LHTES) systems for the temperature range chosen are typically used in solar technologies associated with Organic Rankine Cycle (ORC) (e.g. REELCOOP EU/FP7 project), or in general in concentrating small-medium scale solar power (CSP). In the same temperature range, PCM materials are also used in various types of industrial applications such as in solar cooling systems with absorption chiller [9], related to fuel cell PAFC or heat recovery in metal hydrides hydrogen storage systems. Other application areas are in the food, beverage, transport equipment, textile, machinery, pulp and paper industries and drying of agricultural products, where roughly 60% of the heating needs is required temperatures below 250°C [10] [11]. Temperature range for reported industrial applications are listed in Table 1.3.

Table 1.3 - Heat demand for different industrial processes by sectors and temperature ranges

Industry	Process	Temperature [°C]
Dairy	Pressurization	60-80
	Sterilization	100-120
	Drying	120-180
	Concentrates	60-80
	Boiler feed water	60-90
Tinned Food	Sterilization	110-120
	Pasteurization	60-80
	Cooking	60-90
	Bleaching	60-90
Textile	Bleaching, Dyeing	60-90
	Drying, Degreasing	100-120
	Dyeing	70-90
	Fixing	160-180
	Pressing	80-100
Paper	Cooking, Drying	60-80
	Boiler feed water	60-90
	Bleaching	130-150
Chemical	Soap	200-250
	Synthetic rubber	150-200
	Processing heat	120-180
	Pre-heating water	60-90
Meat	Wash, Sterilization, Cleaning	60-90
	Cooking	90-100
Tinned food	Sterilization	60-70
	Cooking	90-100
Beverages	Washing, Sterilization	60-80
	Pasteurization	60-70
Flours & by-prod.	Sterilization	60-80
Timber by-products	Thermodiffusion beams	80-100
	Drying	60-100

	Pre-heating water	60-90
	Preparation pulp	120-170
Automobile	Painting	160-220
	Drying	60-100
	Cooking	60-90
Bricks and blocks	Curing	60-140
Plaster	Calcinating	140-160
	Curing plasterboard	230-250
Glass	Sheets	100-150
	Drying fibre-glass	110-130
Plastics	Preparation	120-140
	Distillation	140-150
	Saparation	200-220
	Extension	140-160
	Drying	180-200
	Blending	120-140

Source: GESA Research Group, 1988

Suitable materials for accomplishing this task are Phase Change Materials (PCM). A Phase Change Material is a material that change its phase at a certain temperature storing or releasing large amount of energy called latent heat. The latent heat change is usually much higher than the sensible heat change for a given medium, which is related to its specific heat. Solar energy applications require large TES capacities in order to cover the lack of daytime radiation for meteorological reasons or simply overnight. This capacity is commonly achieved by sensible heat storage systems. A valid alternative is offered by latent heat storage systems, where thermal energy is stored as latent heat in substances undergoing a phase transition, for example, the heat of fusion in the solid–liquid transition. The main advantages of LHTES systems are high thermal energy storage capacities per unit mass compared to those of sensible heat systems, and a small temperature range of operation since the heat interaction occurs at approximately constant temperature.

This work is based on two parts: the first part is the study and the analysis of numerical models in order to simulate the transient behaviour of the PCM-TES, to predict the energy balance in space and time and the TES overall performances. The second part concerns the design and the implementation of a test rig specifically built for experimental investigation of heat storage devices. The test rig, implemented in the laboratory for TES technologies of the Department of Mechanical, Chemical and Materials Engineering (DIMCM) of the University of Cagliari, can be used not only to validate all the developed numerical models, but also to carry out a considerable research activity in the field of thermal energy storage based on modeling, control and testing of innovative TES systems for industrial applications. Main objectives of this research activity will be the performance evaluation of PCM-TES prototypes with respect to energy stored/released, time and efficiency during repeated cycles of charge/discharge, the analysis on different materials, geometries and heat transfer enhancement techniques in order to optimize the entire process.

The numerical models implemented in COMSOL Multiphysics are used to simulate latent heat storage systems with different geometries and different working materials. The numerical analysis is based on development of three and two-axisymmetric dimensional models, where energy

equation is used in accordance with the apparent heat capacity formulation to solve and model the phase transition of a PCM material chosen.

Finally, because of the test rig of the DIMCM has not yet been completed, the numerical models proposed have been validated by comparison with experimental results carried out with the experimental facilities of the GREA Innovació Concurrent situated in the University of Lleida (Spain). The result demonstrates its validity and feasibility to simulate real application in thermal energy storage with PCM.

1.2   Overview of the thesis

This Thesis is structured in six main chapters and a concluding chapter subdivided in paragraphs for each topic.

A brief description of each chapter is given in the following:

- **Chapter 2:** A general overview of the different methods of thermal energy storage is presented with respect to their characteristics, focusing the attention to the latent heat thermal storage systems. Furthermore, a comparison between these different methods is also presented, in order to evaluate the advantages and disadvantages of the latent heat storage with respect to the other technologies.

- **Chapter 3:** A summary of the different classes of PCM materials is reported with respect to their most important properties, advantages and disadvantages. Furthermore a description of the basic requirements to use them as phase change material is discussed. In the last part of this chapter, various method to increase thermal conductivity of PCM are also discussed.

- **Chapter 4:** The numerical models used to simulate the latent heat thermal energy storage systems are introduced. A description of equations, geometries, configurations and materials used is presented. Different models are investigated using two approaches to model the PCM during transition process: in the first heat transfer only by conduction is considered, in the second heat transfer by conduction and natural convection are considered. Finally, the numerical results are compared with an experimental test in order to validate the accuracy of the models.

- **Chapter 5:** The design of a test rig to investigate thermal energy storage systems within the laboratory of the Department of Mechanical, Chemical and Material of the University of Cagliari is presented. A description of the facility components and of the latent heat storage device is also reported.

- **Chapter 6:** The study of a real application of latent heat thermal energy storage system in the research center Plataforma Solar de Almeria (Spain) are reported. Description of the pilot plant equipments and operation mode is reported. A simplified numerical model to

simulate the dynamic behaviour of the entire system during the charge and discharge process is presented.

- **Chapter 7:** The main conclusions and the possible future development of this research are discussed.

1.3   Publication

Some of the topics discussed in this Thesis have been already published in international journal, and presented at national and international conferences.

International Journal Papers:

1. Arena S., Cau G., Palomba C., *CFD Simulation of Melting and Solidification of PCM in Thermal Energy Storage Systems of Different Geometry*, Journal of Physics: Conference Series 655.
2. Migliari L., Arena S., *Thermal Energy Losses During Night, Warm-Up and Full-Operation Periods of a CSP Solar Field Using Thermal Oil*, Energy Procedia 82 (1002-1008) doi:10.1016/j.egypro.2015.11.858

National and International Conferences:

1. Arena S., Cau G., Palomba C., *Development and Implementation of a 3D Numerical Code for Designing and Predicting Performances of PCM Thermal Energy Storage Systems*, Eurotherm Seminar n°99 - Advances in Thermal Energy Storage, Lleida, Spain 2014.
2. Arena S., Casti E., Cascetta M., Serra F., Cau G., *Performance Analysis of Thermal Energy Storage (TES) Systems based on Sensible and Latent Heat for Concentrated Solar Power (CSP) Applications*, Ricerca in Vetrina, Alghero, Italy 2015.

Chapter 2

Methods for thermal energy storage

2.1 Introduction

Thermal energy storage (TES) systems allow the storage of heat or cold for later use. The main use of TES are in all the applications where exist a mismatch between energy production and use like in the case of renewable energies which are by nature intermittent and whose availability is further reduced by weather perturbation. Solar energy is available only during the day, and hence, its application requires an efficient thermal energy storage so that the excess heat collected during sunshine hours can be stored for later use during the night. Similar problems occur in heat recovery systems and industrial processes where the waste heat availability and utilization periods are different, requiring some thermal energy storage. Also, electrical energy consumption varies significantly during the day and night, especially in extremely cold and hot climate countries where the major part of the variation is due to domestic space heating and air conditioning. Such variation leads to an off-peak period, usually after midnight until early morning. Accordingly, power stations have to be designed for capacities sufficient to fulfil the peak load. Otherwise, very efficient power distribution would be required. Better power generation management can be carried out if some of the peak load could be shifted to the off-peak load period, which can be achieved by energy storage. Hence, the successful application of load shifting depends to a large extent on the method of energy storage adopted [12]. Generally, it is possible to divide thermal storage systems in active and passive systems. An active storage system contains a mechanically assisted component for enabling the heat transfer between the system and the heat source. Therefore, this systems are characterized by forced convection heat transfer into the storage material that circulates through a heat exchanger, a solar receiver or a steam generator. In a passive storage system, the heat transfer between the system and the heat source occurs by means of natural convection or buoyancy forces (due to density gradient) without the assistance of any external devices [13]. Active storage systems can be divided into direct and indirect systems. In the direct systems, the heat transfer fluid (HTF) is used also as storage medium, while in the indirect systems, a second medium is used for storing the heat [14]. Figure 2.1 reports some TES system configurations classified as active and passive storage systems.
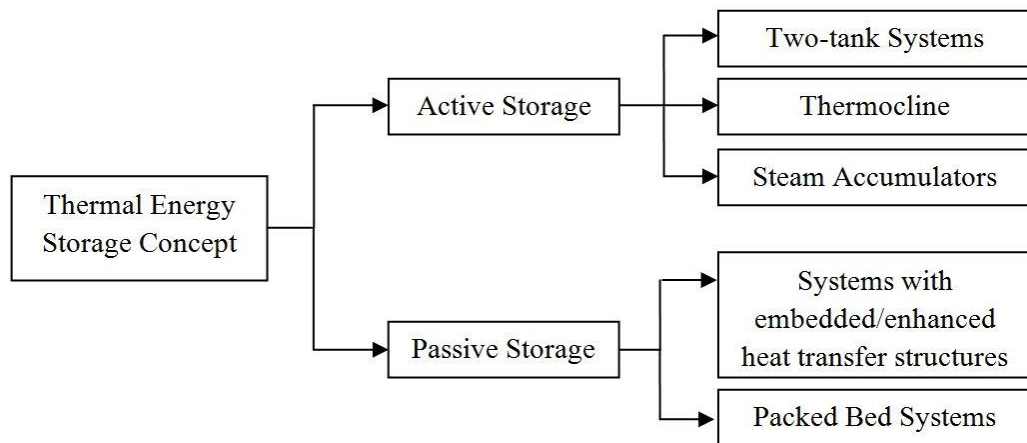
Fig. 2.1- Examples of TES system configurations classified as active and passive storage systems [15]

Thermal energy can basically be classified according to the way heat is stored: as sensible heat, latent heat or chemical energy (Fig. 2.2).
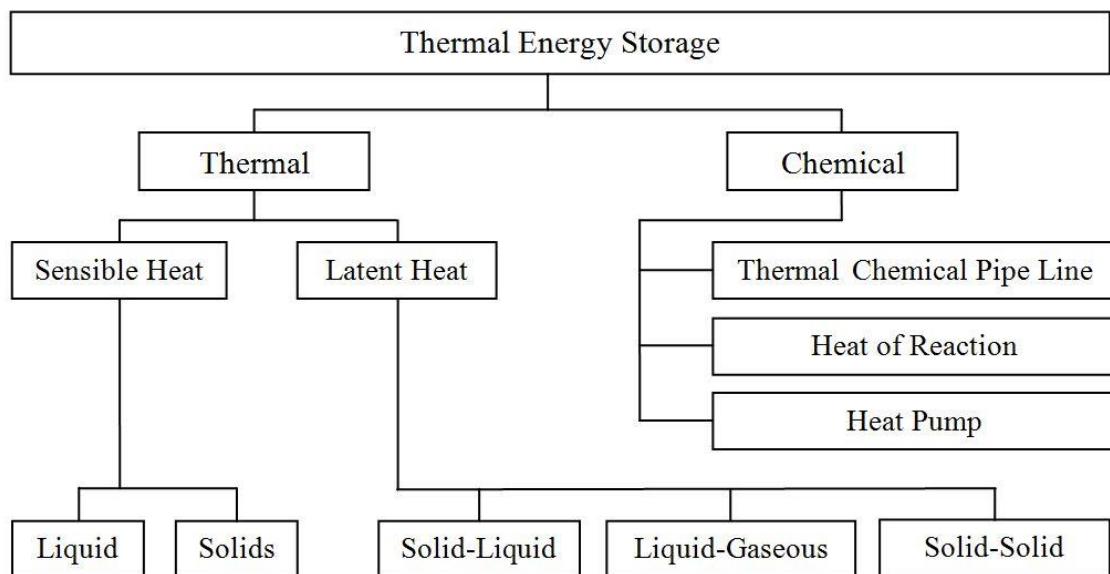
Fig. 2.2 - Methods of thermal energy storage

Each of these types presents a sequential process of charge, storage and discharge giving a complete storage cycle as reported in Figure 2.3.
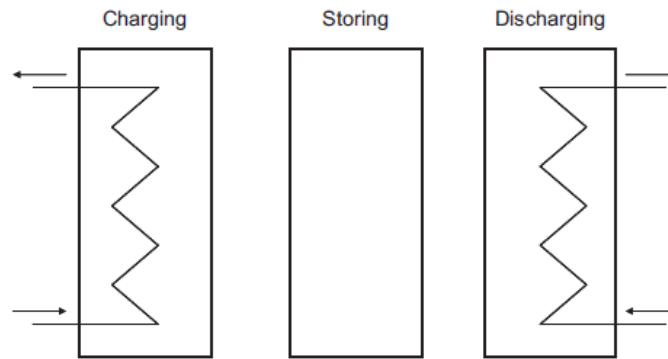
Fig. 2.3 - TES complete storage cycle.

2.2   Sensible Heat Storage

In sensible heat storage systems (SHSS), thermal energy is stored by raising the temperature of a solid or liquid media. Sensible heat storage is by far the common method for heat storage, for example, hot water heat storage is used for domestic heating and domestic hot water in every household. The amount of energy stored is given by the relation:

$$Q = \int_{T_i}^{T_f} mC_p dT = m\overline{C_p}(T_f - T_i) \tag{2.1}$$

where Q is the amount of heat stored in the material, m is the mass of storage material, $\overline{C_p}$ is the mean specific heat of the material evaluated in the operative temperature range and T_i and T_f are the initial and final temperature of the process respectively.

A large number of materials are available in any required temperature range therefore, the storage material is usually selected according to its heat capacity and the available space for storage. Gases have very low volumetric heat capacity and therefore are not used for sensible heat or cold storage. Table 2.1 reports some common materials used in SHSS [16].

Table 2.1 - Typical materials used in sensible heat storage systems

Material	Density [kg/m³]	Specific heat [J/kg·K]	Volumetric thermal capacity [MJ/m³·K]
Clay	1458	879	1.28
Brick	1800	837	1.51
Sandstone	2200	712	1.57
Wood	700	2390	1.67
Concrete	2000	880	1.76
Glass	2710	837	2.27
Aluminium	2710	896	2.43

Iron	7900	452	3.57	
Steel	7840	465	3.68	
Gravelly earth	2050	1840	3.77	
Magnetite	5177	752	3.89	
Water	988	4182	4.17	

In Table 2.2 are presented some materials mostly used in CSP storage applications [17].

Table 2.2 - Properties of materials used in CSP plants

Material	Density [kg/m³]	Specific heat [J/kg·K]	Thermal conductivity [W/mK]	Cost [€/kg]	Cost [€/kWh] ΔT=100 °C
Molten Salt	900-2600	1500	0.15-2	0.63	14
Colafite	3120	800-1034	1.4-2.1	0.01	0.4
Castable ceramics	3500	866	1.35	4.5	188
High temperature concrete	2750	916	1	0.08	3

Water appears to be the best available liquid SHSS because it is cheap and has a high specific heat and volumetric thermal capacity. However above 100 °C, materials such as oils, molten salts and liquid metals are preferred since water should be pressurized. For air heating applications rock or metal bed type storage materials are used [6].

2.3 Latent Heat Storage

Latent heat storage is based on the heat absorption and release when a storage material undergoes a phase change. PCM can store 5–14 times more heat per unit volume than sensible heat storage materials such as water, masonry, or rock. Phase change can occur in different forms: solid–solid, solid–liquid, solid–gas, liquid–gas. Solid–liquid transitions are an economically attractive option for use in thermal energy storage systems. In fact these transformations have comparatively smaller latent heat than liquid–gas, but involve only a small change (of about 10% or less) in volume. The storage capacity of the LHTES system with a solid-liquid process is given by:

$$Q = m \left[\int_{T_i}^{T_m} C_{p,s} dT + \lambda + \int_{T_m}^{T_f} C_{p,l} dT \right] \tag{2.2}$$

The first term of the second member is the sensible heat of the solid phase, λ represents the specific latent heat and, finally, the third term is the sensible heat of the liquid phase. In the Equation 2.2, $C_{p,s}$ and $C_{p,l}$ are specific heat of solid and liquid phase respectively and T_m is the melting temperature of the material.

With respect to other techniques, latent heat thermal energy storage is particularly attractive due to both its ability to provide high-energy storage density and its characteristic to store heat at constant temperature corresponding to the phase-transition temperature (Fig 2.4).
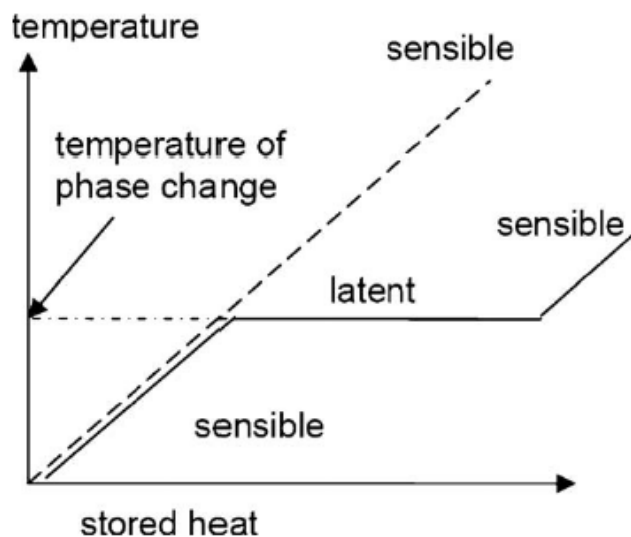
Fig. 2.4- Comparison between sensible and latent heat.

A large number of PCM are known to melt with a heat of fusion in any range of interest. However, for their employment these materials must exhibit certain desirable thermodynamic, kinetic and chemical properties. In Chapter 3 a list of different classes of PCM materials is reported with respect to their important properties, advantages and disadvantages.

2.4   Thermochemical Heat Storage

Thermochemical TES systems use an endothermic chemical reaction, where the energy associated with a reversible reaction is required for the dissociation of the chemicals [8]. In this case, the heat stored is given by Equation 2.3:

$$Q = a_r m \Delta h_r \tag{2.3}$$

where a_r is the extent of conversion, m is the amount of storage material and Δh_r is the endothermic heat of reaction. Thermochemical materials have higher energy densities relative to PCMs and sensible storage media [14]. Because of higher energy density, thermochemical TES systems can provide more compact energy storage relative to latent and sensible TES. This attribute is particularly beneficial where space for the TES is limited or valuable [18]. Drawbacks include complexity and high cost [19]. Thermochemical energy is divided in two different systems: chemical reactions and sorption systems. In chemical reactions storage systems, high

energy storage density and reversibility is required to the materials [14]. Usually TES based on chemical reaction have better energy storage performance efficiency than sensible and latent heat storage systems. These systems are used as storage at high temperature (more than 400 °C) and the main reaction used are the carbonation reaction, ammonia decomposition, metal oxidation reactions and sulfur cycles [20].

In sorption systems, heat is stored by separation of substances. To recover heat, the substances are recombined. This technologies are divided into closed and open sorption storage systems as reported in figure 2. [21].

(a)   (b)
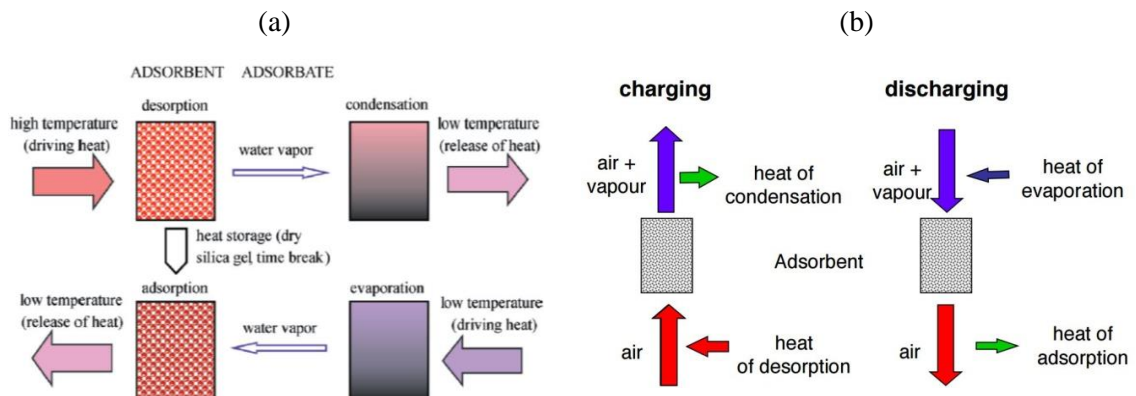
Fig. 2.5- Scheme of closed (a) and open (b) sorption storage systems [21]

The first configuration takes the sorbate from the ambient, while in the second, the sorbate remains within the system (not only water can be used but also other liquids such as ammonia or methanol), and only the evaporation heat is taken from the ambient. The most common sorbents are reported in figure 2.4.
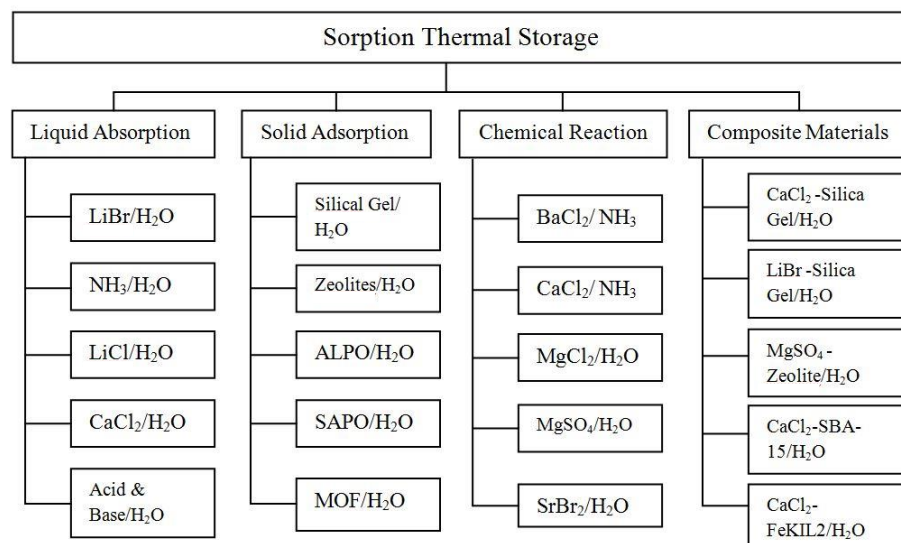
Fig. 2.6 - Sorption thermal storage methods and materials [9]

2.5   Comparison of TES types

A quantitatively comparison of the different thermal energy storage technologies is reported in table 2.3, considering a range of relevant performance parameters and factors. It is evident that the various technologies have different operating characteristics, advantages and disadvantages. For different applications, different TES can be the most suitable choice.

Table 2.3 - Comparison of different thermal energy storage systems

	Sensible TES	*Latent TES*	*Thermochemical TES*
Temperature range	Up to: 50 °C (Aquifers and ground storage) 110 °C (Water tanks) 300 °C (Sand-rock-mineral oil) 400 °C (Siliconic oil) 400 °C (Concrete) 500 °C (NaCl, solid) 700 °C (Cast steel) 1200 °C (Magnesia fire bricks)	-100÷0 °C (Water-salt solutions) -50÷0 °C (Clathrates) -20÷100 °C (Paraffins) -20÷80 °C (Salt hydrates) 20÷450 °C (Sugar alcohols) 120÷300 °C (Nitrates) 150÷400 °C (Hydroxides) 350÷750 °C (Chlorides) 400÷800 °C (Carbonates) 700÷900 °C (Fluorides)	180 °C (Iron carbonate) 200÷300 °C (Metal hydrides) 250÷400 °C (Magnesium oxide) 400÷500 °C (Ammonia) 800÷900 °C (Calcium carbonate) 500÷1000 °C (Methane/water) 2000÷2500 °C (Metal oxides Zn and Fe)
Energy density			
Volumetric density	Small ~ 50 kWh/m^3 of material	Medium ~ 100 kWh/m^3 of material	High ~ 500 kWh/m^3 of material
Gravimetric density	Small ~ 0.02-0.03 kWh/m^3 of material	Medium ~ 0.05-1 kWh/m^3 of material	High ~ 0.5-1 kWh/m^3 of material
Storage period	Limited (thermal losses)	Limited (thermal losses)	Theoretically unlimited
Lifetime	Long	Often limited due to storage material cycling	Depends on reactant degradation and side reactions
Technology status	Industrial scale	Pilot scale	Laboratory scale
Advantages	Low cost Reliable Simple application with available materials	Medium storage density Small volumes Short distance transport possibility	High storage density Low heat losses (storage at ambient temperature) Long distance transport possibility High compact energy storage
Disadvantages	Significant heat loss over	Low heat conductivity	High capital costs

time (depending on level of insulation)	Corrosivity of materials	Technically complex
Large volume needed	Significant heat loss (depending on level of insulation)	

Chapter 3

Phase Change Materials (PCM)

3.1 Introduction

Thermal energy storage systems based on phase change materials are considered to be an efficient alternative to sensible thermal storage systems. Furthermore, these systems have high energy density compared to sensible heat storage systems. As said before PCM include the solid-solid, the solid-liquid, the solid-gas and the liquid-gas type.

In solid–solid transitions, heat is stored during the change from one crystalline to another. These transitions generally have small latent heat and small volume changes than solid–liquid transitions. Solid–solid PCM offer the advantages of less strict container requirements and greater design flexibility. Solid–gas and liquid–gas transition have higher latent heatof vaporization but their large change in volume on phase transition are associated with the containment problems and restricts their application in TES. Solid–liquid transformations have comparatively smaller latent heat than liquid–gas, but involve only a small volume change (of order of 10% or less). For this reasons, solid–liquid transitions is considered the most interesting and economically attractive option to be applied in thermal energy storage systems.

The PCM to be used in the design of thermal-storage systems require desirable thermo-physical, kinetics chemical and economical properties [6][16][22] thus, generally, a material is not able to achieve all these requirements.

a) Thermal requirements
   - Suitable phase-transition temperature to assure storage and release of heat at the correct temperature for each application.
   - High latent heat of transition to achieve a large storage density in order to minimize the physical size of the heat store.
   - High thermal conductivity to assure storage and release of latent heat in a short time during charging and discharging operation.

b) Physical requirements
   - High density to minimize the size of storage container.
   - Small volume change to reduce the containment problem.
   - Low vapor pressure to reduce the containment problem.
   - Favorable phase equilibrium to assure the stability of the storage capacity during cycles.

c) Kinetic requirements
   - No subcooling to guarantee that melting and solidification take place at correct temperature transition range. The subcooling happens when a PCM do not solidify immediately upon cooling below the melting temperature; in this case the crystallization starts only after a temperature well below the melting temperature is reached. The effect of subcooling involves the reduction of the temperature below the phase change temperature to start crystallization and to release the latent heat stored in the material. If nucleation does not happen at all, the latent heat is not released at all and the material only stores sensible heat [16].
   - Good crystallization rate.

d) Chemical requirements
   - Chemical stability to avoid degradation after a large number of cycles.
   - Compatibility with other materials to avoid problems of corrosion with container.
   - Non toxic, non flammable and non explosive behaviour for safety and environmental impact.

e) Economics requirements
   - Low price to be competitive with other thermal storage technologies.
   - Good recyclability for environmental and economic reasons.

3.2 Classification of PCM

PCM materials can be divided in three groups as reported in figure 3.1.
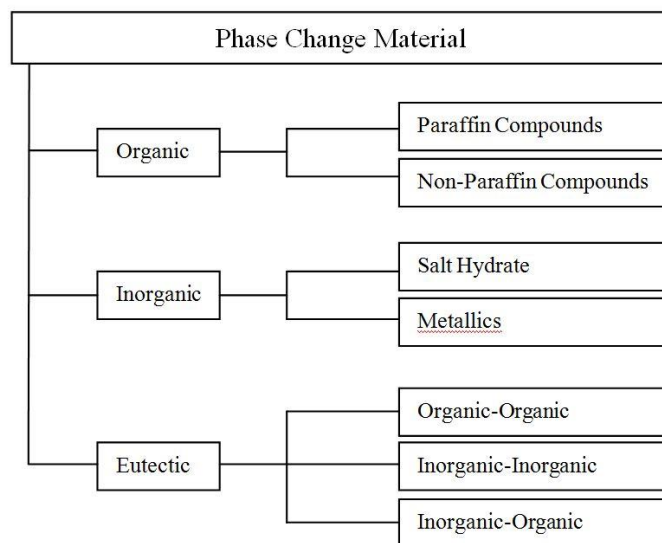
Fig. 3.1- Classification of PCM

Figure 3.2 shows common classes of PCM related with the melting enthalpy and the melting temperature [16].
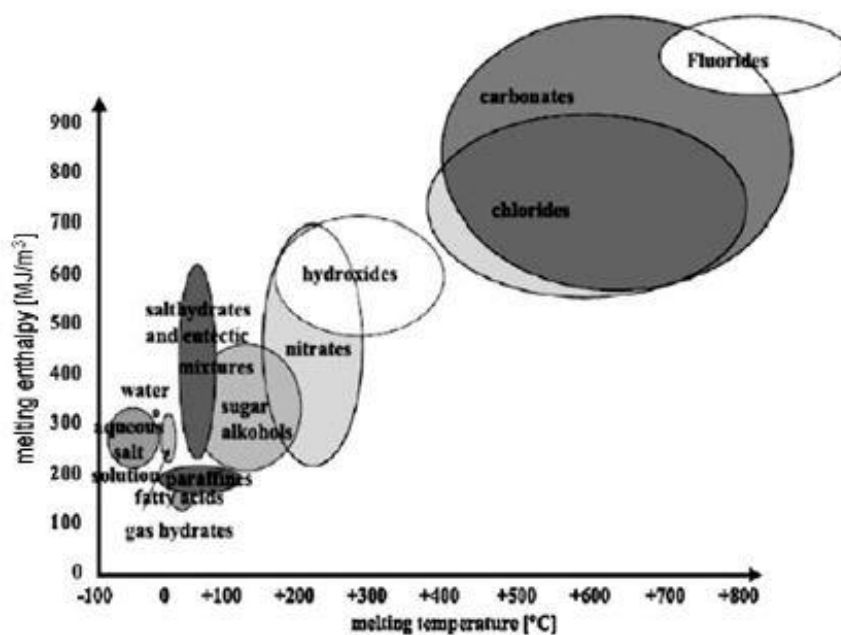
Fig. 3.2 - Classes of PCM related with melting enthalpy and melting temperature[16]

A short overview on properties, advantages and disadvantages of the different classes of PCM materials is given below.

3.2.1 Organic PCM

Organic materials are divided into two groups: paraffin and non-paraffins.

Paraffins

Paraffin wax is the most common organic PCM and consists of a mixture of mostly straight chain *n*-alkanes CH3-(CH2)-CH3. Generally the higher the average length of the hydrocarbon chain, the higher the latent heat of fusion and the melting temperature. Paraffins are safe, reliable, quite cheap and non-corrosive; others advantages are chemical stability, absence of segregation and sub-cooling, good nucleating and constant thermo-physical properties. However, this material shows some disadvantages such as: low thermal conductivity, high temperature transition range, non compatible with plastic container, high volume change during solid-liquid transition and often is flammable. Table 3.1 reports examples of paraffins used as PCM.

Table 3.1 - Example of paraffins that have been investigated as PCM [7]

Material	Melting temperature [°C]	Melting enthalpy [kJ/kg]	Thermal conductivity [W/m·K]	Density [kg/m³]
n-Tetradecane $C_{14}H_{30}$	6	230	-	760 (liquid, 20°C)
			0.21 (solid)	-
n-Pentadecane $C_{15}H_{32}$	10	212	-	770 (liquid, 20°C)
			-	-
n-Hexadecane $C_{16}H_{34}$	18	210,238	-	760 (liquid, 20°C)
			0.21 (solid)	-
n-Heptadecane $C_{17}H_{36}$	19	240	-	776 (liquid, 20°C)
			-	-
n-Octadecane $C_{18}H_{38}$	28	200, 245	0.148 (liquid, 40°C)	774 (liquid, 70°C)
			0.358 (solid, 25°C)	814 (solid, 20°C)
n-Eicosane $C_{20}H_{42}$	38	283	-	779
			-	-
n-Triacontane $C_{30}H_{62}$	66	-	-	775
			-	-
n-Tetracontane $C_{40}H_{82}$	82	-	-	-
			-	-
n-Pentacontane $C_{50}H_{102}$	95	-	-	779
			-	-
Polyethylene C_nH2_{n+2} n up to 10000	110	200	-	-
			-	870-940 (solid, 20 °C)

Non-Paraffins

The non-paraffin materials are fatty acids, esters, glycols and alcohols and represent the largest category of organic PCM. These materials are flammable and should not be exposed to excessively high temperature, flames or oxidizing agents. Fatty acids have high heat of fusion values comparable to that of paraffin's and also present good cycle stability and no subcooling. The disadvantages are corrosivity, toxicity, instability at high temperature and the cost (2-2.5 times than paraffins). Sugar alcohols have melting temperatures in range between 90°C to 200 °C, present high specific melting enthalpies per unit volume but also subcooling. Some non-paraffins are reported in Table 3.2 (fatty acids), in Table 3.3 (sugar alcohol) and in Table 3.4 (glycols).

Table 3.2 - Examples of fatty acids that have been investigated as PCM [7]

Material	Melting temperature [°C]	Melting enthalpy [kJ/kg]	Thermal conductivity [W/m·K]	Density [kg/m³]
Caprylic acid $CH_3(CH_2)_6COOH$	16	149	0.149 (liquid, 38°C) -	901 (liquid, 30°C) 981 (solid, 13°C)
Capric acid $CH_3(CH_2)_8COOH$	32	153	0.149 (liquid, 40°C) -	886 (liquid, 40°C) 1004 (solid, 24°C)
Lauric acid $CH_3(CH_2)_{10}COOH$	42-44	178	0.147 (liquid, 50°C)	870 (liquid, 50°C) 1007 (solid, 24°C)
Myristic acid $CH_3(CH_2)_{12}COOH$	58	186,204	- 0.17 (solid)	861 (liquid, 55°C) 990 (solid, 24°C)
Palmitic acid $CH_3(CH_2)_{14}COOH$	61,64	185,203	- -	850 (liquid, 65°C) 989 (solid, 24°C)

Table 3.3 - Examples of sugar alcohols that have been investigated as PCM [7]

Material	Melting temperature [°C]	Melting enthalpy [kJ/kg]	Thermal conductivity [W/m·K]	Density [kg/m³]
Xylitol $C_5H_7(OH)_5$	94	263	- -	- 1500 (solid, 20°C)
D-Sorbitol $C_6H_8(OH)_6$	97	185	- -	- 1520 (solid, 20 °C)
Erythritol $C_4H_6(OH)_4$	120	340	0.326 (liquid, 140 °C) 0.733 (solid, 20°C)	1300 (liquid, 140°C) 1480 (solid, 20 °C)
D-Mannitol $C_6H_8(OH)_6$	167	316	- -	- 1520 (solid, 20°C)
Galactitol $C_6H_8(OH)_6$	188	351	- -	- 1520 (solid, 20 °C)

Table 3.4 - Examples of glycols that have been investigated as PCM [7]

Material	Melting temperature [°C]	Melting enthalpy [kJ/kg]	Thermal conductivity [W/m·K]	Density [kg/m³]
Diethylene glycol $C_4H_{10}O_3$	-10 to -7	-	- -	1120 (liquid, 20°C) -

Triethylene glycol $C_6H_{14}O_4$	-7	-	-	1120 (liquid, 20°C)
			-	-
PEG400	8	100	0.19 (liquid, 38°C)	1125 (liquid, 25°C)
				1228 (solid, 3°C)
PEG600	17-22	127	0.19 (liquid, 38°C)	1126 (liquid, 25°C)
			-	1232 (solid, 4°C)
PEG1000	35-40	-	-	-
			-	-
PEG3000	52-56	-	-	-
			-	-
PEG6000	55-60, 66	190	-	1085 (liquid, 70°C)
			-	1212 (solid, 25°C)
PEG10000	55-60	-	-	-
			-	-

3.2.2 Inorganic PCM

Inorganic materials used as PCM are divided into salt hydrate and metallics and cover a wide temperature range (Fig. 3.2). Compared to organic PCM, inorganic materials usually have similar melting enthalpies per unit mass, but higher ones per unit volume due to their high density.

Salt Hydrates

Salt hydrates consist of a water and salt in a discrete mixing ratio. The solid–liquid transformation of salt hydrates is, in fact, a dehydration of hydration of the salt, although this process resembles melting or freezing thermodynamically. Salt hydrates have been widely studied for their use in thermal energy storage systems. There are three different kinds of melting behaviour: congruent melting (when the anhydrous salt is completely soluble in water of hydration), in-congruent melting (when the salt is not completely soluble in water) and semi-congruent melting (when the liquid and solid phase are in equilibrium during phase transition). The advantages of this materials are: high latent heat of fusion per unit volume, relatively high thermal conductivity (almost double of the paraffins), small volume changes during melting process, non corrosive, compatible with plastics, only slightly toxic and quite cheap. The main drawback is the in-congruent melting. As *n* moles of water of hydration are not sufficient to dissolve one mole of salt, the resulting solution is supersaturated at the melting temperature. The solid salt, due to its higher density, settles down at the bottom of the container and the recombination with water during the reverse process of freezing is not possible. This results in an irreversible melting–freezing of the salt hydrate that produce low cycling stability; furthermore salt hydrate are corrosive with metal containers and present subcooling. Table 3.5 shows examples of salt hydrates used as PCM.

Table 3.5 - Examples of salt hydrates that have been investigated as PCM [7]

Material	Melting temperature [°C]	Melting enthalpy [kJ/kg]	Thermal conductivity [W/m·K]	Density [kg/m³]
LiClO$_3$·3H$_2$O	8	155	-	1530 (liquid)
			-	1720 (solid)
KF·3H$_2$O	18.5	231	-	1447 (liquid, 20°C)
			-	1455 (solid, 18°C)
CaCl$_2$·6H$_2$O	29,30	171,190	0.540 (liquid, 39°C)	1562 (liquid, 32°C)
			1.088 (solid, 23 °C)	1710 (solid, 25°C)
LiNO$_3$·3H$_2$O	30	296	-	-
			-	-
Na$_2$SO$_4$·10H$_2$O	32	254	-	-
			0.554	1485 (solid)
Na$_2$HPO$_4$·12H$_2$O	35-44	280	0.476 (liquid)	1442 (liquid)
			0.514 (solid)	1522 (solid)
NaS$_2$O$_3$·5H$_2$O	48-55	187-209	-	1670 (liquid)
			-	1750 (solid)
Na(CH$_3$COO)·3H$_2$O	58	226,264	-	1280 (liquid)
			-	1450 (solid)
Ba(OH)$_2$·8H$_2$O	78	265,280	0.653 (liquid, 86°C)	1937 (liquid, 84°C)
			1.255 (solid, 23°C)	2180 (solid)
Mg(NO3)2·6H2O	89,90	149,163	0.49 (liquid, 95 °C)	1550 (liquid, 94 °C)
			0.669 (solid, 56°C)	1636 (solid, 25°C)
MgCl2·6H2O	117	165,169	0.57 (liquid, 120 °C)	1450 (liquid, 120 °C)
			0.704 (solid, 110 °C)	1569 (solid, 20 °C)

Salt

Above 150 °C, different salts can be used as PCM. The main advantages are very high melting enthalpy, good thermal conductivity, good chemical stability and very low vapor pressure. The main drawbacks are subcooling and corrosion of metals. The volume change from solid to liquid can be up to 10%. Table 3.6 reports a selection of typical examples.

Table 3.6 - Examples of salt that have been investigated as PCM [7]

Material	Melting temperature [°C]	Melting enthalpy [kJ/kg]	Thermal conductivity [W/m·K]	Density [kg/m³]
LiNO₃	254	360	0.58 (liquid)	1780 (liquid)
			1.37 (solid)	2140 (solid)
NaNo₃	307	172	0.51 (liquid)	1900 (liquid)
			0.59 (solid)	2260 (solid)
KNO₃	333	266	0.50 (liquid)	1890 (liquid)
			-	1900 (solid)
MgCl₂	714	452	-	2140
			-	-
NaCl	800	492	-	2160
			-	-
Na₂CO₃	854	276	-	2533
			-	-
KF	857	452	-	2370
			-	-
K₂CO₃	897	236	-	2290
			-	-

Metallics

Metallic PCM includes the low melting metals and metal eutectics. Usually these materials are used for high temperature applications but their use is extremely limited for PCM thermal energy storage systems due to the high weight. The main advantages are high heat of fusion per unit volume, high thermal conductivity and low vapor pressure, while the drawbacks are weight, low heat of fusion per unit mass and low specific heat. Table 3.7 shows examples of metallics materials used as PCM.

Table 3.7 - Examples of metallics that have been investigated as PCM [10]

Material	Tm [°C]	λ [kJ/kg]
Cu(83)-10P-7Si	840	92
Cu(74)-19Zn-7Si	765	125
Cu(91)-9P	715	134
96Zn-4Al	381	138
Mg(55)-28-17Zn	400	146

Zn(49)-45Cu-6Mg	703	176
Mg(52)-25Cu-23Ca	453	184
46.3Mg-53.7Zn	340	185
Cu(80)-20Si	803	197
Zn2Mg	588	230
Mg2Cu	847	243
Mg(60)-25Cu-15Zn	452	254
Mg(84)-16Ca	790	272
34.65Mg-65.35Al	497	285
Al(54)-22Cu-18Mg-6Zn	520	305
Si(49)-30Mg-21Ca	865	305
Al(59)-35Mg-6Zn	443	310
Mg(47)-38Si-15Zn	800	314
64.3-34.0Cu-1.7Sb	545	331
68.5Al-5.0Si-26.5Cu	525	364
60.8Al-33.2Cu-6.0Mg	506	365
Cu(69)-17Zn-14P	720	368
66.92Al-33.08Cu	548	372
64.1Al-5.2Si-28Cu-2.2Mg	507	374
46.3Al-4.6Si-49.1Cu	571	406
Cu(56)-27Si-17Mg	770	420
Al(54)-30Cu-5Si	571	422
86.4Al-9.4Si-4.2Sb	471	471
83.14Al-11.7Si-5.16Mg	555	485
87.76Al-12.24Si	557	498
Si(56)-44Mg	946	757

3.2.3 Eutectics

An eutectic is a mixture of two or more constituents, which solidify simultaneously out of the liquid at a minimum freezing point, also called eutectic point. At the eutectic point, the liquid reacts to a solid that is composed of two or more solid phases with different composition; however, the overall composition is still the same as in the liquid [16]. Therefore, eutectics nearly always freeze without segregation because they freeze to an intimate mixture of crystals, leaving

little opportunity for the components to separate. Table 3.8 shows examples of eutectics materials used as PCM.

Table 3.8 - Examples of metallics that have been investigated as PCM [3]

Material	Composition (wt. %)	Melting point (°C)	Latent heat (kJ/kg)
$CaCl_2 \cdot 6H_2O + CaBr_2 \cdot 6H_2O$	45+55	14.7	140
Triethylolethane+water+urea	38.5+31.5+30	13.4	160
$C_{14}H_{28}O_2 + C_{10}H_{20}O_2$	34+66	24	147.7
$CaCl_2 + MgCl_2 \cdot 6H_2O$	50+50	25	95
$CH_3CONH_2 + NH_2CONH_2$	50+50	27	163
Triethylolethane+urea	62.5+37.5	29.8	218
$Ca(NO_3) \cdot 4H_2O + Mg(NO_3)_3 \cdot 6H_2O$	47+53	30	136
$CH_3COONa \cdot 3H_2O + NH_2CONH_2$	40+60	30	200.5
$NH_2CONH_2 + NH_4NO_3$	53+47	46	95
$Mg(NO_3)_3 \cdot 6H_2O + NH_4NO_3$	61.5+38.45	52	125.5
$Mg(NO_3)_3 \cdot 6H_2O + MgCl_2 \cdot 6H_2O$	58.7+41.3	59	132.2
$Mg(NO_3)_3 \cdot 6H_2O + MgCl_2 \cdot 6H_2O$	50+50	59.1	144
$Mg(NO_3)_3 \cdot 6H_2O + Al(NO_3) \cdot 9H_2O$	53+47	61	148
$CH_3CONH_2 + C_{17}H_{35}COOH$	50+50	65	218
$Mg(NO_3)_3 \cdot 6H_2O + MgBr_2 \cdot 6H_2O$	59+41	66	168
Napthalene+benzoic acid	67.1+32.9	67	123.4
$NH_2CONH_2 + NH_4Br$	66.6+33.4	76	151
$LiNO_3 + NH_4NO_3 + NaNO_3$	25+65+10	80.5	113
$LiNO_3 + NH_4NO_3 + KNO_3$	26.4+58.7+14.9	81.5	116
$LiNO_3 + NH_4NO_3 + NH_4Cl$	27+68+5	81.6	108

3.3 Performance of TES systems with PCM

To improve the efficiency of the charging and discharging processes of a PCM-TES system, the most relevant parameter to be studied is thermal conductivity of the material. In fact, during the discharging process, the energy released by solidification of the PCM must be transported from the solid–liquid interface through the growing solid layer to the heat exchanger surface. Hence, the heat transfer coefficient is dominated by the thermal conductivity of the solid PCM. However, most PCM usually provide low thermal conductivity around 0.5 W/(m·K) [23] which results in poor heat transfer between the HTF and the storage material. In order to increase the thermal

conductivity of PCM, several heat transfer enhancement techniques have been studied (fig. 3.3-3.4): incorporating high thermal conductivity enhancers into PCM and porous heat transfer media, extending heat transfer surfaces by fins and capsules, using intermediate heat transfer medium or heat pipes and employing multiple PCMs.
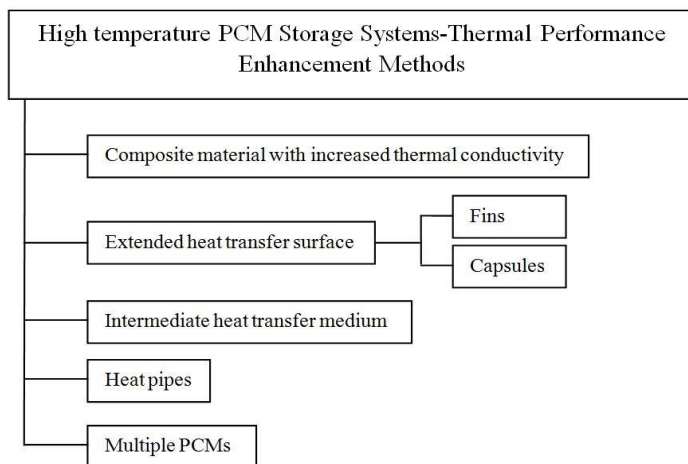
Fig. 3.3 - Classification of investigated performance enhancement techniques in TES-PCM [24]
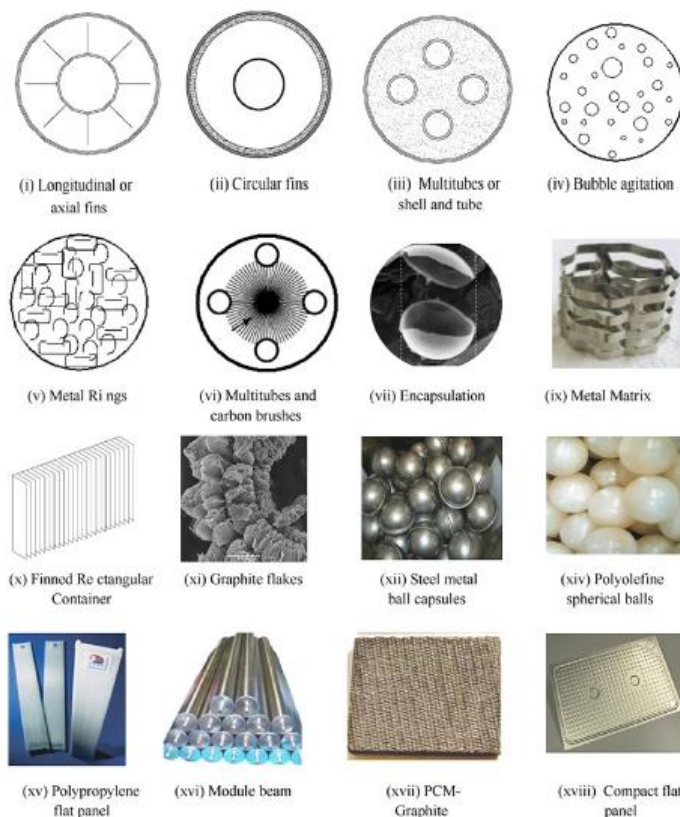
Fig. 3.4 - Examples of enhancement techniques in TES-PCM

3.3.1 High-thermal conductivity material enhancers

The heat transfer within a PCM storage system can be enhanced by composing high thermal conducting material into the PCM. Usually this technique include materials such as ceramic compound, metal foam and graphite.

Using ceramic compound, the molten PCM is retained and immobilized within the micro-porosity defined by the ceramic network by capillary forces and surface tension, which offers the potential of using direct contact heat exchange [25].

Recently, graphite has been studied extensively as heat transfer enhancer in PCM storage systems due to its high thermal conductivity, low density and chemical resistance [16] [26] [27]. The PCM graphite composite can be obtained by infiltration/impregnation of PCM within a porous structure of graphite, dispersion of graphite mechanically within the PCM or compression of the pre-mixed graphite and PCM [28]. There are numerous commercial available types of graphite, such as natural graphite flakes, expanded natural graphite and ground expanded natural graphite. Zhao and Wu [29] [30] experimentally investigated the feasibility of using metal foam and expanded graphite to enhance the heat transfer capability of $NaNO_3$. The results showed that the heat transfer rate increase in both charging and discharging phases using this method.

Another technique consist in the insertion of steel lattice or structures with cylindrical or spherical geometries into the PCM to obtain a melting/solidification time reduction. Drawbacks of this solution are higher volume and costs.

3.3.2 Extended heat transfer surface enhancers

Extensions of heat transfer surface includes the use of capsules or finned tubes to reduce the distance for heat transport within the PCM thus improving the heat transfer.

The encapsulation of PCM is divided into macro, micro and nano encapsulation. In macro-encapsulation, the size of container filled by PCM ranges from several mm up to several cm. These are often containers and bags made of metal or plastic. Micro-encapsulation is the encapsulation of solid or liquid particles of 1 μm to 1 mm diameter with a solid shell, while the capsules smaller than 1 μm are classified as nano-encapsulation. Physical processes used in micro-encapsulation are spray drying, centrifugal and fluidized bed processes, or coating processes for example in rolling cylinders. Chemical processes used are in-situ encapsulations like complex coacervation with gelatine, interfacial polycondensation to get a polyamide or polyurethane shell, precipitation due to polycondensation of amino resins, and others [16]. If the rigid capsule is used to contain the PCM, the initial PCM volume should not exceed 80% in order to compensate the pressure variation during the melting/solidification cycling. There are many advantages of microencapsulated PCM, such as increasing heat transfer area, reducing PCM reactivity towards the outside environment and controlling the changes in the storage material volume as phase change occurs, corrosive to metal, decomposition, sub-cooling and leakage [31].

Fins are used in a large number of applications to increase the heat transfer from surfaces. The fin is exposed to the PCM, which cools or heats it, with the high thermal conductivity allowing increased heat being conducted from the wall through the fin. Fins have several shapes but the

most commons are axials and circulars orthogonal to the axis of the heat transfer fluid pipes. Typically, the fin material has a high thermal conductivity as graphite foil, aluminium, steel and copper.

3.3.3 Intermediate heat transfer medium enhancers

The concept is based on the reflux created by a combined evaporation–condensation process occurring in the intermediate HTF. This technology is named Reflux Heat Transfer Storage (RHTS) system and, it is studied by Adinberg et al. [32] applied to DSG system. Fig. 3.5 reports the schematic of RHTS storage. HTF is used to transfer heat between the PCM and two heat exchangers placed externally of the PCM at the bottom and the top and of the storage vessel. The bottom heat exchanger is immersed in the liquid HTF and connected to the solar working fluid (water or oil) and it is used during charge phase. The top heat exchanger is a steam generator which produces superheated steam and it is used during discharge phase. In the charging process, the liquid HTF absorb energy through vaporization and the vapour flows upwards through the transport channels distributed in the PCM. Then the vapour condenses on the channel's surfaces and the latent heat of vapour is released across the walls to the PCM. The liquefied HTF returns to the pool due to gravity. In the discharging process, the PCM release the energy producing the evaporation of the liquid HTF. This vapour transfers energy to the HTF passing through the top heat exchanger [33].
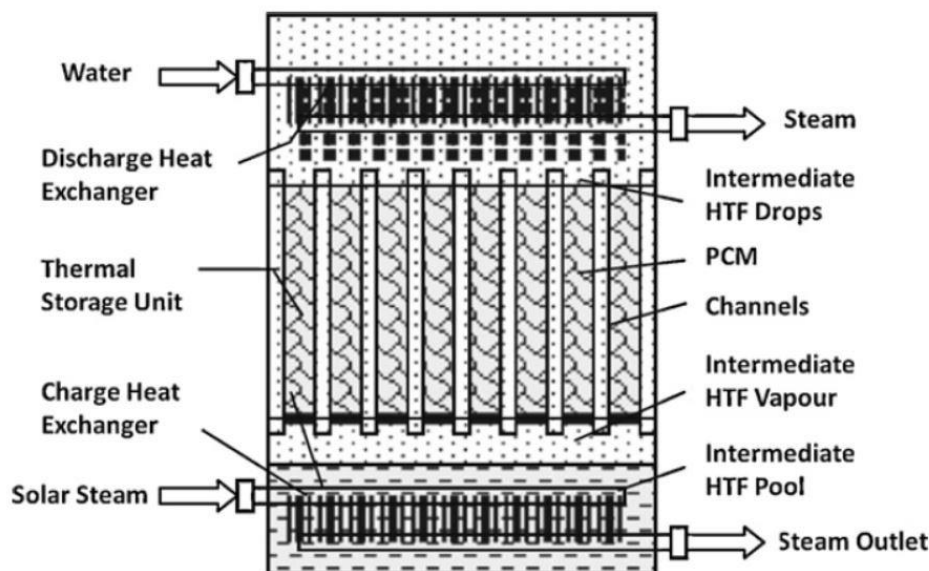
Fig. 3.5 - Reflux heat transfer storage concept

3.3.4 Heat pipe enhancers

The heat pipes are incorporated into the PCM-TES system in order to provide a channel with high thermal conductivity between the HTF and the PCM (fig. 3.6). The heat pipes transfer heat between the HTF and the PCM with evaporation and condensation of the heat pipe working fluid occurring at the ends of the heat pipes. Shabgard et al. [34] investigated the impact of the number of heat pipes, their orientation relative to the HTF flow direction and the gravity vector in two distinct system configurations.
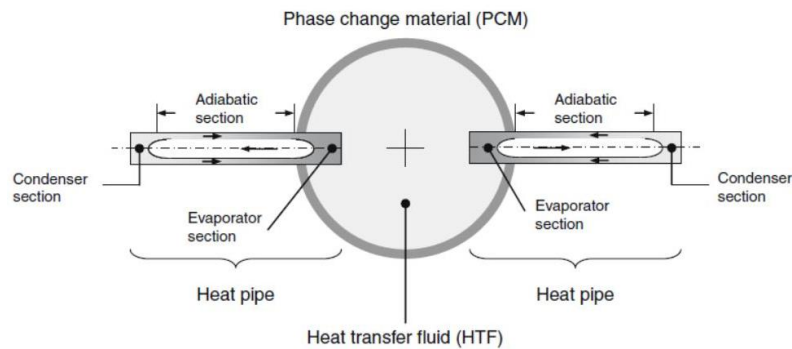
Fig. 3.6- Heat transfer between PCM and HTF using heat pipes [34]

3.3.5 Multiple PCM enhancers

In this system, also named cascaded or multi-stage, few modules containing different PCM with different melting temperatures are connected to each other in series [35] [36] [37]. The multi-stage configuration is obtained by placing the PCMs in a decreasing order of their transition temperatures according to flow direction during charge process, while in an increasing order of their transition temperatures according to flow direction during discharge process as illustrated in fig. 3.7. The heat transfer rate in the storage systems is mainly dependent on the temperature difference between the HTF and the PCM. When a single PCM configuration is used, this temperature difference decreases in the HTF flow direction, consequently also the heat transfer rate decreases. When a multiple PCM configuration is used, the temperature difference can be maintained approximately constant because both the HTF temperature and the melting point of the PCM decrease in the HTF flow direction during the charging process. During discharge both of them increase in the HTF flow direction. Therefore, the heat flux from the PCM to the HTF is nearly constant during the entire process.
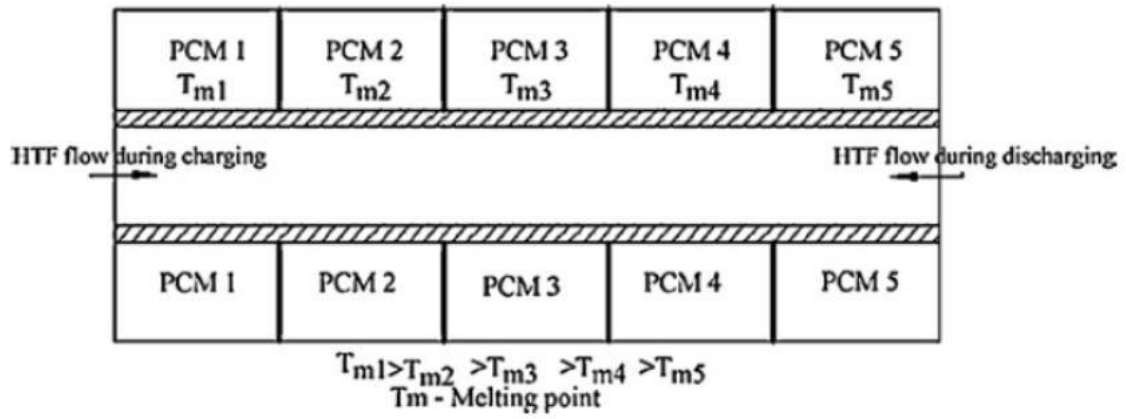
Fig. 3.7- Multiple PCM configuration in thermal energy storage systems

Chapter 4

Mathematical models of the PCM thermal energy storage system

4.1 Introduction

In this thesis, different n-dimensional numerical models were developed with the COMSOL Multiphysics 5.0 platform in order to simulate the transient and energy behaviour of different geometries and configuration of PCM-TES systems during the phase change processes. COMSOL Multiphysics is a software package for analysis, simulation and solver applied to various physical and engineering applications, especially coupled phenomena, or multiphysics based on finite elements method.

Two different approaches both in accordance with the apparent heat capacity formulation were evaluated and presented. In the first approach the energy equation was solved considering heat transfer only by conduction in liquid PCM domain. For this case, a 3D numerical simulation code was developed to simulate the thermal energy storage system based on the configuration of the shell and tube heat exchanger.

In the second approach the energy equation was solved considering heat transfer by heat conduction and natural convection in liquid PCM domain. The Boussinesq approximation was introduced to consider the buoyancy force. For this case, a 2D axysimmetric numerical code was developed comparing different configurations of TES (double tube, double tube with fins and triplex with fins). Furthermore the effect of the number of fins on the PCM melting time was investigated.

Finally, a 2D axysimmetric numerical model of a double tube heat exchanger with fins was validated considering the two different approaches. The purpose of this analysis was focused both on the performance evaluation of different TES configurations and on the evaluation of which mathematical model presents more accuracy to simulate the real behaviour of these systems.

4.2 Mathematical models

The phenomena of melting and solidification are associated with many practical applications, not only in thermal energy storage systems but also in several industrial processes, such as metal processing, solidification of castings and environmental engineering, in food and pharmaceutical processing. Predicting the behaviour of phase transition is difficult due to its non-linear nature at moving boundary and also because PCM materials show thermo-physical properties which vary

according to the phase. The term 'moving boundary problems' is associated with time-dependent problems, where the position of the moving boundary must be determined as a function of time and space. The analysis of heat transfer related to phase transition problems is called Stefan problem. The Stefan problem was first investigated as pure conduction and later natural convection was considered during melting and solidification of PCM [38]. Analytical and numerical methods are used to solve Stefan problem.

Analytical solutions of melting and solidification problems require many simplification and approximations, are generally one-dimensional, consider heat transfer only by conduction, apply simple boundary and initial conditions and constant thermo-physical properties. Moreover, analytical solutions can be rigorously valid for semi-infinite domains only. Therefore, these results are used to provide basic knowledge of the phenomena as well as the basis for validation of more complicated theoretical and numerical schemes.

Due to these simplifying assumptions, the use of numerical methods is required to obtain more accurate solutions of the problem for most applications of practical interest. Therefore, ad-hoc codes for specific applications or commercial software adapting to the PCM behaviour during transition phase must be used and developed.

The finite elements method (FEM) is the numerical method most commonly used, but also finite difference method (FDM), boundary element method (BEM), the Monte-Carlo and others are used. The success of finite element and boundary element methods lies in their ability to handle complex geometries, while the time consuming in terms of computing and programming is the main drawback. These methods can be divided into front-tracking methods and fixed-domain methods.

- *Front tracking methods:*
    - Fixed mesh, finite difference
    - Variable mesh, finite difference
    - Moving mesh, finite element
    - Moving boundary element
- *Fixed domain methods:*
    - Apparent heat capacity
    - Enthalpy based formulations
    - Apparent heat capacity with post-iteration correction
    - Fictitious heat flow
    - Freezing index
    - Discontinuous integration

In this thesis, the phase change processes were treated using fixed domain method based on apparent heat capacity. This method will be explained in paragraph 4.2.1.

4.2.1 Apparent heat capacity formulation

The apparent heat capacity formulation assumes that the latent heat is evaluated by increasing the heat capacity of the material in a transition temperature range. For instance, in a solid-liquid transition, if the latent heat is released uniformly in the phase change temperature range, the apparent heat capacity is given by:

$$C_{p,app} = \begin{cases} C_{p,sol} & T < T_{sol} & \text{solid phase} \\[3ex] \dfrac{\left[\int_{T_{sol}}^{T_{liq}} Cp(T)dT + L_f\right]}{(T_{liq} - T_{sol})} & T_{sol} < T < T_{liq} & \text{solid/liquid phase} \\[3ex] C_{p,liq} & T < T_{liq} & \text{liquid phase} \end{cases} \qquad (4.1)$$

Where $C_{p,sol}$ and $C_{p,liq}$ are specific heat of solid and liquid phase respectively, T_{liq} and T_{sol} are the temperature of solid and liquid phase respectively, $Cp(T)$ is the specific heat during transition in function of the temperature, while L_f is the latent heat of fusion. Figure 4.1 reports the apparent heat capacity in function of temperature.
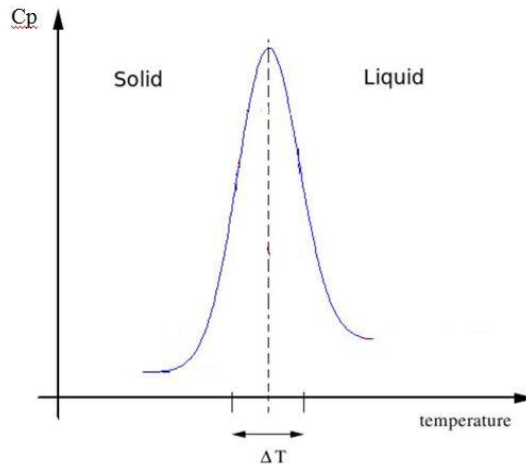
Fig. 4.1- Smoothed function used to evaluate C$_p$ in apparent heat capacity formulation

Using these definitions, the energy equation for the entire region is defined as:

$$\rho C_{p,app} \frac{\partial T}{\partial t} + \rho C_{p,app} u \cdot \nabla T = \nabla \cdot (k\nabla T) \qquad (4.2)$$

Where:

- ρ is the density [kg/m^3]
- u is the fluid velocity (PCM in liquid phase) [m/s]
- $C_{p,app}$ is the specific heat evaluated with Equation (4.1) [J/kg·K]
- k is the thermal conductivity [W/m·K]
- T is the temperature [K]
- t is the time [s]

The first term represents the rate of temperature change in function of time, the second and the third terms represent the heat transfer by conduction and by convection respectively.

Equation (4.2) can easily be discretized and solved numerically. The apparent heat capacity formulation was first applied using a finite difference method based on the Crank–Nicolson scheme for one-dimensional problems [39] where the phase change occurs in a finite temperature interval. Then it was applied using the finite element method in a generally applicable approach to one and two-dimensional problems with both moving boundary and temperature-dependent physical properties [40].

The apparent heat capacity formulation is conceptually simple and one of this advantages is that temperature is the primary dependent variable that derives directly from the solution. However, it is well known that this formulation presents an important drawback with respect to the other methods [41] when the phase change transition occurs at a fixed temperature. During melting process, if the temperature of a control volume rises from below the solidus to above the liquidus temperature in one time step, the absorption of the latent heat for that control volume is not accounted for. Same difficulty also occurs during solidification process. This problem can be overcome by assuming that the phase change occurs over a small temperature range and very small time steps have to be used during transition. All PCM considered in this thesis are not pure substances, whereby phase transition takes place not at a fixed temperature but in a range temperature. The use of the apparent heat capacity method is therefore justified.

4.3 First approach: 3D numerical model

4.3.1 Material and method

A 3D numerical simulation code of a PCM-TES during both charging and discharging processes was developed considering the first approach.

The geometry adopted for the storage system is presented in figure 4.2 and it is based on the configuration of the shell and tube heat exchanger. Shell is filled with PCM while the working fluid flows in the tube side. The choice of this configuration was made taking into account that a similar storage system will be used for the experimental investigations with the test rig implemented in the laboratory for TES technologies of the DIMCM-University of Cagliari. The design of the test rig and of the TES are treated in chapter 5.
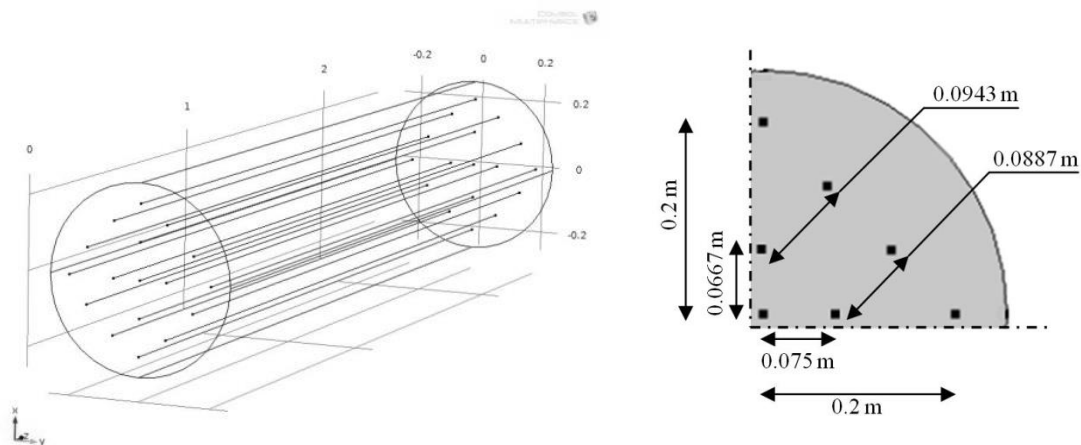
Fig. 4.2 - Geometrical configuration of TES system

For this model, Hydroquinone was selected among different PCM candidates after a literature review [9][16][23][42][43] since it has a phase change temperature range between 166 °C and 173 °C and a melting enthalpy of 225 kJ/kg [9]. Many applications exist in this temperature range such as in solar technologies generally associated with Organic Rankine Cycle (ORC) or in solar cooling systems with absorption chiller, related to fuel cell PAFC, heat recovery in metal hydrides hydrogen storage systems, in the food, beverage, transport equipment, textile, machinery, pulp and paper industries and drying of agricultural products as reported in Table 1.3.

Hydroquinone is an aromatic organic compound that is a type of phenol, a derivative of benzene, having the chemical formula $C_6H_4(OH)_2$. This material was chosen because its properties and features are easy to find in the literature and could be readily used for calculation. However, Hydroquinone presents an important drawback concerning the toxic hazards: its mutagenic and carcinogenic properties make it inappropriate in laboratory activities. Therefore, different materials, most suitable for laboratory activities, were also selected for the other analysis presented in this thesis. The properties of Hydroquinone are shown in Table 4.1 [44].

Table 4.1 - Properties of Hydroquinone

	Solid	*Liquid*
Density (kg/m³)	1358	1155
Specific heat (J/kg·K)	2310	2670
Thermal conductivity (W/m·K)	0.45	0.612
Phase change temperature	172.4 °C	
Range phase transition temperature	3 °C	
Latent heat	225 kJ/kg	
Boling point	285 °C	
Flash point	165 °C - closed cup	
pH	3.7 at 70 g/l	

The "Therminol66" from Solutia Inc. was selected as heat transfer fluid (HTF) as it covers an operating range suitable with the process under study.

The design of the storage system was based on the Logarithmic Mean Temperature Difference (LMTD) method and calculations were made using Matlab. The geometrical characteristics and the operating parameters of the TES are shown in Table 4.2.

Table 4.2 - Geometrical characteristics and operating parameters of storage system

	Units	*Value*
Diameter	m	0.127
Length	m	2.44
Number of tubes	-	17
Number pass of tubes	-	1
Internal diameter of tubes	m	0.0135
External diameter of tubes	m	0.0191
HTF mass rate	kg/s	0.11
PCM mass	kg	104
HTF temperature inlet charge	°C	200
HTF temperature inlet discharge	°C	100

The mesh used (Fig. 4.3) is built with 71731 free tetrahedral elements with size between $4.88 \cdot 10^{-4}$ m and $4.88 \cdot 10^{-2}$ m. The smallest elements of the mesh are used in the HTF inlet and outlet section in the system and to create a boundary layer around the tube and in the edges of the PCM. Axially in the outer surfaces of the PCM, where extreme precision is not required in the calculation of the temperature gradients, the largest elements of the mesh are used.
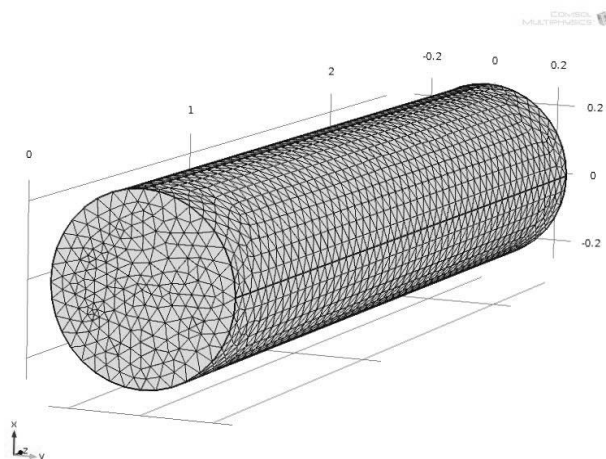
Fig. 4.3 - Mesh using for the TES simulation

The numerical model based on the first approach was developed to simulate the transient behaviour of the PCM-TES and to evaluate the TES overall performances. Two different "physics", described in the following, were used to create the model. The first physics "Non-Isothermal Pipe Flow" was used to simulate the pipes, the second "Heat Transfer with Phase Change" was used to simulate the PCM behaviour.

The following assumptions are applied:

- The velocity profile is fully developed and does not change within a section.
- Laminar flow
- Uniform temperature at inlet
- The cross section area is allowed to change between pipe segments.
- Empirical functions describe viscous losses.
- PCM is bounded by adiabatic external wall

- *Non-Isothermal Pipe Flow*

This module defines the conservation of mass, momentum and energy of a fluid inside the pipes (Eq. 4.3-4.5). The mass flow, pressure, temperature and concentration fields across the pipe sections are modelled as cross-section averaged quantities, which only vary along the length of the pipes. The pressure losses along the length of the pipes are described using Darcy friction factor expression. The energy balance equations are solved assuming heat transfer by convection and conduction, and the flow is considered incompressible.

$$\frac{\delta A \rho}{\delta t} + \nabla_t \cdot (A \rho u e_t) = 0 \tag{4.3}$$

$$\rho \frac{\delta u}{\delta t} = -\nabla_t p \cdot e_t - \frac{1}{2} f_D \frac{\rho}{d_h} |u| u \tag{4.4}$$

$$\rho A C_p \frac{\delta T}{\delta t} + \rho A C_p u e_t \cdot \nabla_t T = \nabla_t \cdot (A k \nabla_t T) + \frac{1}{2} f_D \frac{\rho A}{d_h} |u| u^2 + Q_w \tag{4.5}$$

where:

- A is the pipe cross section area available for flow [m^2]
- ρ is the density [kg/m^3]
- t is the time [s]
- u is the cross section averaged velocity [m/s]
- $e_t = (e_{t,x} e_{t,y} e_{t,z})$ is the unit tangent vector to the pipe axis
- p is the pressure [Pa]
- $f_D = f_D(Re, \varepsilon/d_h)$ is the Darcy friction factor. This parameter accounts for the continuous pressure drop along a pipe segment due to viscous shear, and is expressed as a function of the Reynolds number and the surface roughness divided by the hydraulic diameter. Thus, the second term on the right-hand side in Equation 4 represents the pressure drop due to viscous shear

- $Re = \rho u d_h / \mu$ is the Reynolds number
- μ is the dynamic viscosity [Pa·s]
- $d_h = 4A/Z$ is the mean hydraulic diameter [m]
- A is the pipe cross section area available for flow [m^2]
- Z is the wetted perimeter [m]
- T is the temperature [K]
- Q_w is the external heat exchange through the pipe wall [W/m] given by:

$$Q_w = (hZ)_{eff}(T_{ext} - T) \tag{4.6}$$

In Equation 4.6, $(hZ)_{eff}$ is an effective value of the heat transfer coefficient h [W/m^2·K] multiplied by the wall perimeter Z of the pipe. T_{ext} [K] is the external temperature outside of the pipe.

- *Heat Transfer with Phase Change*

The energy equation (4.2), in accordance with the apparent heat capacity formulation is used to obtain the temperature field in PCM domain. Instead of adding a latent heat L_f in the Equation (4.2) when the material reaches its phase change temperature T_m, it is assumed that the transition occurs in a temperature interval between $(T_m - \Delta T_m/2)$ and $(T_m + \Delta T_m/2)$. In this range the material phase is modelled by a smoothed function α, representing the fraction of phase that generates during transition. The value of this function is equal to 0 before $(T_m - \Delta T_m/2)$ and to 1 after $(T_m + \Delta T_m/2)$. The enthalpy H is expressed by:

$$H = (1 - \alpha)H_{phase1} + \alpha H_{phase2} \tag{4.7}$$

where H_{phase1} and H_{phase2} are the enthalpies of the material related to phase 1 or phase 2, respectively. Differentiating with respect to temperature, the following formula for the specific heat capacity is obtained:

$$C_p = (1 - \alpha)\frac{d}{dT}\left(H_{phase1}\right) + \alpha\frac{d}{dT}\left(H_{phase2}\right) + \left(H_{phase2} - H_{phase1}\right)\frac{d\alpha}{dT} \tag{4.8}$$

which can be rewritten as:

$$C_p = (1 - \alpha)C_{p,phase1} + \alpha C_{p,phase2} + \left(H_{phase2} - H_{phase1}\right)\frac{d\alpha}{dT} \tag{4.9}$$

In Equation (4.9) the third term of the second member is the distribution of latent heat:

$$C_L(T) = \left(H_{phase2} - H_{phase1}\right)\frac{d\alpha}{dT} \tag{4.10}$$

In the ideal case, when the PCM is a pure substance, α is the Heaviside function (equal to 0 before T_m and to 1 after T_m), the term $d\alpha/dT$ corresponds to the Dirac pulse. Therefore, C_L is the enthalpy jump L_f at temperature T_m that is added to specific heat capacity. The Equation (4.10) is approximated by:

$$C_L(T) = L_f \frac{d\alpha}{dT} \tag{4.11}$$

so that the total heat per unit mass released during the phase transition corresponds to the latent heat:

$$\int_{T_m-\Delta T/2}^{T_m+\Delta T/2} C_L(T)dT = L_f \int_{T_m-\Delta T/2}^{T_m+\Delta T/2} \frac{d\alpha}{dT}dT = L_f \tag{4.12}$$

Finally, the apparent heat capacity $C_{p,app}$ is given by:

$$C_{p,app} = (1 - \alpha)C_{p,phase1} + \alpha C_{p,phase2} + L_f \frac{\partial \alpha}{\partial T} \tag{4.13}$$

The equivalent heat conductivity and density are given by Equations (4.14) and (4.15) respectively:

$$k = (1 - \alpha)k_{phase1} + \alpha k_{phase2} \tag{4.14}$$

$$\rho = \frac{(1 - \alpha)\rho_{phase1}C_{p,phase1} + \alpha\rho_{phase2}C_{p,phase2}}{(1 - \alpha)C_{p,phase1} + \alpha C_{p,phase2}} \tag{4.15}$$

These equations allow to evaluate the HTF behaviour, the heat transfer that occur in the entire model (in PCM domain only the heat transfer by conduction is considered) and the PCM thermophysical properties in both liquid and solid phase.

4.3.2 Results and discussion

In this paragraph the results of simulations performed on 3D model using the first approach are presented. Figures 4.4(a,b) show the temperature profiles during charge and discharge phase. The initial condition chosen assumes the temperature of the entire system (PCM, tubes, and HTF) equal to 100 °C. This condition was assumed to simulate a charging process starting from a homogeneous initial state of the PCM. In this way it is possible to clearly observe the phase transition of the PCM in the sections closest to the HTF inlet. Then, after 1 min, the HTF temperature is assumed to increase up to a value of 200 °C with a step function thus, the charging process starts (Fig. 4.4a). The discharging process is performed analogously. At the beginning, the entire system temperature is equal to 200 °C, then, after 1 min, the HTF temperature suddenly decreases up to 100 °C and the discharging process begins (Fig. 4.4b).

(a)   (b)
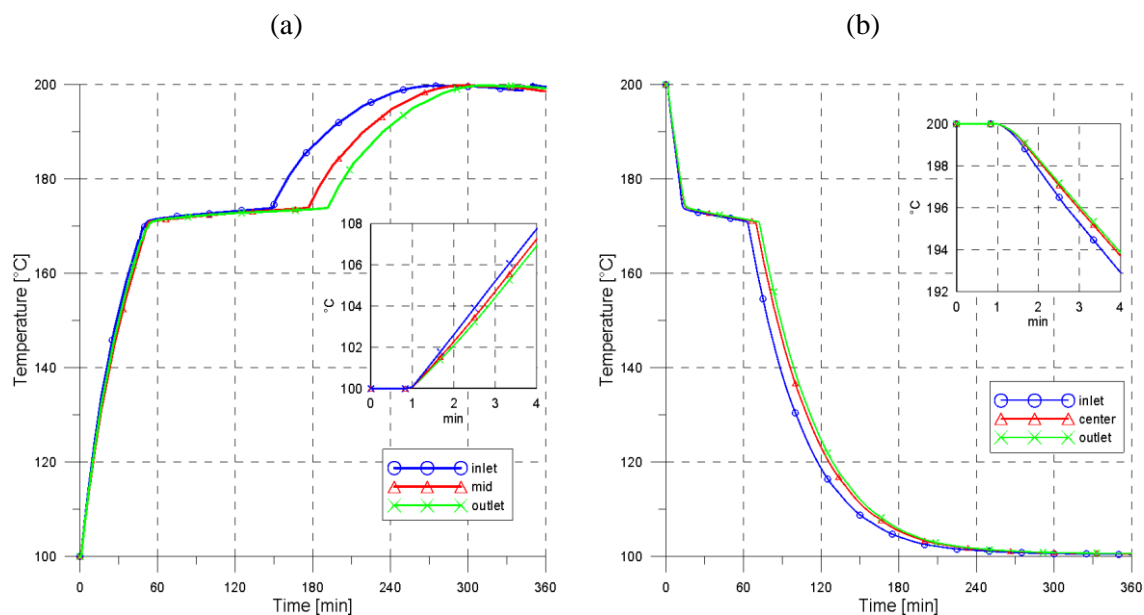
Fig. 4.4 - Profiles of PCM temperature for (a) charge phase, and (b) discharge phase

In the charge phase the transition process finishes after approximately 3 hours while in the discharge phase the complete transition is reached in about 1 hour. As expected, the melting process took more time than the solidification due to the lower difference between the phase change temperature of the PCM and the HTF temperature, being approximately 25°C and 70°C (absolute values), respectively.

Figures 4.5 and 4.6 show the phase change evolution for three different time steps during charge and discharge respectively. Three different sections of the TES are represented: the inlet, the mid

and the outlet section starting from the left. The red area represents the solid phase of the PCM material, the blue area represents the liquid phase while the tubes are reported as black lines. The first time step is selected to show the existing condition in the three section considered when in the outlet section begins the transition process. Instead, the third time step is selected to show the condition in which the PCM has completely terminated the transition phase in the inlet section. The second time step represents approximately an intermediate time between the beginning and the end of the phase transition

60 min

100 min

150 min
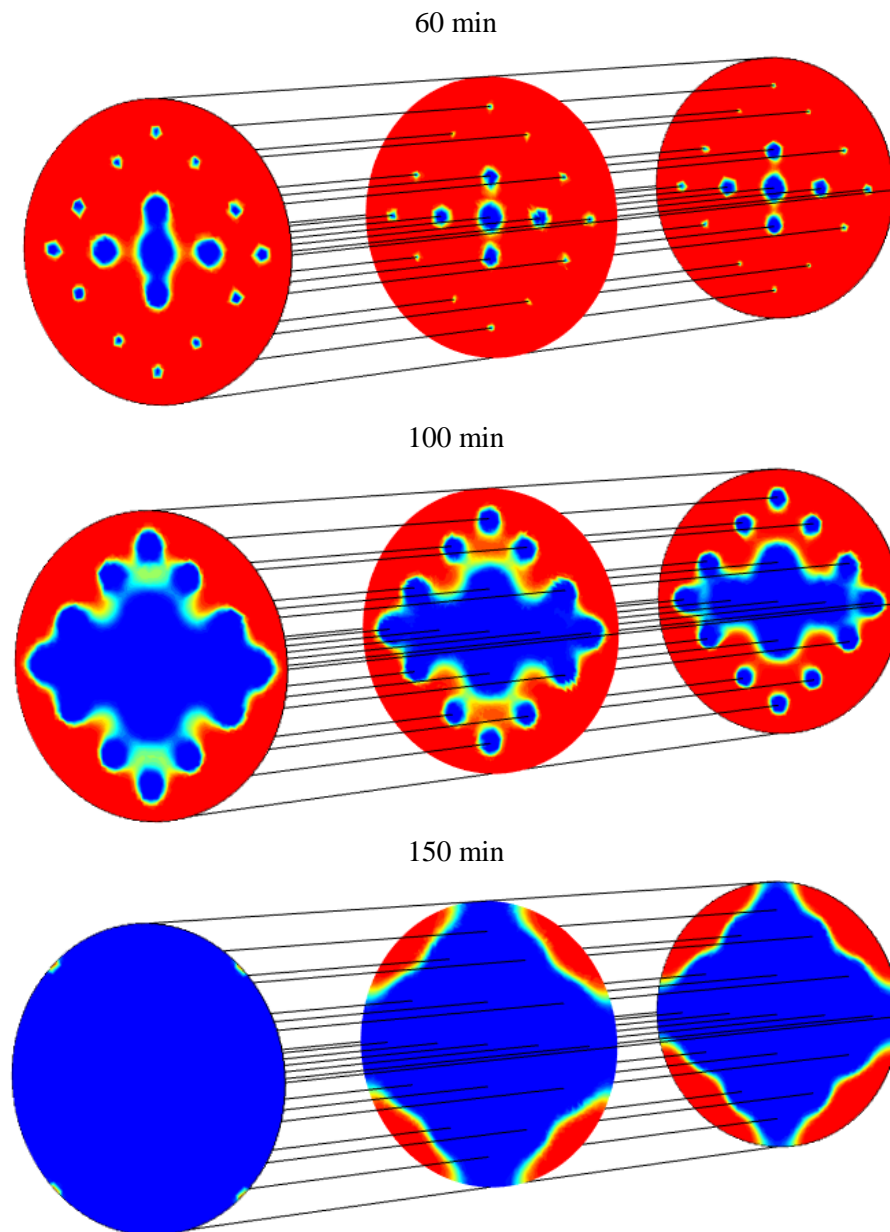
Fig. 4.5 - Profiles of PCM temperature and solid-liquid interface evolution in the charge phase

As expected the PCM phase change starts in proximity of the tubes, then continues in the intersections between them, and finally near the wall of the shell. It can be notice that the in the central part of the TES, the melting process proceeds more quickly than in the external part owing to the different tube pitch chosen for this configuration as reported in Figure 4.5. It is evident that

lower the tube pitch, greater the thermal interaction between the tubes that allows a greater heat transfer rate released to the PCM. When the phase transition begins to be detected in the inlet section, it takes approximately 4 minutes for melting to propagated up to the outlet section. After 100 minutes, melted PCM is in the area enclosed by the tube in the inlet section, while in the outlet section the solid-liquid front has not yet reached the outer tubes. After 150 minutes the PCM in the inlet section is completely in liquid state, while in the mid and in the outlet section, areas with PCM in solid state already exist near the external wall. When in the inlet section the complete melting is achieved, it needs another 40 minutes to reach the complete transition in the outlet section.

15 min

40 min

75 min
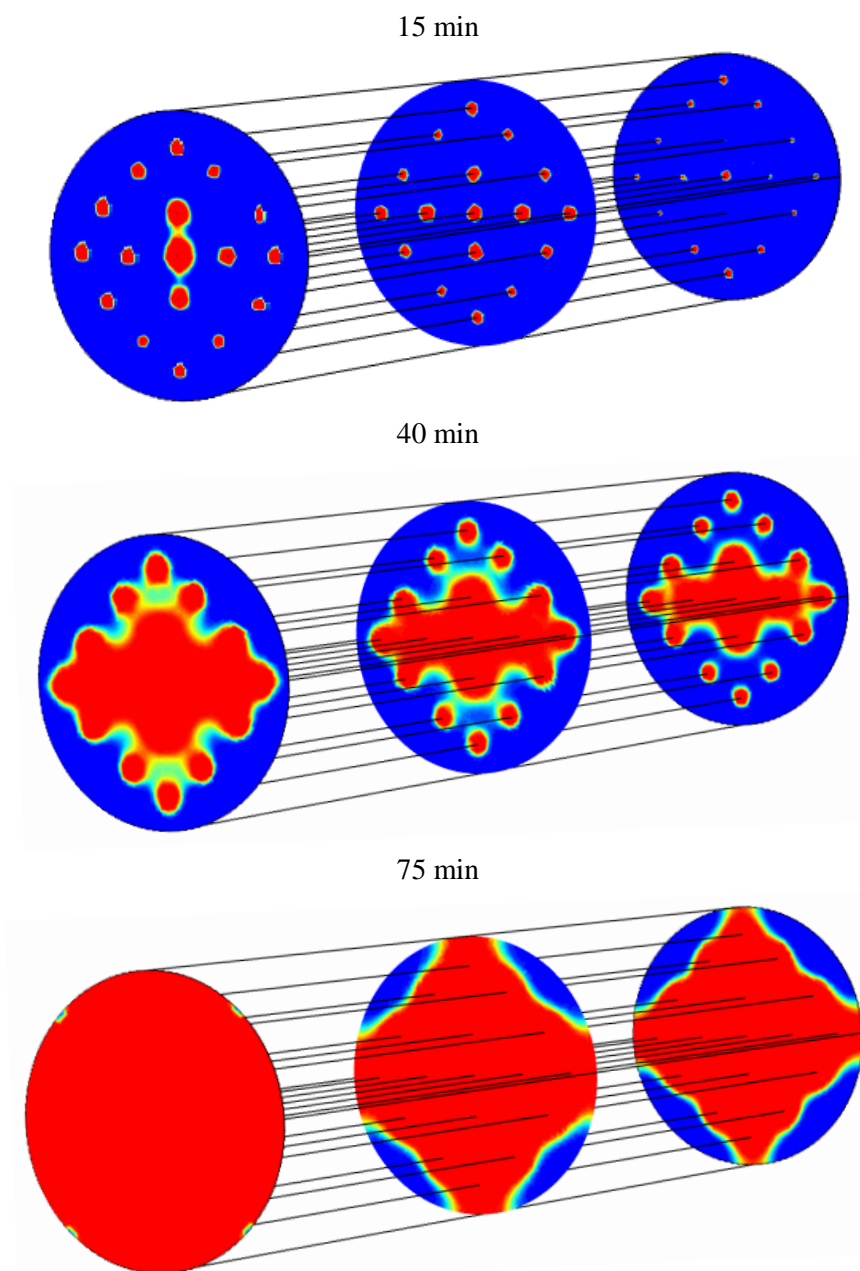
Fig. 4.6 - Profiles of PCM temperature and solid-liquid interface evolution in the discharge phase

Figure 4.6 shows, in a similar way of figure 4.5, the phenomena of solidification during the discharge phase. Also in this case, the pitch tube influences the transition process. After 15 minutes a PMC in solid state is observed in the inlet section, while in the outlet section only very small areas around the tubes are observed. After 40 minutes the solid-liquid interface moves from the center to the external wall of the TES. After 75 minutes, in the inlet section the PCM is completely solidified, while the mid and the outlet section still presents areas of liquid PCM in proximity of the external wall.

The shape of solid-liquid interface depends on the heat transfer process considered. The solid-liquid interface moves uniformly around the tubes because the convection and the buoyancy force were not considered with this approach. Another parameter that depends on heat transfer process is the melting and solidification time. In fact, convection improves the heat transfer between liquid and solid PCM decreasing the charge and the discharge phase time.

Further considerations about the shape and the motion solid-liquid interface and the effects of the natural convection will be presented in the following paragraphs. The comparison between the heat transfer only by conduction and the heat transfer by both conduction and convection is discussed by validating the two approaches discussed.

4.4 Second approach: 2D axysimmetric numerical model

4.4.1 Introduction

Several researches investigate the role of natural convection that occurs in the phase transition of a PCM during thermal energy storage. The literature includes studies on both numerical methods and different storage system configurations. The first are based on reproducing the time evolution of the solid-liquid interface during a melting and solidification process taking into account the natural convection phenomena. The latter are based on the development of different TES configuration to optimize the amount of exchanged heat. Longeon et al. [45] conducted an experimental and numerical study about the annular PCM solidification and melting system. The results show that in vertical TES the motion direction of the HTF into the TES, related to the natural convection heat transfer mechanism, affects the development of the PCM melting front. Furthermore, the configuration in which the HTF enters from above during the charging process and from the bottom during discharging process is recommended. Ismail and Da Silva [46] proposed a model for melting PCM around a horizontal circular cylinder, including heat transfer by convection. Agyenim et al. [47] and Dubovsky et al. [48] studied configuration of finned shell and tube heat exchanger storage systems. Castell et al.[49] determined the heat transfer coefficient by natural convection for a cylindrical module with external fins using experimental correlations. Khalifa et al. [50] conducted experimental and numerical investigations on the thermal performance of LHTES systems based on heat pipes for solar thermal power generation proving the benefits of added fins. Zhang and Faghri [51] analyzed numerically the heat transfer enhancement in LHTES systems using internal finned tube. The results indicate that the melting fraction can be significantly increased by increasing the thickness, height and number of fins.

4.4.2 Material and method

Three cases with different geometrical configurations (Fig. 4.7a,b,c) were considered in characterizing the TES system using the second approach:

- Case 1 (Fig. 4.7a) is based on the configuration of the double-tube heat exchanger, where the outer tube is filled with PCM while the heat transfer fluid (HTF) flows in the inner tube.

- Case 2 (Fig. 4.7b) is based on a triplex heat exchanger. It is composed of three tubes: the HTF flows in the outer and inner tubes, while the PCM is placed between them.

- Case 3 (Fig. 4.7c) is a triplex with circular fins with pitch ratio equal to 0.142 (Fin pitch ratio refers to the spacing between centerlines of fins divided by the TES length).

For the present study, D-Mannitol was selected from among different PCM candidates after a literature review [2][3][16][42][43][52] since it has a phase change temperature range between 164 and 170 °C. As for the Hydroquinone, in fact, also this material was selected in a operating temperature range between 150-200 °C where many applications exist such as in solar technologies generally associated with Organic Rankine Cycle (ORC) or in solar cooling systems with absorption chiller, related to fuel cell PAFC, heat recovery in metal hydrides hydrogen storage systems, in the food, beverage, transport equipment, textile, machinery, pulp and paper industries and drying of agricultural products as reported in Table 1.3.

D-Mannitol is classified as a sugar alcohol, molecular formula $C_6H_{14}O_6$: it is derived from a sugar (mannose) by reduction. The properties of D-Mannitol are shown in Table 4.4. Thermophysical properties of the liquid phase were obtained from other materials belonging to the same family and with similar transition temperatures with an estimated uncertainty of about 10%. Although widely used in other fields (pharmaceuticals, food industry etc.), only in recent years has this kind of materials been studied and used for thermal energy storage.

Due to its safety and its good thermophysical properties for thermal energy storage, D-mannitol was also selected as PCM for the experimental tests that will be performed in the DIMCM laboratories. As concerns latent heat, a value of 316 kJ/kg was found in literature [16], obtained for the pure substance and under controlled conditions, but several tests with the DSC [53][54][55][56][20] detected that this value depends strongly on three important factors, namely purity, cooling/heating rate and air contact. For these reasons, a more "realistic" value of 234 kJ/kg [c] was used in this work [16][54][55][56][57].

Table 4.3 - Properties of D-Mannitol.

	Solid	Liquid
Density (kg/m³)	1520 (20 °C)	1382
Specific heat (kJ/kg·K)	1.320 (20 °C) [a]	1.452
Thermal conductivity (W/m·K)	0.279 [b]	0.307
Phase change temperature	167°C	
Range of phase transition temperature	±3°C	
Latent heat	234 kJ/kg [c]	

[a] NIST web page (National Institute of Standards and Technology).
[b] Thermal Energy Storage Systems for Solar Cookers, www.ukessays.com
[c] value obtained as the average of the experimental results found in literature [16][54][55][56][57].

Syltherm800 from Dow Chemical Company was selected as the heat transfer fluid, as it is the HTF used in the experimental facility implemented in the laboratory for TES technologies of the DIMCM-University of Cagliari.

Syltherm800 is a highly stable, long-lasting, silicone fluid designed for high-temperature liquid phase operation. It has a recommended operating temperature range between -40°C and 400°C. The main advantages of this oil are low fouling potential, low freeze point, high-temperature stability, long life, non-corrosive, low acute oral toxicity and low odour. At elevated temperatures, it is sensitive to contamination. Contamination by acids or bases can result in accelerated rates of volatile by-product formation, while contamination by water, oxygen, or other oxidants can result in crosslinking of polymer molecules, that can cause a gradual increase in viscosity. Thus, it is important that contamination be minimized [58].
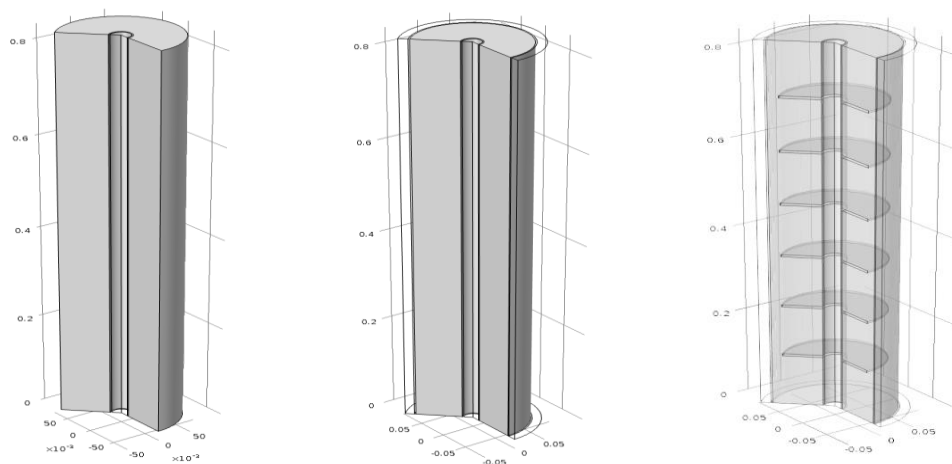
(a) Case 1 - Double tube   (b) Case 2 - Triplex   (c) Case 3 - Triplex with fins

Fig. 4.8 - Geometrical configuration of the three TES systems.

The design of the storage systems is based on the LMTD method and was performed by means of a computer code developed in Matlab environment. The geometrical characteristics of the three TESs are shown in Table 4.3. The value of HTF mass flow rate was selected as 0.052 kg/s for all three cases analyzed for both charge and discharge phases. In the triplex heat exchanger the flow rate is equally divided between inner and outer tube. Consequently, due to the different surface areas, the velocities results different and equal to 0.0664 m/s and 0.0049 m/s for inner and outer tube respectively. The HTF temperature at the inlet of the storage device was chosen equal to 180 °C and 100 °C for charge and discharge respectively. The HTF flows from top to bottom during both charge and discharge phases. The PCM mass for Cases 1 and 2 was 23.4 kg, while for Case 3, owing to the space occupied by the fins, the value was slightly lower, 22.8 kg, allowing a thermal energy storage of about 3 kWh.

Table 4.4 - Geometrical characteristics of the storage system

	Case 1	Case 2	Case 3
Heat transfer surface [m²]	0.077	0.568	0.73
Internal Diameter inner tube [m]	0.0254 (1")	0.0254 (1")	0.0254 (1")
Outside Diameter tube PCM [m]	0.127 (5")	0.127 (5")	0.127 (5")
Outside Diameter outer tube HTF [m]	-	0.1898	0.1898
Length [m]	0.83	0.83	0.83
Number of fins	-	-	6
Fin Length [m]	-	-	0.05
Fin thickness [m]	-	-	0.005
Tube thickness (Steel) [m]	0.002	0.002	0.002

A 2D axisymmetric numerical model using the second approach was developed with the COMSOL Multiphysics platform to simulate the transient and energy behaviour of the entire PCM-TES system during the phase change processes. Three different "physics", described below, were used to create the model:

-   the first and the third physics, "Fluid Flow", were used to simulate the behaviour of the HTF and the liquid PCM;

-   the second, "Heat Transfer", was used to simulate the heat transfer process between the HTF and the PCM; it is composed of three sub-modules: heat transfer by convection, by conduction and phase change heat transfer.

The mathematical model is based on the following hypothesis:

-   Two-dimensional and axisymmetric problem.
-   The velocity profile is fully developed and does not change within a section.
-   Laminar flow
-   Uniform temperature at inlet
-   The cross section area is allowed to change between pipe segments.
-   Empirical functions describe viscous losses.
-   PCM is bounded by adiabatic external wall

   – *Fluid Flow (HTF)*

To simulate the dynamic behaviour of the HTF flowing inside the inner tube (Case 1) and inside the inner and the outer tubes (Case 2-3), the continuity equation (4.15) and the momentum equation (4.16) were used. The flow is considered laminar and incompressible and the effect of gravity is negligible ($F=0$).

$$\frac{\partial \rho}{\partial t} + \nabla \cdot (\rho u) = 0 \qquad (4.15)$$

$$\frac{\partial \rho u}{\partial t} + \rho(u \cdot \nabla)u - \nabla \cdot \left[\mu\left(\nabla u + (\nabla u)^T\right)\right] + \nabla p = F \qquad (4.16)$$

where:

- ρ is the density[kg/m^3]
- μ is the dynamic viscosity [Pa·s]
- u is the velocity vector [m/s]
- p is the pressure [Pa]
- F is the volume force [N/m^3]
- T is the absolute temperature [K]
- t is the time [s]

In Equation (4.16) the first two terms correspond to the inertial forces, the third term corresponds to viscous forces, the forth represents the pressure forces and the first term at second member corresponds to the external forces applied to the fluid.

- *Heat Transfer in Fluid*

Heat transfer from the HTF to the wall of the steel tube takes place by convection. The energy equation (4.17) was solved using the velocities found from the solution of Eqs. (4.15) and (4.16). In Equation (4.17) C_p and k are respectively the specific heat and the thermal conductivity of the material.

$$\rho C_p \frac{\partial T}{\partial t} + \rho C_p u \cdot \nabla T = \nabla \cdot (k \nabla T) \tag{17}$$

- *Heat Transfer in Solid*

Heat transfer from the wall of the steel tube to the PCM takes place by conduction. The energy equation (4.17) for this case is reported below:

$$\rho C_p \frac{\partial T}{\partial t} = \nabla \cdot (k \nabla T) \tag{4.18}$$

- *Heat Transfer with Phase Change*

Also for this case, the energy equation (4.2), in accordance with the apparent heat capacity formulation (Eq. 4.12), was used to obtain the temperature field and the PCM properties (Eqs 4.13-4.14).

- *Fluid Flow (liquid PCM)*

The continuity (4.15) and momentum (4.16) equations were used to simulate the behaviour of the PCM in liquid phase. To simulate the buoyancy force giving rise to natural convection, a volume force was added. The Boussinesq approximation was introduced to consider this buoyancy force, according to Equation (4.19). In this case ρ, μ and β are respectively the density, the dynamic

viscosity and the thermal expansion coefficient of the liquid PCM [1/K], g is the gravitational constant [m/s^2] and T_m is the melting temperature. The flow is considered laminar and incompressible.

$$F_b = g\rho\beta(T - T_m) \tag{4.19}$$

In this approach, the entire PCM was treated as a liquid, even when its temperature was lower than its melting point. A modified viscosity was used to force this liquid to behave as a solid when required. A step function, continuous second derivative centred at about T_m, was introduced to define the modified viscosity: an extremely large value was selected for the solid PCM and the actual value of μ was selected for the liquid PCM [59]. This approach forces the Navier-Stokes equation to calculate the velocity everywhere, even when the PCM is a solid. This significantly increases the number of calculations and the possibility that the solver will diverge during the simulation. A second volume force, defined by Eq. (4.20), was added to the momentum equation to calculate velocities equal to zero in the solid phase of PCM.

$$F_v = -A(T) \cdot \mathrm{u} \tag{4.20}$$

In this equation a step function $A(T)$ was introduced: its value was extremely large for the solid PCM and zero for the liquid PCM [59]. The role of F_v is to dominate every other force terms in the momentum equation (4.16) when the PCM is solid, thus improving the time of calculation and effectively forcing a trivial solution of $u = 0$ in the solid. This method is mathematically better defined and allows a reduction of the number of iterations performed by the solver.

4.4.3 Results and discussion

In this paragraph the simulation results of the three cases considered are presented. Figure 4.6 shows the temperature evolution of the PCM evaluated at the bottom of the accumulator (in proximity of the HTF outlet), in function of time during charge (Fig. 4.6a) and discharge (Fig. 4.6b). In charging mode, the process started from a homogeneous initial state of the entire system (PCM, tubes, and HTF). At the beginning, the entire PCM system was at the set temperature of 100 °C, with an inlet temperature of the HTF of 180 °C. In this condition the heat transfer inside the solid PCM was governed by conduction. Then, when the temperature range of phase transition was reached, the melting process began. During the phase transition both conduction and natural convection in liquid phase occurred. At the end of the transition process, the heat transfer inside the liquid PCM was governed by convection.
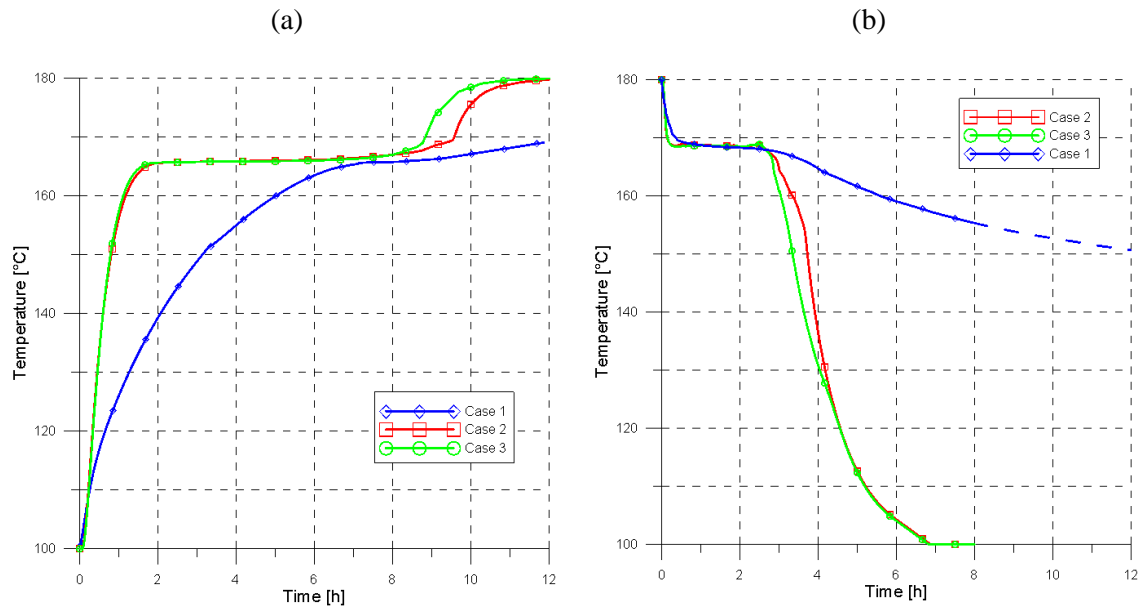
Fig. 4.8 - PCM temperature profile for charge (a) and discharge (b) processes.

The discharging process was performed analogously. Initially, the entire PCM system was at the set temperature of 180 °C, with an inlet temperature of the HTF of 100 °C. The duration of the charge and discharge processes was imposed as 12 and 8 hours respectively. In the charge phase the transition process finished after approximately 9-10 hours, while in the discharge phase the complete transition was reached in about 3.5 hours. As expected, the melting process took longer than solidification owing to the lower temperature difference between PCM during transition and HTF at the accumulator inlet, approximately 15 °C during charge and 70 °C during discharge. Case 3 presents the lowest time of charge and discharge, owing to the enhanced heat transfer surface which allows the exchange of higher and more uniform thermal power with respect to the other cases. Fig. 4.8 points out that neither in the charging nor in the discharging phase does Case 1 reach the equilibrium condition for melting/solidification respectively. In fact, after 12 hours of charge and 8 hours of discharge, the PCM shows a lower temperature value than the HTF temperature at TES inlet equal to 180 °C and 100 °C for charge and discharge respectively. Therefore, in this case the charge and the discharge processes are much slower than in the other two cases. The dashed line refers to the condition where Case 1 continues for 12 hours as for the charge phase.

	80 min	200 min	460 min	20 min	120 min	215 min

Case 1

(a)   (b)

Case 2

(c)   (d)

Case 3

(e)   (f)
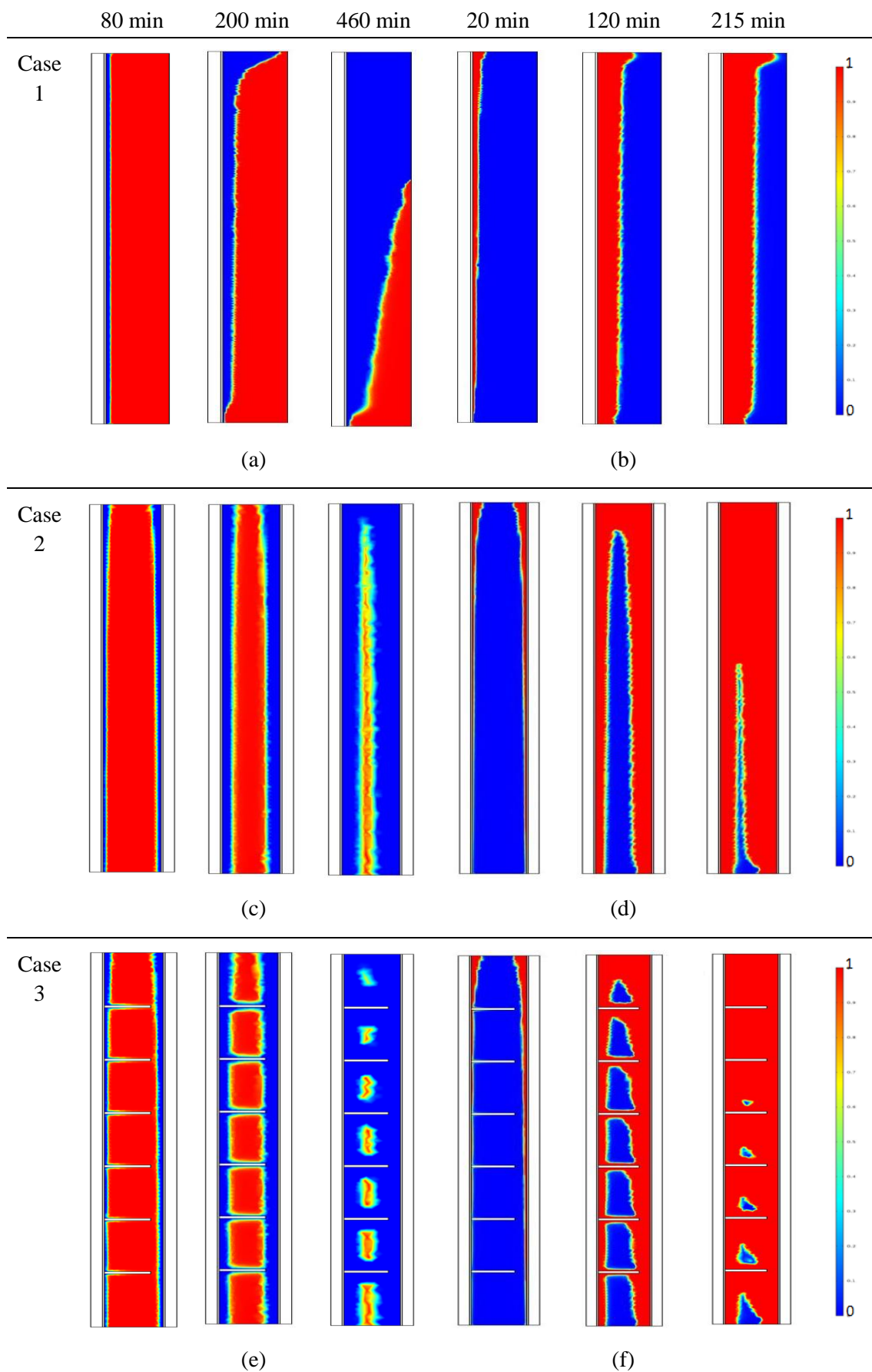
Fig. 4.9 - Phase evolution of PCM during charge and discharge process

Fig. 4.9 shows the phase change evolution of the PCM during charge (a,c,e) and discharge (b,d,f) processes. The figures show a cross section of the TES in which the inner tube is on the left side while the wall (Case 1) or the outer tube (Case 2-3) are on the right side. The red area represents the solid phase of the PCM material, the blue area represents the liquid phase. It can be observed that the solid-liquid interface moves in different time steps depending on the different geometrical configurations. It is evident that Case 2 and Case 3 have a more homogeneous heat transfer rate with respect to Case 1. After 80 min (see also figure 4.8), the solid-liquid interface starts to form at the top of the TES, where the HTF enters and along the entire length of the inner tube (Case 1) and of the inner and outer tubes (Cases 2-3). Fig. 4.9e shows that for this time step a film of liquid PCM starts to form also around the fins. After 200 min it is possible to note the different characteristics of the solid-liquid interface for the three cases on account of their different configurations. In Case 1 the solid-liquid interface moves parallel and radially from the centre to the peripheral wall. On the top of the TES device it is possible to observe a larger area of liquid PCM, owing to the proximity of the HTF inlet, while a smaller area appears on the bottom. In Case 2 the interface assumes a kind of monotonic shape (Fig 4.9c,d), while in Case 3 various cells with liquid PCM form during the process (Fig. 4.9e,f). In Case 1, after 460 min of charge, a large area of solid material can still be seen (Fig. 4.9a) while, in Case 2 only a narrow portion in the mid part of TES device remains in solid phase (Fig. 4.9c). For Case 3, the solid PCM forms small spots into the cells between the fins (Fig. 4.9e). A similar behaviour can be seen for the discharge phase, but the time to reach complete melting is lower with respect to the charge phase.

(a)   (b)
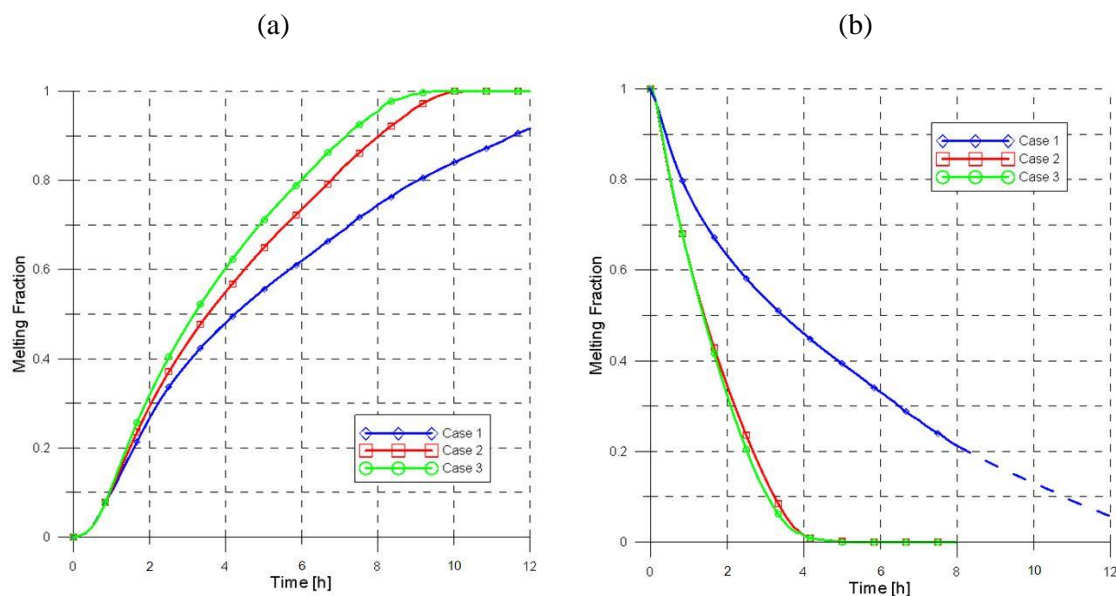
Fig. 4.10 - Melting Fraction for charge (a) and discharge (b) processes.

Figure (4.10) presents the PCM melted fraction versus time for the charge (a) and discharge (b) processes. This parameter is defined as the volume of PCM in liquid phase divided by the total volume occupied by the PCM. By definition, the melted fraction is 0 at the beginning of the charge process and 1 at the beginning of the discharge process. As mentioned, the lowest melting and solidification time was obtained for Case 3. Moreover, it is evident that Case 1 does not reach complete melting and solidification after 12 and 8 hours of charge and discharge respectively. The

dashed line again refers to the condition where Case 1 continues for 12 hours as for the charge phase. For Cases 2-3, in the charge phase the melting fraction is equal to 1 after about 9-10 hours and the whole PCM is in the liquid phase. At the same time, for Case 1 the melted fraction is between 0,80-0,84. In the discharge phase, after about 5 hours the melting process is complete for Cases 2-3, while at the same time the value of the melting fraction is about 0.40 for Case 1.

All these considerations will be better in-depth in the following paragraphs where the comparison between the two approaches is presented.

Furthermore, the effect of the number of fins on the melting rate was investigated comparing five different cases. Case A is the reference case and it corresponds to the triplex heat exchanger without fins already discussed in the previous paragraphs. The number of fins of the others cases are reported in table 4.5.

The results previously presented in Figures 4.10(a,b) show that the fins influence the melting fraction especially in the charge phase (fig.4.10a) where the difference between the Case 2 and 3 is considerable, while for the discharge phase this difference is not appreciable. Thus, this comparative analysis was carried out only for charge process. The melting time is expressed as a percentage of total time with respect to the case without fins (Case A).

Table 4.5 - Number of fins and melting times for five different cases analyzed
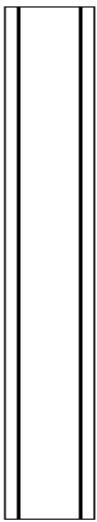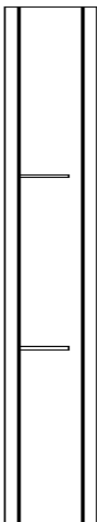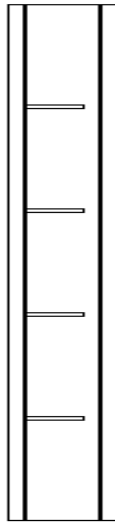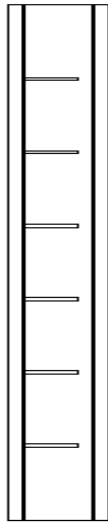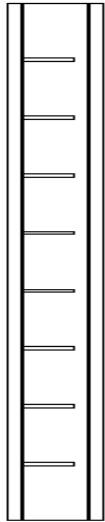
	Case A	Case B	Case C	Case D	Case E
Number of fins	0	2	4	6	8
Melting Time [min]	440	426	394	372	358
Melting Time %	100	96.8	89.6	84.6	81.4
ΔMT %	-	-3.2	-7.2	-5	-3.2

Figure 4.11 shows the effect of the number of fins in the melting fraction for the tested cases. It can be seen that the melting time of PCM decreases increasing the number of fins. Taking as reference the 85% of the total melting fraction, the melting times were evaluated with respect to the TTHX without fin (Case A). The complete melting time for Cases B, C, D and E were respectively as reported in table 4.5.

A significant influence of the number of fins on the melting fraction was founded. The greater the fins number, the lower the melting time, since, obviously, the fins extend the heat transfer area and increase the heat transfer rate between the inner tube and the PCM.
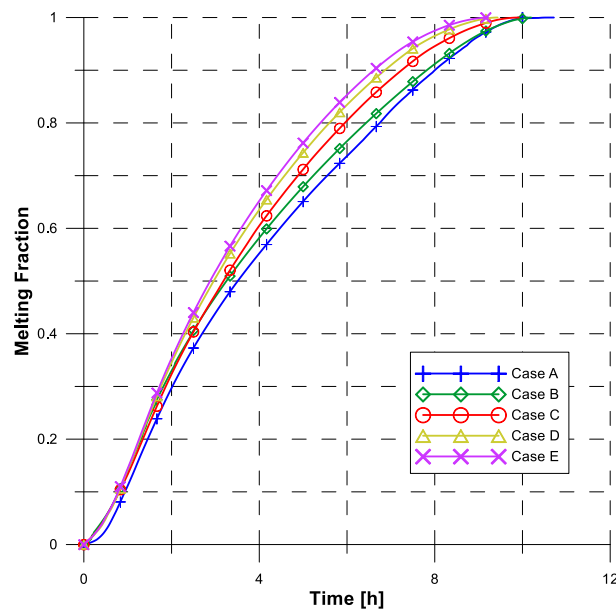
Fig. 4.11 - Number of fins effect to the melting time

A reduction of 18.6% was found between the Case A and Case E. The 85% of melting for Case A was reached in 440 min (7.3 h), thus the addition of 8 finned surfaces inside the storage system involves a decrease of the melting time for the same percentage equal to 82 min (1.4 h).

The relative percentage difference of melting time $\Delta MT\%$ increases for Case B and C, while for Case D ad E decreases. A maximum value of -7.2% is achieved for Case C (four fins) whereby, the relative improvement decrease with increasing the fins number. In fact, on the one hand the fins increased heat transfer rate by increasing the total surface area available for heat transfer by conduction, on the other hand high number of fins reduces the formation of convective cells decreasing the amount of heat transfer by convection.

It can be concluded that the number of fins has a significant effect on the PCM melting process that it must be takes into account using finned surface.

In future works, an optimization with respect to the number, the distance, the thickness, the length and the shape of the fins will be carried out, as well as the effects of different flow rate and fins number on the TES thermal performance will be studied.

4.5 Validation of the 2D axysimmetric model: comparison between the two approaches

4.5.1 Material and method

In order to evaluate which of the two proposed approaches shows more accuracy during charge and discharge processes, a comparison with the results obtained by experimental tests was performed. Experimental tests were carried out in the laboratories of the research center GREA Innovació Concurrent (University of Lleida, Spain) on a small scale heat exchanger used as TES device [60].
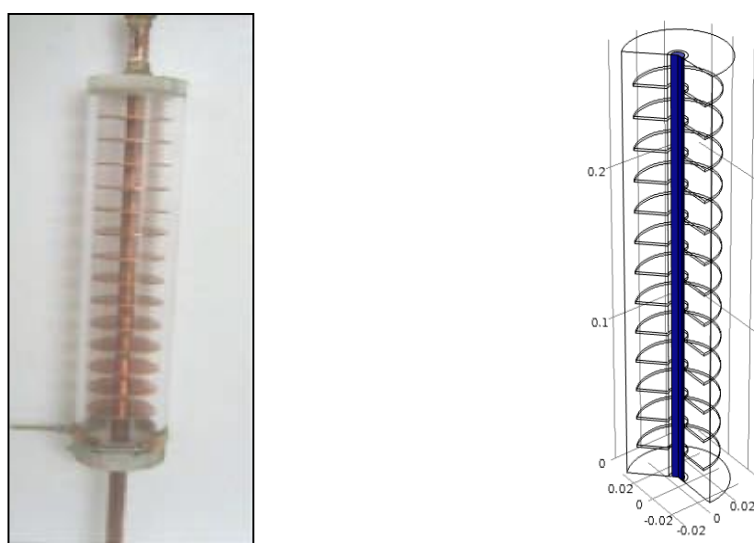
Fig. 4.12 - Double tube heat exchanger with fins (a), geometric configuration of TES system implemented in COMSOL Multiphysics (b).

The TES device is based on the configuration of double pipe heat exchanger with 13 radial copper fins. The inner tube is copper while the outer is made of transparent material (methacrylate), that allows a direct view of the phase transition process. Figure 4.12 shows a picture of the TES (a) and the geometric configuration implemented in COMSOL Multiphysics (b). The geometrical characteristics of the TES are shown in Table 4.6.

Table 4.6 - Geometrical characteristics of storage system

	Units	*Value*
External diameter HTF tube	m	0.012
Height	m	0.26
Width HTF tube	m	0.002
External diameter PCM tube	m	0.065
Width PCM tube	m	0.006
Number of fins	-	12
Diameter fins	m	0.052

Width fins	m	0.0015
Heat transfer area	m2	0.065
PCM mass	kg	0.5

Commercial paraffin RT35 from Rubitherm® Technologies GmbH was used as PCM filling the external tube of the heat exchanger and water circulates through the internal tube as heat transfer fluid. The main physical properties of this PCM [61] [62] are shown in Table 4.7.

The potential applications in the operative temperature range (35-40 °C) of this type of TES are related to small-sized systems, such as telecommunication devices or home appliances, for making them more energy efficient.

Table 4.7 - Properties of Rubitherm RT35

	Solid	Liquid
Density (kg/m^3)	880	760
Specific heat (kJ/kgK)	1.800	2.400
Thermal conductivity (W/mK)	0.2	0.2
Phase change temperature	35°C	
Latent heat	157 kJ/kg	

Fig. 4.13 shows a schematic diagram of the experimental set-up. The set-up consists of a thermostatic bath HUBER K25 that controls water inlet temperature, a water pump WILO and a series of valves to control water flow rate, a digital flow meter Badger Metter Prime Advanced (range of 0.85–17 l/min, accuracy of 0.25% for velocities below 5 m/s and 1.25% for higher values) and a system for temperature measurements based on Pt100 DIN-B probes. Both temperature and flow rate readings are collected in a computer via the data acquisition system STEP DL01-CPU.
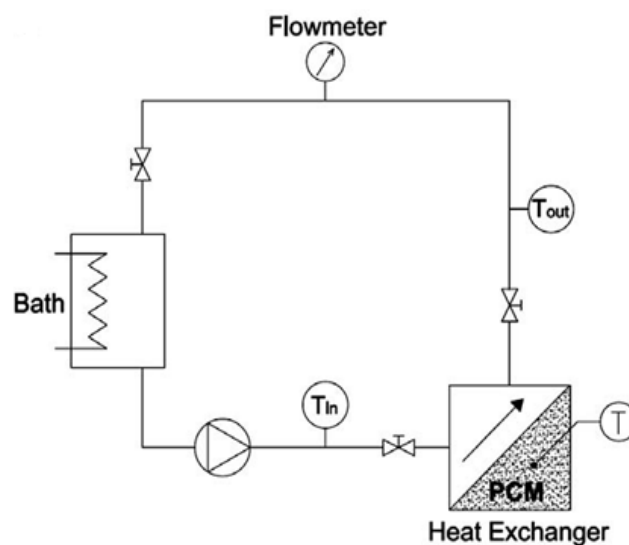
Fig. 4.13 - Diagram of experimental set-up

Working conditions were chosen to achieve temperature gradients of 25 and 15 °C between water inlet and PCM melting point during charge and discharge respectively. The charge phase was performed using two volumetric flow rate values in order to have laminar and turbulent regimes, while the discharge phase was carried out by means of the larger volumetric flow rate value for both experiments. In all cases, the HTF enters from the upper side of the TES. The specific conditions used in the experiments are presented in Table 4.8.

Table 4.8 - Summary of charging and discharging experiments carried out.

	Experiment 1		Experiment 2	
	Charge	Discharge	Charge	Discharge
Volumetric flow rate (m^3/h)	0.03	0.4	0.4	0.4
Reynolds Number	1600	22000	22000	22000
HTF temperature (°C)	60	20	60	20

A 2D axisymmetric numerical model using both approaches was developed with the COMSOL Multiphysics platform to simulate the heat exchanger during the phase change processes. The equations used to model the PCM behaviour are described in the paragraph 4.3 for the first approach and in paragraph 4.4 for the second approach.

The discharge of experiment 1 and the entire process of experiment 2 are characterized by turbulent flow in HTF domain. Considering turbulent flow, Reynolds-averaged Navier-Stokes (RANS) equations were considered the model. The use of RANS equations involves a refined mesh specially at the boundary layer in order to allow the model to predict the transition from laminar to turbulent flow. In this case, the mesh adopted for both laminar and turbulent flow was chosen extremely fine (Fig. 4.19), thus no further mesh refinement was necessary.

The particular RANS model used in this study was the k-ε model. This model is suitable for incompressible flows, and compressible flows at low Mach number (typically less than 0.3). The equations solved by the k-ε method are the continuity equation (4.15) and the momentum equation (4.16). The model introduces two additional transport equations and two dependent variables: the turbulent kinetic energy, k (Eq. 4.22), that determines the energy of the turbulence and the turbulent dissipation rate, ε (Eq. 4.23) that determines the scale of the turbulence. The turbulent viscosity is modeled as given by Equation 4.21:

$$\mu_T = \rho C_\mu \frac{k^2}{\varepsilon} \tag{4.21}$$

$$\rho \frac{\partial k}{\partial t} + \rho u \cdot \nabla k = \nabla \cdot \left(\left(\mu + \frac{\mu_T}{\sigma_k} \right) \nabla k \right) + P_k - \rho \varepsilon \tag{4.22}$$

$$\rho \frac{\partial \varepsilon}{\partial t} + \rho u \cdot \nabla \varepsilon = \nabla \cdot \left(\left(\mu + \frac{\mu_T}{\sigma_\varepsilon} \right) \nabla \varepsilon \right) + C_{\varepsilon 1} \frac{\varepsilon}{k} P_k - C_{\varepsilon 2} \rho \frac{\varepsilon^2}{k} \tag{4.23}$$

where

- – u is the velocity vector [m/s]
- – ρ is density [kg/m^3]
- – P is pressure [Pa]
- – μ is the dynamic viscosity [Pa·s]
- – μ_T is the turbulent (or eddy) viscosity
- – C_μ, $C_{\varepsilon1}$, $C_{\varepsilon2}, \sigma_k, \sigma_\varepsilon$ are dimensionless model constants [63] [64]
- – ε is the turbulence dissipation rate
- – k is the turbulence kinetic energy
- – t is the time [s]

Table 4.9. - Value of Rans model costants [63] [64]

Constant	Value
C_μ	0.09
$C_{\varepsilon1}$	1.44
$C_{\varepsilon2}$	1.92
σ_k	1.0
σ_ε	1.3

The production term P_k is given by Equation 4.24:

$$P_k = \mu_T \left(\nabla u : (\nabla u + (\nabla u)^T) - \frac{2}{3}(\nabla \cdot u)^2 \right) - \frac{2}{3}\rho k \nabla \cdot u \qquad (4.24)$$

4.5.2 Results and discussion

The comparison between the experimental results and the two discussed approaches was carried out. Figure 4.14 shows the PCM temperature profiles for charge (a) and discharge (b) process. As said before, two experiments were performed using different volumetric flow rate values. Red curves represent the first approach, that is the method in which heat transfer by only conduction is considered. Blue curves represent the second approach, that is the method in which heat transfer by both conduction and natural convection is considered. The time of the charge process for the two experiments was imposed equal to 900 and 1600 seconds respectively, while the time of discharge process was imposed equal to 2100 seconds for both the experiments. The temperature measurement was taken in a centered position in the PCM domain, near the outer wall in the radial direction and half way between inlet and outlet in the axial direction.
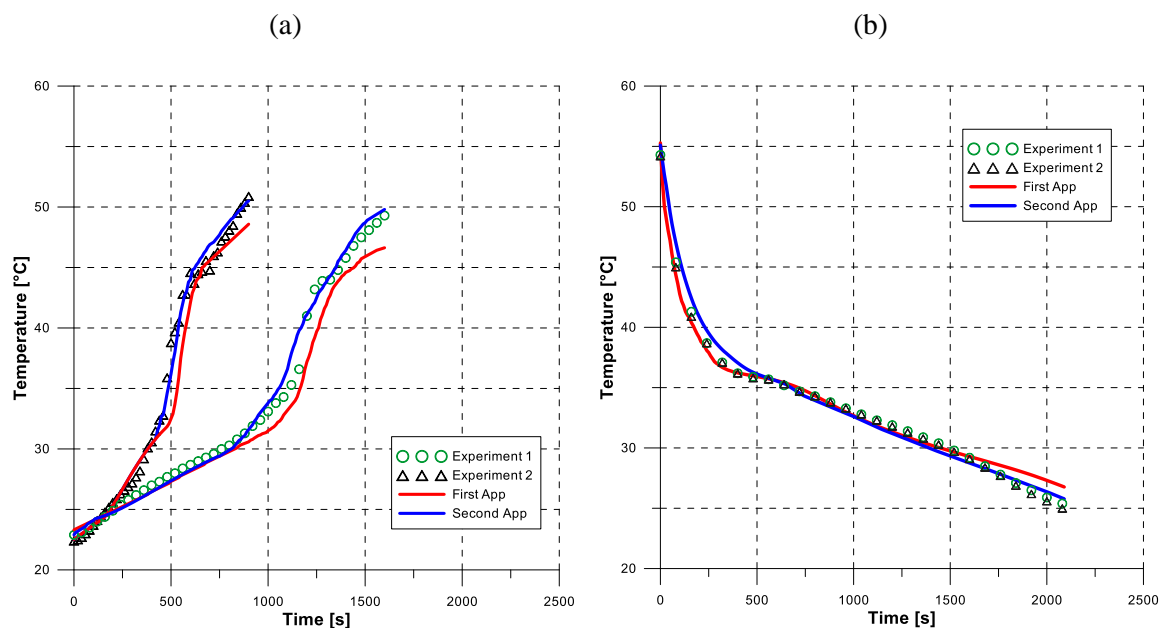
Fig. 4.14 - PCM temperature profile for charge (a) and discharge (b) processes.

It is possible to note that the second approach is more accurate because it is closer to the experimental results. Fig. 4.14a shows that at the beginning of the charge process, up to 800 and 400 seconds for experiment 1 and 2 respectively, both approaches demonstrate good accuracy with respect to the experimental results. After, the second approach presents approximately the same temperature values of the experimental results while the first approach differs of about 2-3 °C even if it maintains the same trend. Conversely, during discharge (Fig. 4.14b) the numerical predictions of both approaches appear very close to the experimental results. This can be explained by the different nature of the heat transfer phenomena that take place during melting or solidification. In the case of solidification, conduction is the only heat transfer mechanism, while in the case of melting, natural convection occurs in the melt layer dominating the heat transfer process and this generally increases the heat transfer rate compared to the solidification process.

The following figures present the PCM melted fraction versus time for the charge (Fig. 4.15a) and discharge (Fig. 4.15b) processes. As said before, this parameter is defined as the volume of PCM in liquid phase divided by the total volume occupied by the PCM and it can assume values between 0 (only solid PCM) and 1 (only liquid PCM).

(a)   (b)
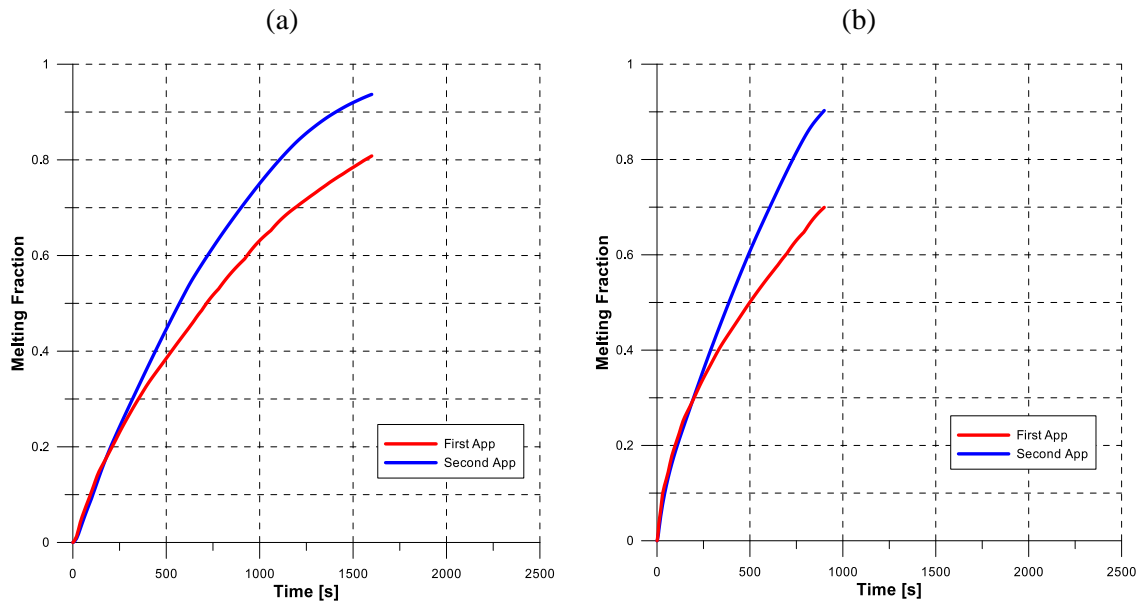
Fig. 4.15 - Melting process for experiment 1 (a) and experiment 2 (b) during charge process

At 1600 second, the value of melting fraction for experiment 1 (Fig. 4.15a) during charge is approximately 0.8 and 0.94 for the first and second approach respectively. For experiment 2, at the end of charge (900 seconds) this value is about 0.7 and 0.9 for the first and second approach respectively (Fig.4.15b). At the end of discharge phase (2100 seconds) the melting fraction reaches the value of about 0.2 and 0.16 for the first and second approach respectively (Fig.4.16). It is clearly seen that for the charge process, the difference between the two approaches is considerable because during melting the heat transfer is strongly influenced by convection, while for discharge the two curves are very similar, because during solidification the heat transfer is dominated by conduction.
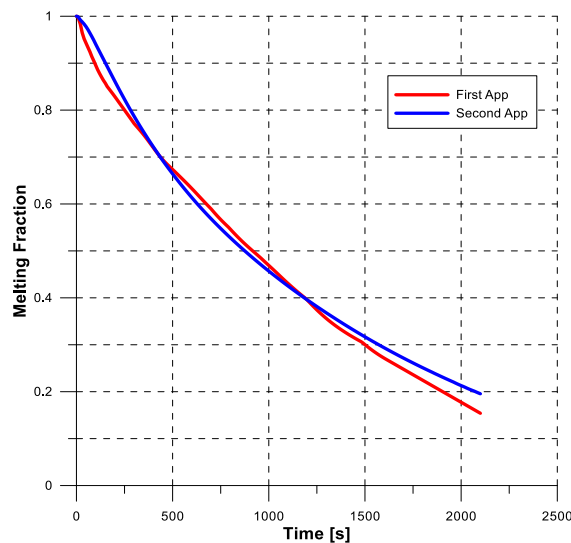
Fig. 4.16 - Melting fraction for both approaches during discharge process

This is also evident in figure 4.17 that presents the phase change evolution of the PCM for both experiments and both approaches during charge and discharge processes. The figures show a cross section of the TES in which the inner tube is on the left side while the wall are on the right side. The red area represents the solid phase of the PCM material, the blue area represents the liquid phase.

Exp. 1, First Approach - Charge (a)   Exp. 1, Second Approach - Charge (b)

250 s   800 s   1600 s   250 s   800 s   1600 s

Exp. 2, First Approach - Charge (c)   Exp. 2, Second Approach - Charge (d)

250 s   450 s   900 s   250 s   450 s   900 s

First Approach - Discharge (e)   Second Approach - Discharge (f)

250 s   1050 s   2100 s   250 s   1050 s   2100 s
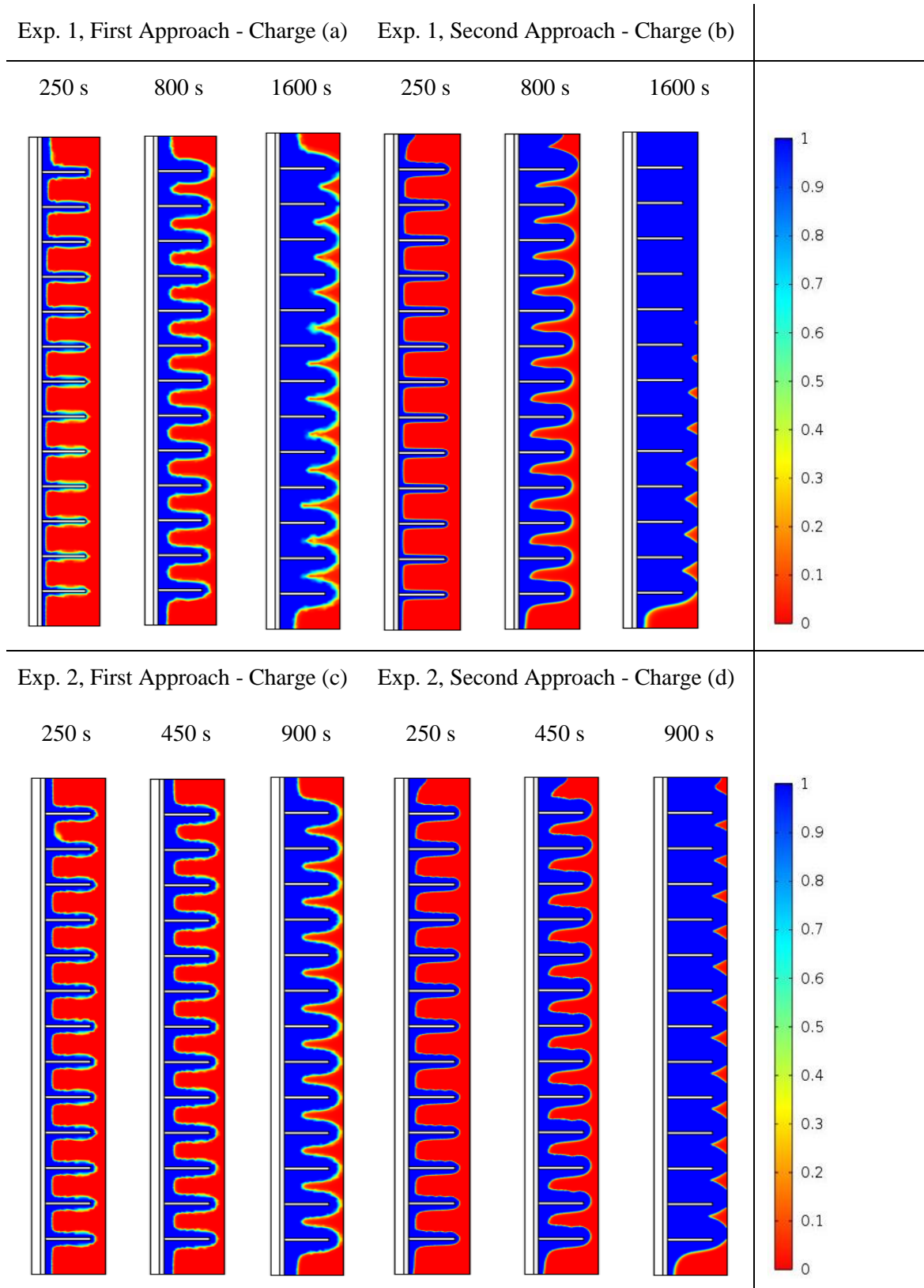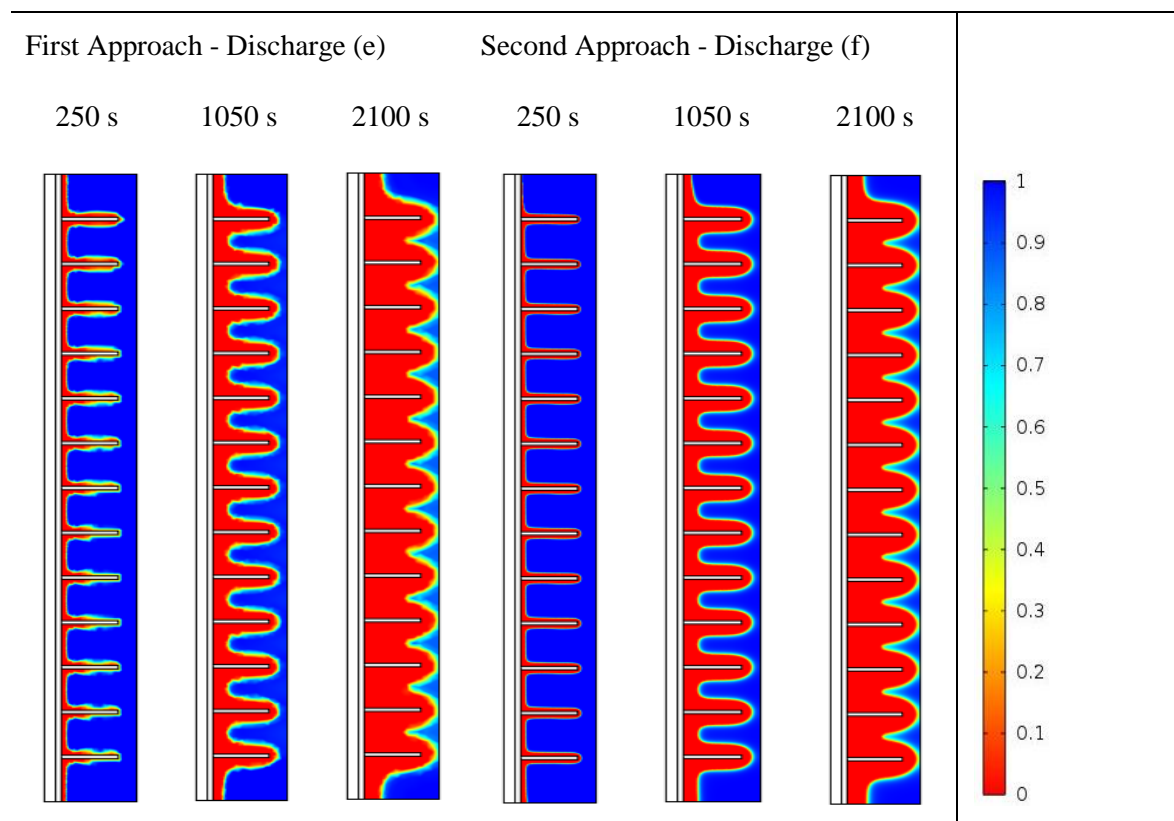
Fig. 4.17 - Phase evolution of PCM for both experiments and for both approaches during charge and discharge process

At the beginning of both charging and discharging processes, the solid-liquid interface starts to form at the top of the TES, where the HTF enters, along the entire length of the inner tube and around the fins. It is found that natural convection in the melt region as well as heat conduction in the solid region considerably influence the interface shape and motion during both the melting and solidification processes. Figures 4.17a,b show the phase evolution of PCM during charge for experiment 1 (flow rate equal to 0.03 m³/h) for first approach (Fig. 4.17a) and second approach (fig. 4.17b). At the beginning, the process is dominated by conduction. The solid-liquid interface moves almost parallel to the heating surface (the inner tube), then when the liquid phase increases, the influence of natural convection become much strong. After 800 seconds, convection heat transfer has a higher contribution in melting and helps in increasing the heat transfer rate within the PCM domain with respect to only conduction. In fact, it is evident that PCM reaches almost complete melting after 1600 second of charge while with the first approach there is still a solid PCM fraction near the outer tube. A similar behaviour can be seen for the charge phase of experiment 2. As an example, figure 4.18 presents the amplitude and direction of the velocity inside the liquid PCM (red arrows) at 600 seconds for experiment 1. The blue line now shows the solid-liquid interface. As expected, it can be seen that when the liquid PCM touches a hot surface of the inner tube, buoyancy forces carries it upward, while when it touches a cooler surface of the solid PCM or of the outer tube it moves downward forming convective cells.

For discharge phase (fig. 4.17e,f), the two approaches present very similar results. After 2100 seconds the solid-liquid interface is approximately in the same position for both cases. In fact, during discharge conduction dominates the heat transfer process, thus the influence of natural

convection is very low. Furthermore, finned surfaces enhance the internal heat transfer of a phase change storage, thus the presence of the fins improves heat transfer by conduction further reducing the contribution of convection. The nearer the fins, the lower the effect of natural convection when conduction takes place as the leading heat transfer mode in a solidification process. Whereby, as said in paragraph 4.4.3, the presence of the fins has a great influence on the phase change process.
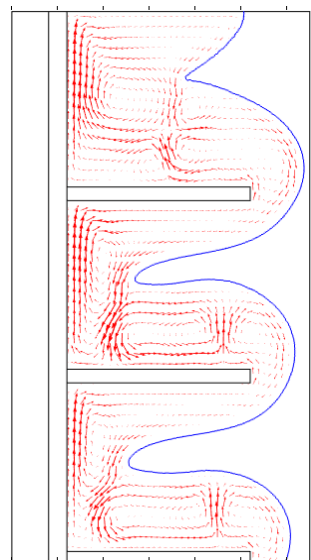
Fig. 4.18 - Convection cells within PCM during melting process at 800s for experiment 1

Heat transfer mode also influences the shape of the solid-liquid interface. In the first approach, in which only heat transfer by conduction was considered, the solid-liquid interface moves parallel from the centre to the wall of outer tube. Instead, in the second approach, in which heat transfer by conduction and natural convection were considered, this boundary is not parallel with the inner tube but it curves gradually from the top, inward during melting (Fig. 4.17b,d) and outward during solidification (Fig. 4.17f). In fact, the presence of gravity, heterogeneous temperature field and heterogeneous density generate buoyancy force in liquid PCM domain which allows the formation of this particular shape of the solid-liquid interface.

As said before, the second approach is more accurate because it is closer to the experimental results. However, it is important to compare the required computation times and the mesh for the two proposed approaches.

Table 4.9 - Summary of the model simulations to compare the two approaches studied.

	First Approach			Second Approach		
	Charge Exp. 1	Charge Exp. 2	Discharge Exp. 1-2	Charge Exp. 1	Charge Exp. 2	Discharge Exp. 1-2
Duration of simulation (real time)	22 h	10.8 h	5.5 h	156.1 h	80.8 h	56.4 h
Physical time (simulation time)	1600 s	900 s	2100 s	1600 s	900 s	2100 s

Table 4.9 shows that the time elapsed during the execution of the simulations for the second approach are 7 and 10 times greater than those related to the first approach for charge and discharge processes respectively. In fact, 22 hours were required to complete the first experiment using the first approach, while 156.1 hours were required to complete the same experiment using the second approach. The computation is performed on a ASUS workstation with I7 Quad-Core CPU and 16 GB memory. Basically, this difference depends on the increasing complexity due to solve the continuity (15), momentum equations (16) and buoyancy forces used to simulate the behaviour of the PCM in liquid phase. In fact a finer mesh was required using the second approach and consequently more computation time was needed.

(a)   (b)
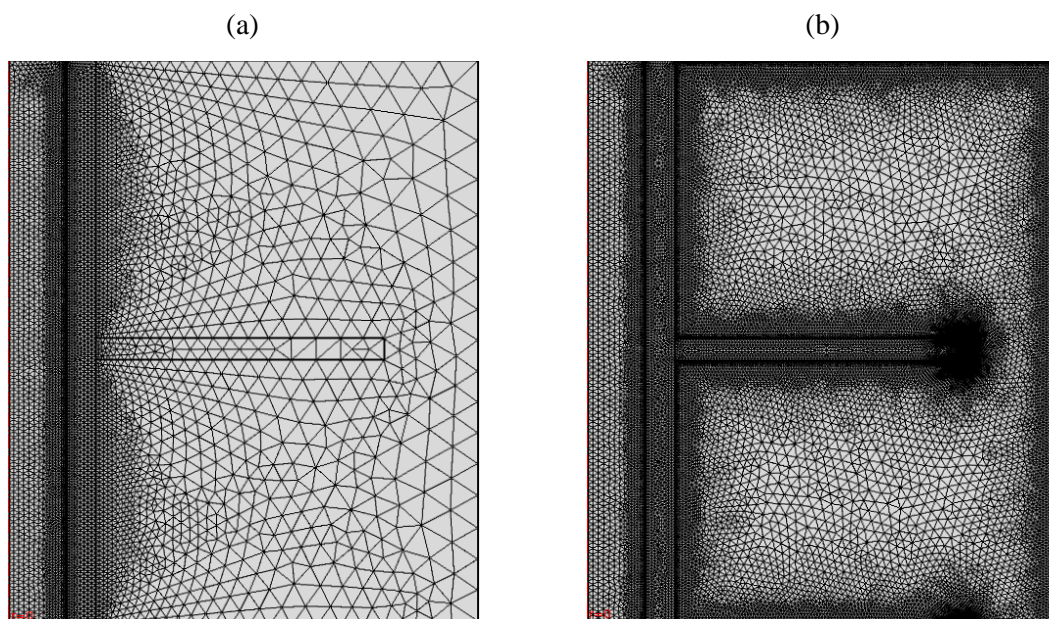
Fig. 4.19 - Free triangular mesh used for first approach (a) and second approach (b)

For all models, a free triangular mesh geometry was selected using 63252 elements and 3428 boundary elements for the first approach (Fig.4.19a), while 255687 elements and 7824 boundary elements for the second approach (Fig. 4.19b).

4.6 Conclusions

Numerical study of latent heat thermal energy storage device were presented in chapter 4, using 2D and 3D numerical simulation codes specifically implemented in the COMSOL Multiphysics environment. Two different approaches were analyzed to perform the behavior of PCM during phase transition. The first approach considers heat transfer only by conduction in both solid and liquid PCM phases. The second approach considers heat transfer by conduction and natural convection in liquid PCM domain. To model the phase transition, the apparent heat capacity formulation was used in both approaches. In this method, the latent heat is implemented by increasing the heat capacity of the material, while the phase change process is modelled by assuming that the transition takes place in a narrow range of temperature rather than at a fixed temperature.

A 3D numerical simulation code was presented in paragraph 4.3 and developed to analyze behaviour and performance of a thermal energy storage systems with phase change materials using the first approach, i.e. heat transfer only by conduction in PCM liquid domain was considered. The configuration of shell and tube heat exchanger was selected to design the TES and Hydroquinone was used as PCM. This configuration has been chosen for the storage device that will be implemented in the laboratories for TES technologies of the DIMCM-University of Cagliari. The heat exchange between the HTF and PCM simulating the phase transition, but also the fluid dynamics of the HTF inside the tubes of the storage system was carefully studied and evaluated. The configuration of the storage system has led to an uniform distribution of the heat flow across the surface of the tank. The results obtained show that the complete transition was reached in about 2 hour for charging process and 1 hour for discharging process. On the other hand, the PCM nearest to the shell was the last that undergoes the transition in both charge and discharge phases. With the first approach, the convection and the buoyancy force in liquid PCM domain were not considered, so the solid-liquid interface moves around the tubes uniformly. The shape of this boundary and the melting and solidification time depend on the heat transfer process considered.

In paragraph 4.4, a 2D axysimmetric numerical model based on the second approach was presented. Three different geometrical configuration of a TES system were studied and compared to identify the best solution as regards thermal energy storage with PCM materials. A double tube (Case 1), a triplex (Case 2) and a triplex with circular fins (Case 3) were analyzed to evaluate temperature and phase distribution in both charge and discharge phases. It was found that the different configurations of the three systems considered had a strong impact on the performance of the phase change process. In Case 1 the solid-liquid interface moved parallel and radially from the centre to the wall of the TES. In Case 2 the interface assumed a monotonic shape, while in Case 3 various cells with liquid PCM formed during the process. As expected, the triplex heat exchanger (Cases 2 and 3) were the solutions that allowed the faster response of the TES device during the charge and discharge processes. The insertion of fins (Case 3) allowed, in particular, not only an increase in the heat exchange surface of the inner HTF tube, but also the creation of cells in the PCM volume that determined faster melting/solidification of the PCM. A time of 12 and 8 hours was considered as a reference period for charge and discharge respectively. In this period, complete melting and solidification of the PCM was achieved only in Cases 2 and 3. A melted fraction for both phases was analyzed. For charge process, a complete melting was achieved in about 9-10 hours in Cases 2 and 3, while a value of about 80-84% of PCM liquid fraction was reached in Case 1 in the same time interval. For discharge process, a complete solidification was achieved in about 4 hours in Cases 2-3, while a value of about 40% of PCM solid fraction was reached in Case 1. The second approach was used in this model, thus heat transfer by both conduction and natural convection was calculated in PCM domain. The role of natural convection involves not only the heat transfer rate during melting process but also the shape of the solid-liquid interface. In fact, using the first approach the solid-liquid interface moves uniformly around the tubes while, the second approach takes into account the buoyancy forces that modify the shape of the interface.

Furthermore, the effect of the number of fins on the melting rate was investigated comparing five different cases (0, 2, 4, 6, 8 fins). A big influence of the fins number on reducing the melting time was found. Considering the 85% of total melting, a reduction of 18.6% of melting time was estimated for the case with 8 fins with respect to the case without fins. The relative percentage difference of melting time $\Delta MT\%$ presents a maximum value of -7.2% for TES with four fins, while for higher number of fins this parameter decreases. Whereby, on the one hand the fins

increased heat transfer rate by increasing the total surface area available for heat transfer by conduction, on the other hand high number of fins reduces the formation of convective cells decreasing the amount of heat transfer by convection.

In paragraph 4.5, the validation of the two proposed approaches was carried out through a comparison with the results obtained by experimental tests. The transient behaviour of a LHTES system based on the configuration of a finned double tube heat exchanger filled with paraffin RT35 as PCM was investigated. The first approach takes into account the heat transfer only by conduction in liquid PCM domain. The second approach takes into account the heat transfer by heat conduction and natural convection in liquid PCM domain and also, the Boussinesq approximation was introduced to consider the buoyancy forces. In order to evaluate which one of the two proposed approaches show more accuracy during charge and discharge processes, a comparison with the results obtained with two experimental tests was carried out. These tests were performed in the laboratories of the research center GREA Innovació Concurrent (University of Lleida, Spain). Overall, a good agreement with the experimental temperature profiles during charge and discharge phase was obtained. However, it was found that heat transfer mode influences the interface shape and motion during both the melting and solidification processes. In fact, natural convection in melt region drives and improves the heat transfer rate increasing the velocity of the solid-liquid interface. A time of 1600 and 900 seconds was considered as a reference period for the charge phase of experiment 1 and 2 respectively, while a time of 2100 seconds was considered for discharge phase of both experiments. At the end of charge phase, the temperature profile obtained with the second approach shows a good agreement with respect to the experimental results, while the first approach is less accurate. Instead, the numerical prediction of both approaches appears very similar to the experimental results during discharge process. A melted fraction for both phases was analyzed. For experiment 1, melting fraction values of 0.8 and 0.94 were reached at the end of charge for first and second approach respectively, while for experiment 2, melting fraction values of 0.7 and 0.9 were reached at the end of charge for first and second approach respectively. At the end of discharge, melting fraction values of 0.16 and 0.2 were obtained for first and second approach respectively for both experiments. These differences can be explained considering that the different nature of the heat transfer phenomena that take place when a PCM melts or solidifies. During charge the difference between the two approaches, evenly considering the temperature profile or the melting fraction, is high because in melting process the heat transfer is dominated by convection, while during the discharge the results are very similar, because in solidification process the heat transfer is dominated by conduction. Furthermore it was found that the two approaches had a strong impact on the shape of the solid-liquid interface. In the first approach solid-liquid interface moves parallel and radially from the centre to the wall of the TES, while in the second approach, natural convection and buoyancy force this boundary slopes gradually from the top, inward during melting and outward during solidification. Finally, first approach was simple and required relatively low computational resources but it has proven less accurate. A good fitting was obtained using the second approach that was more closer to the experimental results thus, natural convection plays a significant role in phase change process and it must be taken into account. The effects of natural convection on the shape and the motion of solid-liquid interface can not be neglected. However, it must be considered that the addition of natural convection implies a major requirement of computational resources.

Chapter 5

Project design and implementation of a TES test rig

5.1 Introduction

The project, design and implementation of a test rig was carried out to investigate thermal energy storage systems within the laboratory for TES technologies of the Department of Mechanical, Chemical and Material of the University of Cagliari. In particular an accurate selection of test rig components was specifically chosen for experimental investigation of latent heat thermal storage devices.

The experimental facility was designed not only to be an important tool for the research activity in order to validate the developed numerical models, but also for the experimental investigation applied to medium-high temperature industrial processes. For these reasons, a PCM-TES prototype was specially designed and build as latent heat thermal energy storage device based on the configuration of shell and tube heat exchanger. D-Mannitol was selected as PCM material while silicone oil Syltherm 800 was selected as HTF. D-Mannitol and Syltherm 800 were already presented in chapter 4. The operating parameters of the test rig are reported in table 5.1:

Table 5.1 - Operating parameters of the test rig	
Temperature Max	350 °C
Pressure Max	15 bar
Nominal pressure	12 bar
HTF Flow-rate [min- Max]	0.5-3 m^3/h

At the time of writing the test rig is already build while the storage system is still under construction.

5.2 Design and implementation of the LHTES test rig

The test rig consists of the following components as reported in figure 5.1:

    A. Electric heater
    B. Air cooler
    C. Latent heat thermal energy storage device

D. Fluid Circulation Pump
E. Thermal Fluid Expansion Tank
F. Pump empty/full
G. Air Separation Unit

The pump circulates the HTF within the plant during the charging and discharging processes. During charge, the HTF is heated by the electric boiler until the operating temperature conditions. Then it enters the TES system releasing thermal energy to the PCM. A valves by-pass system allows to the continuous recirculation of the HTF avoiding to passing into the air cooler. During discharge, cold HTF enters the TES absorbing the thermal energy accumulated by the PCM, then it flows into the air cooler considered as the thermal user.
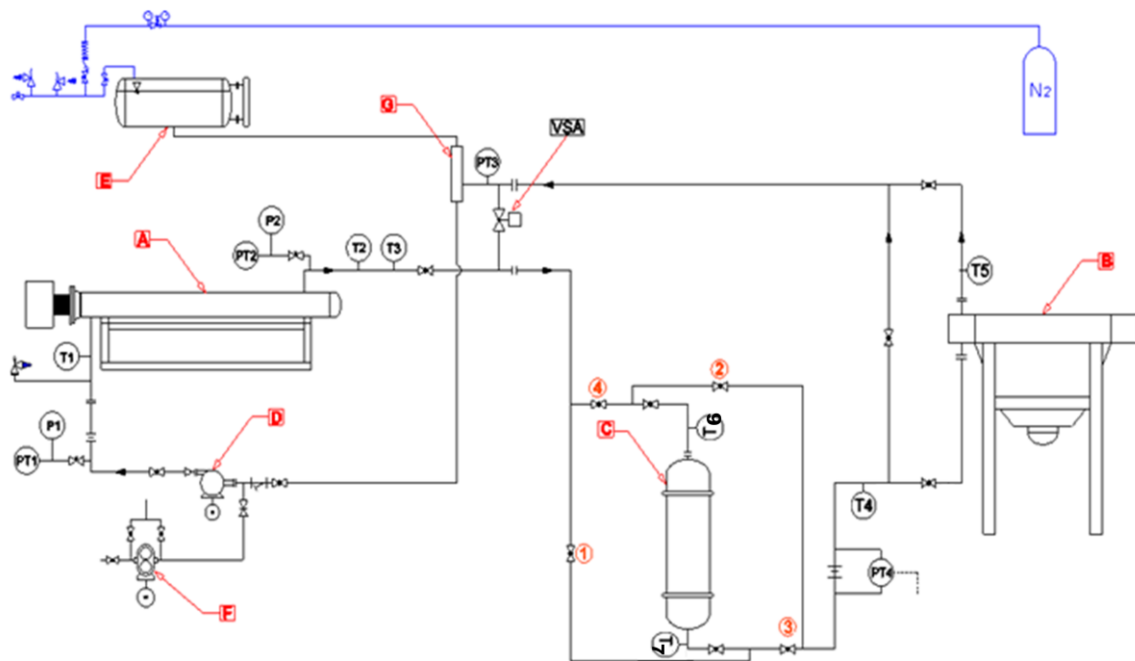
Fig. 0.1 - Test rig layout

Figure 5.1 shows the test rig layout. HTF temperature and pressure are measured in different sections of the facility by temperature (indentified with *T* in figure 5.1) and pressure (identified with *PT* in figure 5.1) sensors.

The pump circulates the HTF within the plant during both charge and discharge processes. Two shut-off valves, located one before and one after the pump, allow to isolate the pump when it is necessary (e.g. for maintenance). Then the HTF is heated up to the operating conditions inside the electric boiler.

A servo-actuated valve (identified with *VSA* in Figure 5.1) located at the exit of the boiler allows to control the HTF flow rate that circulates in the "storage pipes" (it consist of TES and aircooler) or "skid pipes" (it only consist of heater and pump) admitting three operating conditions:

– Valve fully closed (0%): full HTF flow rate is available to the TES and the thermal user (the aircooler).

- Valve fully open (100%): full HTF flow rate is not available to the TES and the thermal user but it is recirculated inside the heater skid.
- Valve partially open (x%): part of HTF flow rate flows to the TES, part of the HTF recirculates inside the skid.

Figure 5.2 shows the valves system used to modify the direction of the HTF at the inlet of the TES. In fact, this system allows two different HTF inlet direction modes (figure 5.3a,b): in the first, the HTF enters from the top of the storage system while in the second, the HTF enters from the bottom.
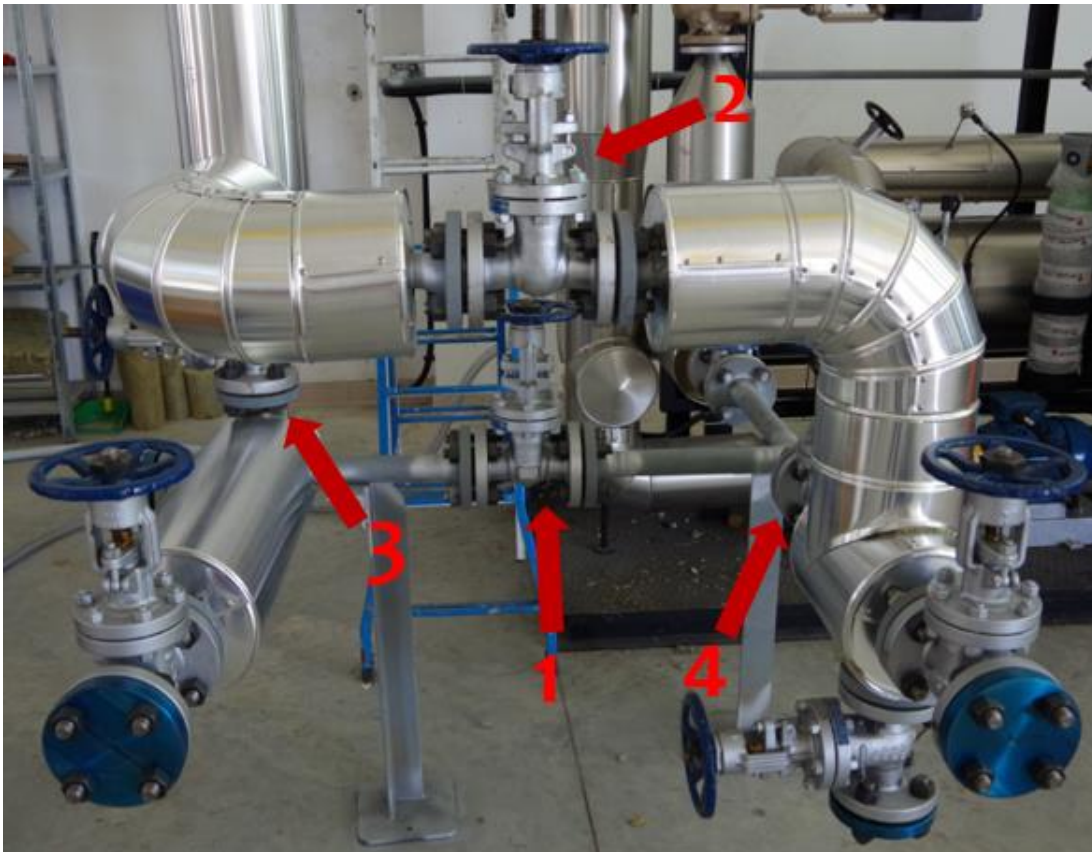
Fig. 5.2 - Valves system to modify the direction of the HTF at the inlet of the TES

The first mode is achieved by closing of valves 1 and 2 and opening of valves 3 and 4 (fig. 5.2). In this condition the HTF enters the TES from the upper part as reported in figure 5.3a. The second mode is achieved by opening valves 1 and 2 and closing valves 3 and 4 (fig. 5.2). In this condition the HTF enters the TES from the bottom as reported in figure 5.3b.

(a)   (b)
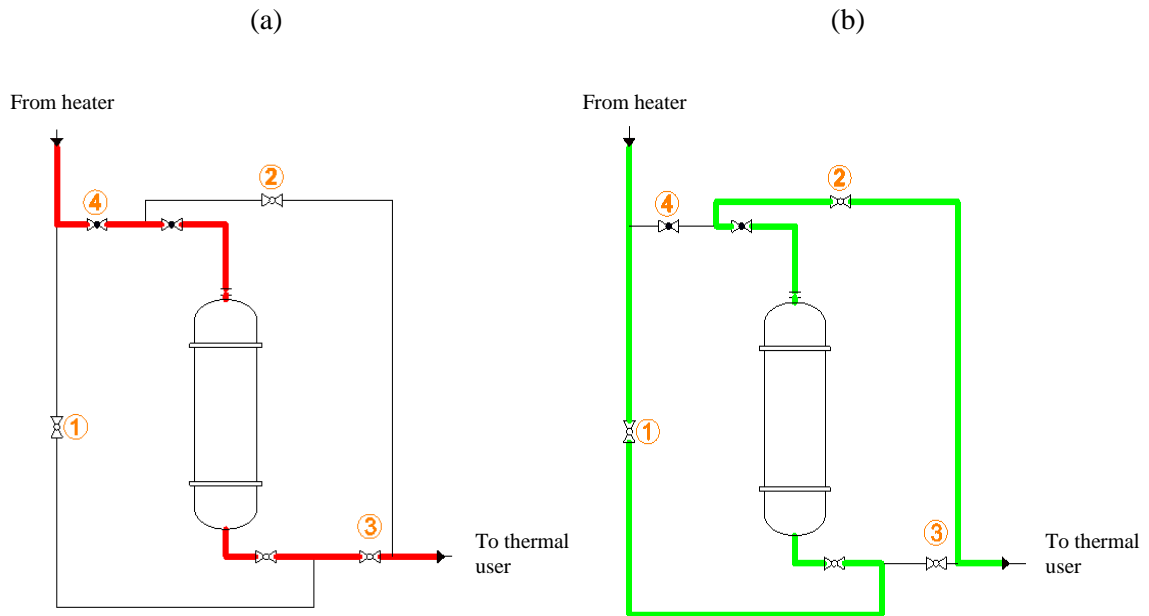
Fig. 5.3 - Two different modes concerning the HTF direction at TES inlet

This valves system is implemented to study the thermal performance of the storage device in function of the direction of HTF inlet. Furthermore it allows to analyze all the cases in which partial load conditions occur. In fact, it is not always possible to complete full charging and discharging processes for example, in cases of heater failure, when thermal energy is suddenly required or to fulfil peak-load during time. This system allows to avoid the formation of different solid-liquid interfaces which move in different directions inside the PCM. Not homogeneous phase transition process and different temperature profile are possible due to the presence of multiple melting/solidification fronts inside the PCM resulting loss thermal energy.

In the following paragraphs the main components of the test rig will be presented and analyzed.

5.2.1 Skid

A skid from "Pirobloc S.A." was selected for moving and heating the HTF. Figure 5.4 shows the skyd implemented in the laboratory.

Fig. 5.4 - Skid of the test rig

The skid is composed of the following main elements:

− Electric heater

The heater body is made of carbon steel with barrelled bottoms. The size of the heater body are 2645 mm (length) x 1450 mm (height) x 420 mm (depth), with a total capacity of 45 liters. The maximum operating temperature and pressure are 350 °C ad 15 bar respectively. The electrical resistance is made of AISI-316 stainless steel, and generates a maximum power equals to 41 kW. This power can be adjusted from 0 to 100%. This element has low density heating which means that the heat produced per surface area is very low (3.15 W/cm²) in order to avoid the oil cracking.

− Control panel

Processes control is carried out by the PLC model S7-1200 system from Siemens. Temperature and pressure measured with transducers placed in the boiler and in different section of the plant (fig. 5.1) are the input of the PLC. Two inverters allow the variation of rotational speed of the pump and of the air cooler fan. Furthermore a servo-actuated valve, controlled by the panel, allows to adjust the flow rate that circulates in the plant.

The control devices placed into the skid are:

- 1 Transmitter for differential pressure.
- 1 Transmitter for maximum pressure (minimum flow control).
- 2 Pressure gauges Ø 100, of 0-25 kg/cm², with glycerine bath and with its own expansion.
- Quadrants and closure taps.

- 3 Temperature probes type PT-100 (T1 for inlet temperature, T2 for outlet temperature, T3 as safety outlet temperature in figure 5.1 respectively).
- 3 Thermowells for the placement of the probes.

– Circulating pump

A nominal flow rate of 12 m³/h is set on the circulating pump model "ALLWEILER CTWH-32-160". The pump is designed to work with thermal oil with maximum temperature and pressure of 400 °C and 15 bar respectively. The pump has a nominal rotational speed equal to 2900 rpm and the presence of an inverter allows to vary the pump velocity. Fig. 5.5 reports the pump characteristic and system curves.
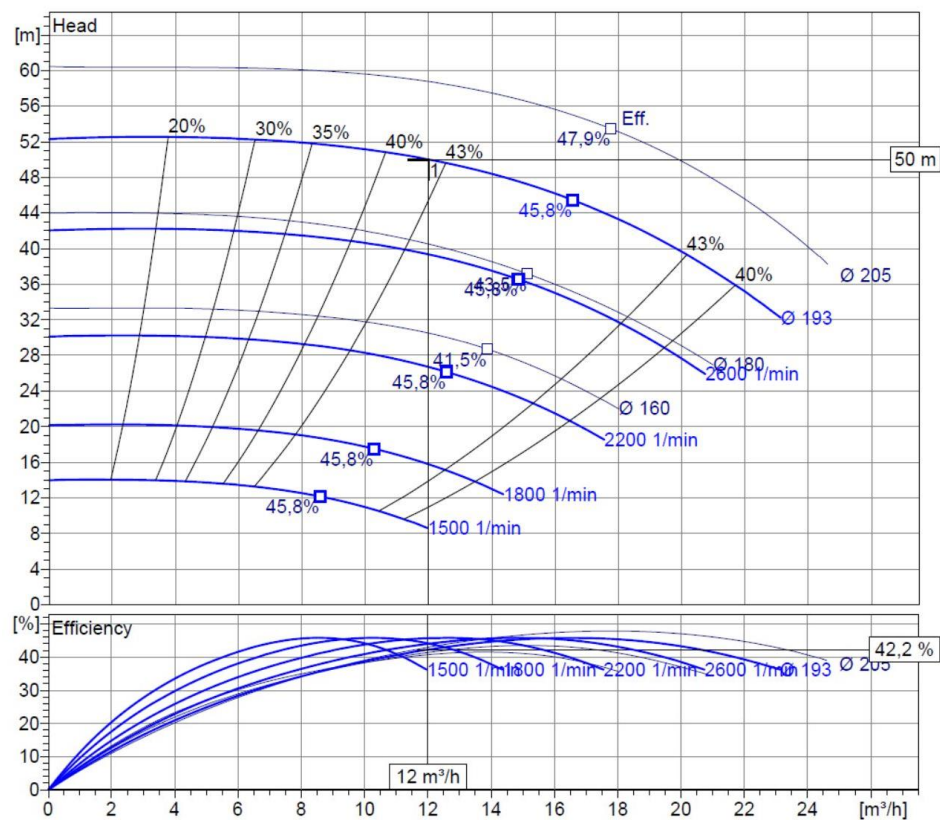
Fig. 5.5 - Pump characteristic and system curves

– Expansion tank

An expansion tank is a metal tank used to accommodate fluctuations in the volume the entire system. These fluctuations occur because HTF expands in volume during heating and reduces volume during cooling. This tank has a capacity of 400 liters and it is equipped with a magnetic level indicator. Nitrogen is used to pressurized the tank.

5.2.2 Air cooler

The air cooler producted by "Pirobloc S.A." (Fig. 5.6) allows to cool the HTF during the discharge phase in order to simulate thermal demand of an user.

Fig. 5.6 - Air cooler placed outside the laboratory

It consists of 36 helical finned tubes arranged in two rows of 18 tubes each, made of carbon steel ASTM A106 GrB (diameter of 25.4 mm, and length of 1000 mm). The air cooler is designed for a maximum temperature and pressure of 410 °C and 15 bar respectively.
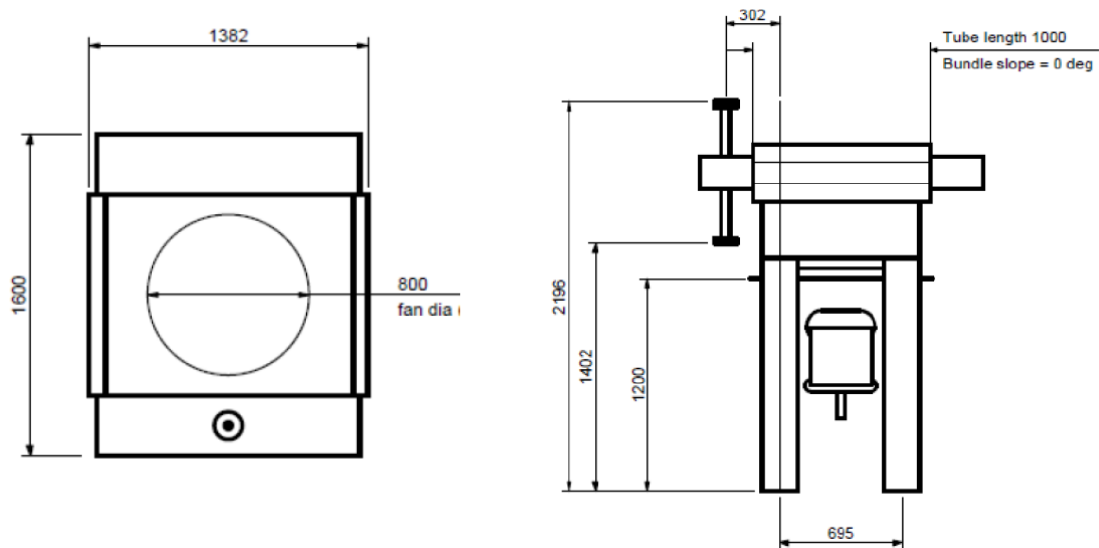
Fig. 5.7 - Scheme of air cooler

Figure 5.7 reports the scheme of the air cooler. The HTF flows into the tubes while air flowing outside is forced by a fan driven by an electric motor whose rotational speed can be varied by inverter. The HTF outlet temperature is measured by a temperature transmitter type PT-100 connected with the control system.

5.2.3 Air Separation Unit

Air trapped in the system can produce major problems such as reduced heat transfer, loss of system efficiency, pipe corrosion, pump damage and increased energy consumption. The air separator unit consists of a tube portion with a larger diameter than the other tubes forming the piping, which allow to aerate the HTF by flowing the gases directly to the expansion tank.

5.2.4 Thermal energy storage device

The design project of thermal energy storage device specifically applied to latent heat technologies was carried out. The geometry of the system is based on a configuration of shell and tube heat exchanger whose shell is filled with PCM while the HTF flows in the tube side.

Different TES geometrical configuration were proposed and studied during last years as reported by Sharma [6] and Farid [12]. Numerous researcher suggested the configuration of shell and tube heat exchanger as the most suitable for latent applications. Buddhi [65] designed and fabricated a PCM based shell and tube type heat exchanger without fins for low temperature industrial waste heat recovery. Trp et al. [66] analysed numerically and experimentally the transient phenomenon during both charging and discharging processes of the shell and tube latent energy storage system using paraffin as PCM. Adine and Qarnia [37] presented a numerical analysis of the thermal behaviour of a shell-and-tube PCM system comparing the utilization between one and two PCM. Cabeza et al. [9] conducted an experimental analysis of a shell and tube heat exchanger applied to

solar cooling. Morcos [67] studied an experimental investigation of a shell-and-tube heat exchanger concept for the use in a latent heat thermal energy storage system for solar heating applications. Hosseini et al. [68] investigated the thermal behaviour of phase change material (PCM) inside a shell and tube heat exchanger. Agyenim et al. [69][70] investigated melting and solidification on a paraffin in a shell and tube heat exchanger for various operating conditions and geometric parameters.

For the specific application the classical configuration of this type of heat exchanger was modified to adapt the shell side to the storage of the PCM material. Figure 5.9 shows the TES system layout which consists of a vessel with a tube bundle inside. This bundle is composed of 32 tubes distributed in square pitch as shown in figure 5.9b.

The tube bundle, was designed to operate at a maximum temperature and pressure of 370 °C and 16 bar respectively, while the shell was designed to operate at a maximum temperature and pressure of 370 °C and 1.49 bar respectively. Both tube bundle and shell are made of stainless steel.

The HTF flows in the tube side while PCM material is placed in the shell side. Two inclined nozzles DN-80 (identified with *J* in Figure 5.9a) were implemented in the upper part of the TES in order to facilitate the introduction of the PCM in the shell side during the filling procedure. A further nozzle DN-60 (identified with *K* in Figure 5.9a) coupled with gate valve was inserted in the TES bottom to realize emptying operation.

A particular floating head system was implemented in order to make shell side accessible for cleaning and inspection. This system allows to withstand the pressure in the shell side and avoids leakage of PCM during operation.

The geometrical characteristic and the design operative parameters of the TES are obtained using the design method presented in paragraph 5.2.5, and reported in Table 5.2.

Table 5.2 - Geometrical characteristics and design operating parameters of PCM-TES device

	Units	Value
Height	m	1.5
External Diameter	m	0.273
Number of tubes	-	32
External diameter tubes	m	0.01588 (5/8")
Pitch	m	0.0381
Maximum temperature	°C	370
Maximum pressure tube side	bar	16
Maximum pressure shell side	bar	1.49

Furthermore, considering D-Mannitol as PCM and Syltherm800 as HTF, a preliminary evaluation of thermal performance was carried out. The operating parameters of TES device are reported in Table 5.3.

Table 5.3 - Operating parameters of PCM-TES device using D-Mannitol

	Units	Value
HTF inlet temperature - Discharge	°C	100
HTF inlet temperature - Charge	°C	180
HTF flow	m³/h	0.5
PCM mass	kg	90
PCM melting temperature	°C	167
PCM latent heat	kJ/kg	234
Nominal latent heat storage capacity	kWh	5.7

(a)   (b)
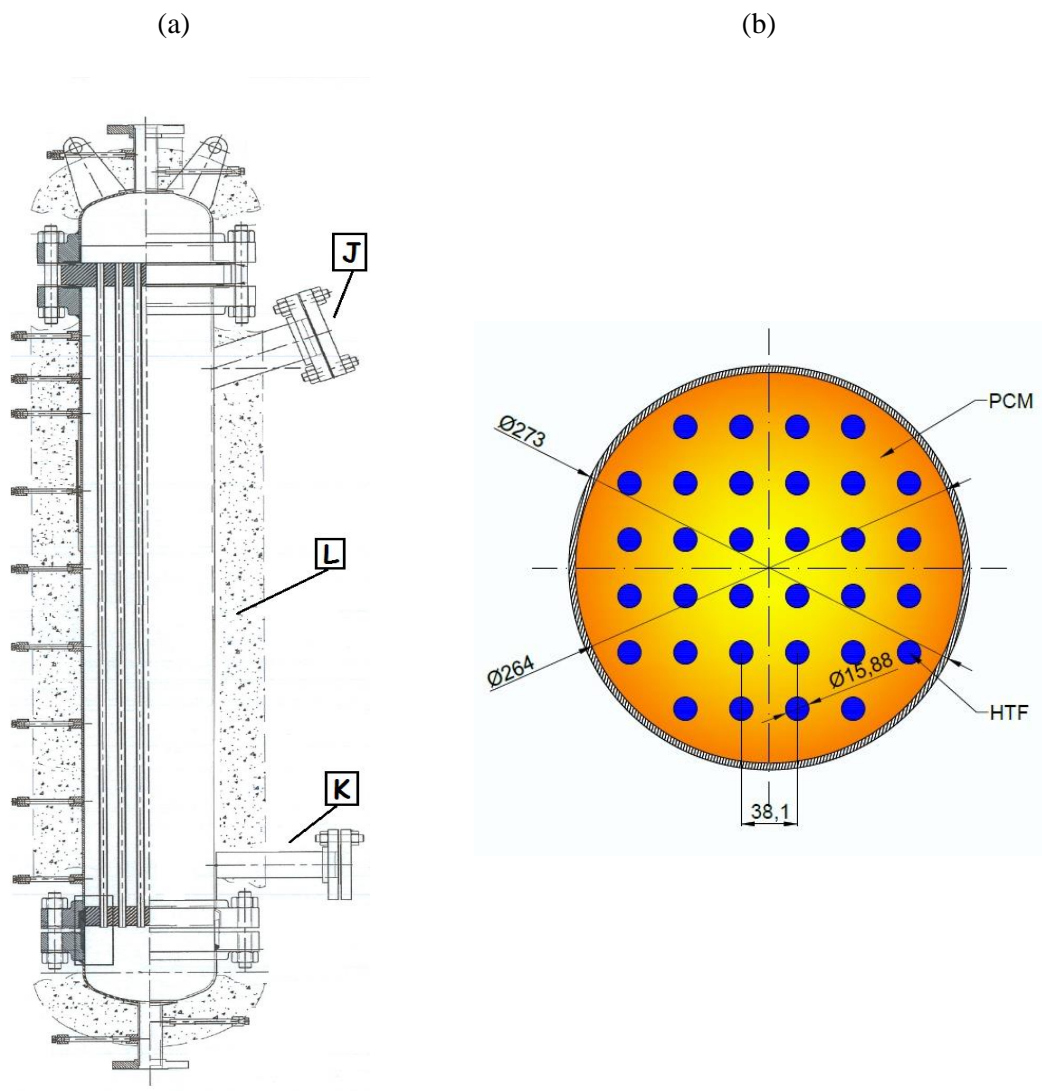
Fig. 5.9 - TES layout (a) and tube bundle scheme (b)

In order to minimize the heat losses, 100 mm of rock wool (identified with *L* in Figure 5.6a) were installed on both lateral walls and two ends.

Square pattern was selected to facilitate the insertion of the temperature measurement system inside the TES shell side. The temperature measurement system allows to determine the PCM temperature profiles in both radial and axial direction during operation. In the axial direction, eight thermocouples (type K) were inserted in order to cover the entire height of the TES, while thermocouple multipoint sensor systems (type K) were used in radial direction. These systems were placed in three different section (upper, middle and bottom part) measuring the temperature evolution from the center to the outer wall of the TES. Finally, two additional thermocouples were inserted to measure the temperature of the HTF at the TES inlet and outlet.

A numerical model based on the Logarithmic Mean Temperature Difference (LMTD) method [71] was developed in Matlab environment to determine both the heat transfer area of the storage device (sizing problem) and the TES performance (rating problem). Even if LMTD method is used for heat exchanger in which the heat transfer occurs between the two fluids, it can be also applied for PCM applications [16].

5.2.5 LMTD method

During phase transition, PCM material releases thermal energy through an isothermal transformation (for pure substance). Figure 5.10(a,b) reports the fluid temperature variation in heat exchanger when phase transition occurs during charge (a) and discharge (b) processes.

(a)   (b)
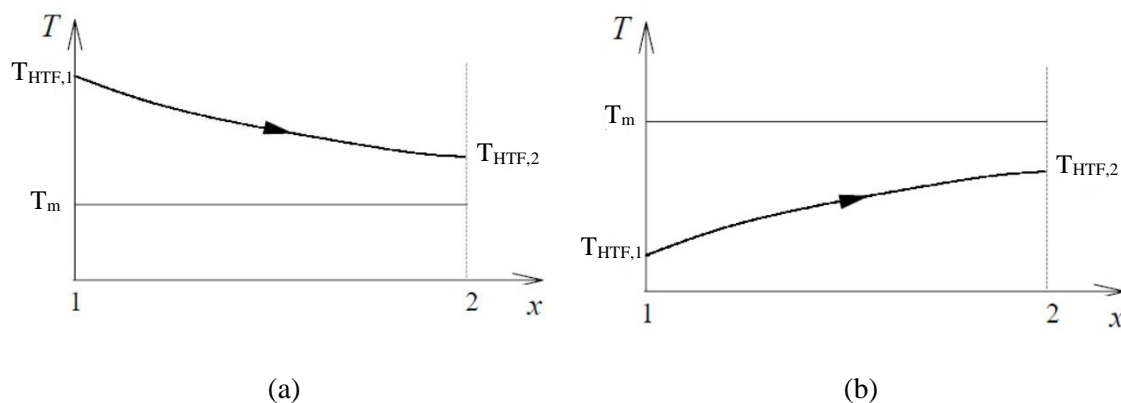
Fig. 5.10 - Fluid temperature variation in heat exchanger when occurs phase transition during charge (a) and discharge (b) processes.

In general, in heat exchanger applications, the inlet and outlet temperatures are commonly specified based on the fluid in the tubes. The temperature change that takes place across the heat exchanger from the entrance to the exit is not linear. A precise temperature change between two fluids across the heat exchanger is best represented by the log mean temperature difference:

$$\Delta T_{ml} = \frac{\Delta T_2 - \Delta T_1}{\ln\left(\frac{\Delta T_2}{\Delta T_1}\right)}$$

(5.1)

where:

$$\Delta T_1 = T_{h1} - T_{c1} \tag{5.2}$$

$$\Delta T_2 = T_{h2} - T_{c2} \tag{5.3}$$

The variables T_h and T_c represent the temperature of hot and cold fluids that flow in the heat exchanger, while the subscripts 1 and 2 refer to the inlet and the outlet conditions. If one of the two fluids is replaced by a PCM (Fig. 5.10a,b), the heat exchanger becomes a heat storage type. Indeed, the PCM has not a constant temperature along the heat exchanger and the temperature will also change with time. Nevertheless, a simplified first approach was used assuming a constant temperature equal to the phase change temperature along the heat exchanger and constant with time. Considering that the PCM is everywhere at the phase transition temperature means that all inlet and outlet temperatures of hot fluid can be replaced by the phase change temperature T_m. Thus, the Equation 5.1 becomes:

$$\Delta T_{ml} = \frac{\Delta T_2 - \Delta T_1}{\ln\left(\frac{\Delta T_2}{\Delta T_1}\right)} = \frac{\left(T_m - T_{HTF,2}\right) - \left(T_m - T_{HTF,1}\right)}{\ln\left(\frac{T_m - T_{HTF,2}}{T_m - T_{HTF,1}}\right)} \tag{5.4}$$

The rate of the heat transfer between the two fluids in general, and between PCM and fluid in particular, is related with the mean logarithmic temperature difference (Eq. 5.4) by the equation:

$$\dot{Q} = U \cdot A \cdot \Delta T_{ml} \tag{5.5}$$

where, $\dot{Q}$ is the heat transfer rate [W], U_d is the overall heat transfer coefficient [W/m^2·K] including heat transfer coefficients of the fluids and heat conduction through the heat exchanger material and A is the heat exchanging area [m^2].

The clean (a) and dirty (b) overall heat transfer coefficient can be calculated from Equation 5.6(a,b):

$$U_c = \frac{1}{\frac{1}{h_{HTF}} + R_w + \frac{1}{h_{PCM}} \cdot \frac{A_i}{A_o}} \tag{5.6a}$$

$$U_d = \frac{1}{U_c} + R_{f,o} + R_{f,i} \cdot \frac{d_0}{d_i} \tag{5.6b}$$

where h_{HTF} and h_{PCM} are the heat transfer coefficients [W/m²·K] of HTF and of PCM, R_w is the conduction coefficient through the wall [m²·K/W], $R_{f,i}$ and $R_{f,o}$ are the fouling factors for the inner and outer pipe respectively [m²·K/W], A_i and A_o are the inner and the outer surface area of the tube wall [m] while d_i and d_o are the diameter of inner and outer pipe respectively [m].

Convective heat transfer coefficients for HTF

The convective heat transfer coefficient between HTF (inside the tube) and tube walls is a function of the thermal conductivity of the fluid k_{HTF}, the internal diameter of the tubes d_i and the Nusselt number Nu as reported in Equation 5.7:

$$h_{HTF} = \frac{k_{HTF} \cdot Nu}{d_i} \tag{5.7}$$

A correlation for the Nusselt number for laminar flow was provided by Sieder and Tate:

$$Nu = 1.86 \cdot \left(\frac{Re \cdot Pr}{L/d_i} \right)^{1/3} \left(\frac{\mu_{oil}}{\mu_w} \right)^{0.14} \tag{5.8}$$

where L is the tubes length, Re and Pr are the Reynolds and Prandtl numbers respectively while μ_{oil} and μ_w are the dynamic viscosity of the HTF calculated at bulk fluid average temperature and at wall average temperature. It attempts to explicitly account for the fact that the viscosity of the fluid next to the wall is different from that in the bulk at any axial location. If the wall is hot, and we consider a liquid being heated in the pipe, the viscosity of the wall fluid will be smaller than that of the fluid in the bulk. This increases the velocity gradient at the wall and therefore the heat transfer rate compared to that obtained by assuming that the fluid is at a single temperature across the entire cross-section.

Reynolds and the Prandtl numbers are obtained respectively by the relations:

$$Re = \frac{\rho_{HTF} \cdot u_{HTF} \cdot d_i}{\nu_{HTF}} \tag{5.9}$$

$$Pr = \frac{C_{p,HTF} \cdot \mu_{HTF}}{k_{HTF}} \tag{5.10}$$

The parameters ρ_{HTF}, k_{HTF}, $C_{p,HTF}$, are density, thermal conductivity and specific heat of the HTF while u_{HTF} is the HTF velocity inside the tubes.

For a smooth surface and fully turbulent conditions (Re>10.000), the Dittus–Boelter equation is widely used:

$$Nu = 0.023 \cdot Re^{0.8} Pr^n \tag{5.11}$$

where, $n = 0.4$ for heating, and $n = 0.3$ for cooling.

Conductive heat transfer coefficient

The heat transferred from the tubes wall to the PCM, placed outside the tubes, happens by conduction. The heat transfer coefficient for the wall is given by the equation:

$$R_w = \frac{\delta_w}{k_w \dfrac{A_{lm}}{A_o}} \tag{5.12}$$

where:

- δ_w is tube thickness [m]
- k_w is tube the thermal conductivity [W/m·K]
- $A_{lm} = (A_o - A_i)/\ln(A_o/A_i)$ is the log mean area
- $A_i = 2\pi L r_i$ is the inner surface area of the tube wall [m]
- $A_o = 2\pi L r_o$ is the outer surface area of the tube wall [m]

Fouling factor

After a period of time, the heat transfer surfaces of a heat exchanger may become coated with deposits from the heat transfer fluids or corrosion. In either case, the additional resistance to heat transfer due to these materials decreases the performance of the heat exchanger and must be accounted for. This is done through the use of experimentally determined fouling factors. If the fouling resistance is not given, it can be adopted values specified in the TEMA (Tubular Exchanger Manufacturers Associations, www.tema.org) standards. Representative values of fouling factors are given in Table 5.3 for some common fluids.

Table 5.3 - Representative fouling factors in heat exchangers

Fluid	R_f (m² K)/W
Seawater and treated boiler feedwater (below 50°C)	0.0001
Seawater and treated boiler feedwater (above 50°C)	0.0002
River water (below 50°C)	0.0002–0.001
Fuel oil	0.0009
Refrigerating liquids	0.0002
Steam (non-oil bearing)	0.0001

Heat transfer coefficient for PCM

Determine the heat transfer coefficient in PCM side is more complicated. This coefficient is obtained through the equation (43) expressed as a function of the Nusselt number. However, during the phase change process, the heat transfer mode is not unique but three different regimes exist. The first regime appears at the beginning of the melting process where the heat transfer process is dominated only by conduction and is characterized by the relatively large magnitude of the Nusselt number that decreases as time elapses. The second regime occurs when melting process becomes more significant as time progresses thus, natural convection dominates the heat transfer process. Between these two regimes lies the transition regime where both conduction and convection are prime factors in the heat transfer process.

Many authors proposed experimental correlations to determine the Nusselt number for PCM during phase transition process. Jesumathy et al. [72] investigated the behaviour of paraffin wax in cylindrical tube and proposed a correlation in which the Nusselt number is function of Rayleigh number (obtained by the product between the Grashof and Prandtl numbers $Ra = Gr \cdot \mathrm{Pr}$), the thickness of the PCM material and the length of the storage device. Wang et al. [73] presented an experimental investigation of the melting process in the vicinity of a heated vertical wall in a flat-plate heat pipe and proposed a correlation to determine a time average Nusselt number as a function of Rayleigh number, Prandtl number and the location of the solid-liquid interface.

5.2.6 Design of the TES device

The design procedure of shell and tube heat exchanger [74] applied to latent heat thermal energy storage was developed in Matlab environmental using the LMDT method. The TES design was performed in discharge phase using an iterative technique in order to evaluate the best device configuration to supply a heat thermal load required by user.

At the beginning, the selected operating parameters necessary to design the TES system are:

-   HTF flow rate (selected in the pump operating range of the test rig)
-   HTF inlet temperature (selected in the heater operating range of the test rig)
-   HTF operating pressure (selected in the pump operating range of the test rig)
-   length of storage device

- allowable pressure drop
- heat thermal power required by the user.

The main steps of the iterative scheme are summarized as follows:

I.   Calculate the required thermophysical properties of HTF and PCM at operating conditions. As said before, the used HTF is the silicone oil Syltherm800, which required properties [58], i.e. viscosity, thermal conductivity, density, and specific heat are obtained in function of bulk temperature, while the selected PCM is the D-Mannitol which properties are reported in Table 4.3.

II.   Perform energy balance and find out the HTF outlet temperature using the Equations 5.13-5.14:

$$\dot{Q} = \int_{T_{HTF,1}}^{T_{HTF,2}} \dot{m} C_p dT = \dot{m} \overline{C_p} \left(T_{HTF,2} - T_{HTF,1} \right) \tag{5.13}$$

$$T_{HTF,2} = \frac{\dot{Q}}{\dot{m} \overline{C_p}} + T_{HTF,1} \tag{5.14}$$

Where $\dot{Q}$ is the thermal power required by the user [W], $\dot{m}$ is the HTF flow rate [kg/s], $\overline{C_p}$ is the specific heat [J/kg·K] evaluated in the temperature range between $T_{HTF,1}$ and $T_{HTF,2}$. These two temperatures represent the HTF inlet and outlet temperature [K].

III. Calculate the log mean temperature difference ΔT_{ml} given by Equation 5.4.

IV.   Assume a reasonable value of overall heat transfer coefficient U_o' for the first process iteration. The value of U_o' with respect to operating fluids, can be taken from Table 5.4:

Table 5.4 - Typical overall heat transfer coefficient for shell and tube heat exchangers

Shell and Tube Heat Exchangers	Hot Fluid	Cold Fluid	U [W/m²C]
Heat Exchangers	Water	Water	800 - 1500
	Organic solvents	Organic Solvents	100 - 300
	Light oils	Light oils	100 - 400
	Heavy oils	Heavy oils	50 - 300
	Reduced crude	Flashed crude	35 - 150
	Regenerated DEA	Foul DEA	450 - 650
	Gases (p = atm)	Gases (p = atm)	5 - 35
	Gases (p = 200 bar)	Gases (p = 200 bar)	100 - 300
Coolers	Organic solvents	Water	250 - 750
	Light oils	Water	350 - 700
	Heavy oils	Water	60 - 300
	Reduced crude	Water	75 - 200
	Gases (p = atm)	Water	5 - 35
	Gases (p = 200 bar)	Water	150 - 400
	Gases	Water	20 - 300
	Organic solvents	Brine	150 - 500
	Water	Brine	600 - 1200
	Gases	Brine	15 - 250

Then, evaluate the heat transfer area A' required using U'_d for the first iteration:

$$A' = \frac{\dot{Q}}{U'_d \cdot \Delta T_{ml}}$$
(5.15)

V.   Fixed the length L [m] and the outer diameter of the tubes d_o [m], evaluate the tubes number N'_t required to provide the heat transfer area A' through the Equation 5.16.

$$N'_t = \frac{A'}{\pi \cdot d_o \cdot L}$$
(5.16)

VI. Selecting the tube pitch and the number of passes from Table 5.11 [74], the internal shell diameter is obtained.

842   PROCESS HEAT TRANSFER

TABLE 9. TUBE-SHEET LAYOUTS (TUBE COUNTS).—(Continued)
Triangular Pitch

¾ in. OD tubes on 15/16-in. triangular pitch

Shell ID, in.	1-P	2-P	4-P	6-P	8-P
8	36	32	26	24	18
10	62	56	47	42	36
12	109	98	86	82	78
13¼	127	114	96	90	86
15¼	170	160	140	136	128
17¼	239	224	194	188	178
19¼	301	282	252	244	234
21¼	361	342	314	306	290
23¼	442	420	386	378	364
25	532	506	468	446	434
27	637	602	550	536	524
29	721	692	640	620	594
31	847	822	766	722	720
33	974	938	878	852	826
35	1102	1068	1004	988	958
37	1240	1200	1144	1104	1072
39	1377	1330	1258	1248	1212

¾ in. OD tubes on 1-in. triangular pitch

Shell ID, in.	1-P	2-P	4-P	6-P	8-P
8	37	30	24	24	
10	61	52	40	36	
12	92	82	76	74	70
13¼	109	106	86	82	74
15¼	151	138	122	118	110
17¼	203	196	178	172	166
19¼	262	250	226	216	210
21¼	316	302	278	272	260
23¼	384	376	352	342	328
25	470	452	422	394	382
27	559	534	488	474	464
29	630	604	556	538	508
31	745	728	678	666	640
33	856	830	774	760	732
35	970	938	882	864	848
37	1074	1044	1012	986	870
39	1206	1176	1128	1100	1078

1 in. OD tubes on 1¼-in. triangular pitch

Shell ID, in.	1-P	2-P	4-P	6-P	8-P
8	21	16	16	14	
10	32	32	26	24	
12	55	52	48	46	44
13¼	68	66	58	54	50
15¼	91	86	80	74	72
17¼	131	118	106	104	94
19¼	163	152	140	136	128
21¼	199	188	170	164	160
23¼	241	232	212	212	202
25	294	282	256	252	242
27	349	334	302	296	286
29	397	376	338	334	316
31	472	454	430	424	400
33	538	522	486	470	454
35	608	592	562	546	532
37	674	664	632	614	598
39	766	736	700	688	672

1¼ in. OD tubes on 19/16-in. triangular pitch

Shell ID, in.	1-P	2-P	4-P	6-P	8-P
10	20	18	14		
12	32	30	26	22	20
13¼	38	36	32	28	26
15¼	54	51	45	42	38
17¼	69	66	62	58	54
19¼	95	91	86	78	69
21¼	117	112	105	101	95
23¼	140	136	130	123	117
25	170	164	155	150	140
27	202	196	185	179	170
29	235	228	217	212	202
31	275	270	255	245	235
33	315	305	297	288	275
35	357	348	335	327	315
37	407	390	380	374	357
39	449	436	425	419	407

1½ in. OD tubes on 17/8-in. triangular pitch

Shell ID, in.	1-P	2-P	4-P	6-P	8-P
12	18	14	14	12	12
13¼	27	22	18	16	14
15¼	36	34	32	30	27
17¼	48	44	42	38	36
19¼	61	58	55	51	48
21¼	76	72	70	66	61
23¼	95	91	86	80	76
25	115	110	105	98	95
27	136	131	125	118	115
29	160	154	147	141	136
31	184	177	172	165	160
33	215	206	200	190	184
35	246	238	230	220	215
37	275	268	260	252	246
39	307	299	290	284	275

APPENDIX OF CALCULATION DATA   841

TABLE 9. TUBE-SHEET LAYOUTS (TUBE COUNTS)
Square Pitch

¾ in. OD tubes on 1-in. square pitch

Shell ID, in.	1-P	2-P	4-P	6-P	8-P
8	32	26	20	20	
10	52	52	40	36	
12	81	76	68	68	60
13¼	97	90	82	76	70
15¼	137	124	116	108	108
17¼	177	166	158	150	142
19¼	224	220	204	192	188
21¼	277	270	246	240	234
23¼	341	324	308	302	292
25	413	394	370	356	346
27	481	460	432	420	408
29	553	526	480	468	456
31	657	640	600	580	560
33	749	718	688	676	648
35	845	824	780	766	748
37	934	914	886	866	838
39	1049	1024	982	968	948

1 in. OD tubes on 1¼-in. square pitch

Shell ID, in.	1-P	2-P	4-P	6-P	8-P
8	21	16	14		
10	32	32	26	24	
12	48	45	40	38	36
13¼	61	56	52	48	44
15¼	81	76	68	68	64
17¼	112	112	96	90	82
19¼	138	132	128	122	116
21¼	177	166	158	152	148
23¼	213	208	192	184	184
25	260	252	238	226	222
27	300	288	278	268	260
29	341	326	300	294	286
31	406	398	380	368	358
33	465	460	432	420	414
35	522	518	488	484	472
37	596	574	562	544	532
39	665	644	624	612	600

1¼ in. OD tubes on 19/16-in. square pitch

Shell ID, in.	1-P	2-P	4-P	6-P	8-P
10	16	12	10		
12	30	24	22	16	16
13¼	32	30	30	22	22
15¼	44	40	37	35	31
17¼	56	53	51	48	44
19¼	78	73	71	64	56
21¼	96	90	86	82	78
23¼	127	112	106	102	96
25	140	135	127	123	115
27	166	160	151	146	140
29	193	188	178	174	166
31	226	220	209	202	193
33	258	252	244	238	226
35	293	287	275	268	258
37	334	322	311	304	293
39	370	362	348	342	336

1½ in. OD tubes on 17/8-in. square pitch

Shell ID, in.	1-P	2-P	4-P	6-P	8-P
12	16	16	12	12	
13¼	22	22	16	16	
15¼	29	29	25	24	22
17¼	39	39	34	32	29
19¼	50	48	45	43	39
21¼	62	60	57	54	50
23¼	78	74	70	66	62
25	94	90	86	84	78
27	112	108	102	98	94
29	131	127	120	116	112
31	151	146	141	138	131
33	176	170	164	160	151
35	202	196	188	182	176
37	224	220	217	210	202
39	252	246	237	230	224

Fig. 5.11 - Tube sheet layout [74]

VII. Determine the heat transfer coefficient for tube h_{HTF} side using Equations from 43 to 47. Determine the shell side heat transfer coefficient. As said before, PCM is located in the shell side and the heat transfer coefficient is obtained by experimental correlations. Finally evaluate the tube-wall resistance from Equation 4.12.

VIII. Select the fouling factors from Table 5.3.

IX. Calculate overall heat transfer coefficient U_d'' based on the outside tube area using Equation 5.6.

X. The iterative method involves the comparison between the obtained value U_d'' and the value assumed by the first iterative step U_d'. If the different between these two values is less than an imposed error ε, the storage device is correctly designed, if not it is necessary repeat the calculations starting from step IV.

XI. Calculate the tube-side pressure drop ΔP_{tube} which consist of the pressure drop caused by frictional losses evaluated trough the Equation (5.17) and the pressure drop caused by the presence of curves for heat exchangers with multi-pass (not in this case).

$$\Delta P_t = f_D \rho \frac{L}{d_h} \frac{v}{2} \tag{5.17}$$

where f_D is the friction factor, ρ is the HTF density [kg/m³], L is the pipe length [m], $d_h = 4A/Z$ is the mean hydraulic diameter [m], v is the flow velocity [m/s], A is the pipe cross section area available for flow [m²] and Z is the wetted perimeter [m]

XII.   Calculate shell side pressure drop ΔP_{shell}: during transition the PCM change its density and consequently its volume.

Furthermore, two important aspects must be taken into account. First aspect concerns that during the design calculation a volume % overdesign must be considered. Overdesign represents an extra volume provided beyond that required to compensate the volume variation of PCM. D-Mannitol has a volume change of about 10% during solid-liquid transition. Moreover, this extra-volume takes into account the presence of baffles which further reduce the available volume. The second aspect concerns that D-Mannitol reacts with oxygen from the atmosphere enclosed in the storage device causing the change of thermochemical properties of the material and affecting thermal and cycling stability [75]. Thus, in this specific application, nitrogen is selected to fill the atmosphere enclosed in the storage device.

It is obvious that this method should be used only for a preliminary analysis because it is based on several simplified assumptions. In fact, constant conditions on the PCM side are assumed thus, there is no time dependency in the solution. The simple solution is derived using the approximation that the one side of the heat exchanger contains PCM that is always at the phase change temperature. The LMTD relies only on temperatures, not accounting for the energy stored during a phase change process, since it occurs at almost constant temperature but with important enthalpy variations. Moreover the solid-liquid front moves during the process, consequently varying the value of overall heat transfer coefficient. Nevertheless, the solution gives important insight into the influence of the main design parameters.

At the time of writing the test rig is already build while the storage system is still under construction. Once implemented the TES device, accurate experimental tests will be carried out in order to validate the results of the adopted numerical models.

Chapter 6

Dynamic analysis of a pilot plant based on LHTES system for DSG applications at Plataforma Solar de Almeria

The work presented in the previous chapters is based on the developed of numerical models to perform and simulate latent heat thermal energy storage devices. Furthermore, the design and the implementation of an experimental facility as well as of a shell and tube PCM storage system in the laboratory of the Department of Mechanical, Chemical and Materials Engineering of the University of Cagliari were performed.

To better understand the issues related to the experimental facilities based on the LHTES systems, and to study more in-depth the applications of this technology to real cases, an experimental investigation was also carried out in collaboration with the research center "PSA-Plataforma Solar de Almeria" situated in the Tabernas Desert (Province of Almeria, Spain). The Plataforma Solar de Almería (PSA), a dependency of the Centro de Investigaciones Energéticas, Medioambientales y Tecnológicas (CIEMAT), is the largest concentrating solar technology research, development and test center in Europe.

This further work was aimed to the set-up of the test facility implemented in the PSA laboratories for evaluating PCM-TES systems, and perform modelling and simulation of a complete system. In addition, the study of the layout, the re-design and modification of the experimental test facility was realized. Finally, a simplified numerical model to simulate the dynamic behaviour of entire system during both charge and discharge processes was developed.

This study is part of the REELCOOP project (Renewable Electricity Cooperation, www.reelcoop.com) of the Seventh European Framework Programme, which involves the construction of a hybrid solar thermal power plant to produce electricity at the "École Nationale d'Ingénieurs de Tunis (ENIT)" in Tunisia, with the collaboration of companies from different European countries. The system is composed of parabolic solar collectors, a biomass boiler and a thermal energy storage system, while the power section is based on an ORC (Organic Rankine Cycle) plant. In particular, the CIEMAT had the task of developing the latent heat thermal storage system, based on the concept of shell and tube heat exchanger, using the steam produced in the solar collectors and the boiler, as thermo-vector fluid system.

6.1 Introduction

Direct Steam Generation (DSG) in linear Fresnel or parabolic trough collectors is a promising technology to produce heat and power from solar energy, avoiding the use of thermal oil and thus decreasing costs [76]. For DSG systems, but in general for all technologies affected by intermittent availability of energy source, energy storage systems play a fundamental role in conserving energy reducing the mismatch between energy supply and demand [2,3]. State of the art parabolic trough power plants use HTF (synthetic oil) and a sensible storage medium (molten salt). Thus, the energy during charging and discharging can be transferred by a standard heat exchanger. If water/steam is also used as the primary HTF, the situation becomes more complex. Indeed while for oil-based CSP plants a 2-tanks molten salt sensible heat storage system has become a wide-spread standard as reported in Table 6.1 [15], for the DSG solar plants various system solutions have been proposed, but all of them are still at the pilot plant level technology.

Table 6.1 - Operational solar thermal facilities with thermal energy storage systems.

Project	Type	Storage medium	Nominal temperature (°C)		Storage concept	Plant capacity	Storage capacity
			Cold	Hot			
SSPS-DCS test facility Almeria, Spain	Parabolic trough	Santotherm 55	225	295	1 tank thermocline	1.2 MWth	5 MWht
Nevada Solar One Nevada, USA	Parabolic trough	Dowtherm A	318	393	Oversized field piping	64 MWe	0.5 h
Holaniku at Keahole Point Hawaii, USA	Parabolic trough	Water	n.a.[a]	200	Indirect storage	2 MWth, 500 kWe	2 h
Planta Solar-10 Sevilla, Spain	Central receiver	Pressurized water	240	260	Steam accumulator	11 MWe	50 min/20 MWht
Planta Solar-20 Sevilla, Spain	Central receiver	Pressurized water	n.a.	250−300	Steam accumulator	20 MWe	50 min
La Florida Badajoz, Spain	Parabolic trough	Molten solar salt[b]	292	386	2-tank Indirect	50 MWe	7.5 h
Andasol-1 Granada, Spain	Parabolic trough	Molten solar salt	292	386	2-tank indirect	50 MWe	7.5 h/1010 MWht
Andasol-2 Granada, Spain	Parabolic trough	Molten solar salt	292	386	2-tank indirect	50 MWe	7.5 h/1010 MWht
Extresol-1 Badajoz, Spain	Parabolic trough	Molten solar salt	292	386	2-tank indirect	50 MWe	7.5 h/1010 MWht
Manchasol-1 Ciudad Real, Spain	Parabolic trough	Molten solar salt	292	386	2-tank indirect	50 MWe	7.5 h
Manchasol-2 Ciudad Real, Spain	Parabolic trough	Molten solar salt	292	386	2-tank indirect	50 MWe	7.5 h
La Dehesa Badajoz, Spain	Parabolic trough	Molten solar salt	292	386	2-tank indirect	50 MWe	7.5 h
Puerto Errado 1 Murcia, Spain	Linear Fresnel	Saturated steam	n.a.	270	Steam accumulator	1.4 MWe	n.a.
Archimede Sicily, Italy	Parabolic trough	Molten solar salt	290	550	2-tank direct	5 MWe	8 h/100 MWht
Torresol Gemasolar Seville, Spain	Central receiver	Molten solar salt	292	565	2-tank direct	17 MWe	15 h
Dahan Beijing, China	Central receiver	Saturated steam/oil	220	350	Combined steam accumulator/concrete	1 MWe	1 MWht

[a] n.a. = not available.
[b] Molten solar salt = 60% sodium nitrate/40% potassium nitrate.

Among the different proposed solutions, the TES based on configuration of shell and tube heat exchanger [77][78][79][80], the Multylayer systems [81][82][83][84] and the thermocline with encapsulated PCM [85] [86] are the most adopted. The configuration of shell and tube heat exchanger will be further discussed and analyzed in chapter 6.

6.2 Material and method

Figure 6.1 reports the layout of the hybrid solar thermal power plant designed for REELCOOP project. The red lines represent the steam and blue lines represent the condensate.
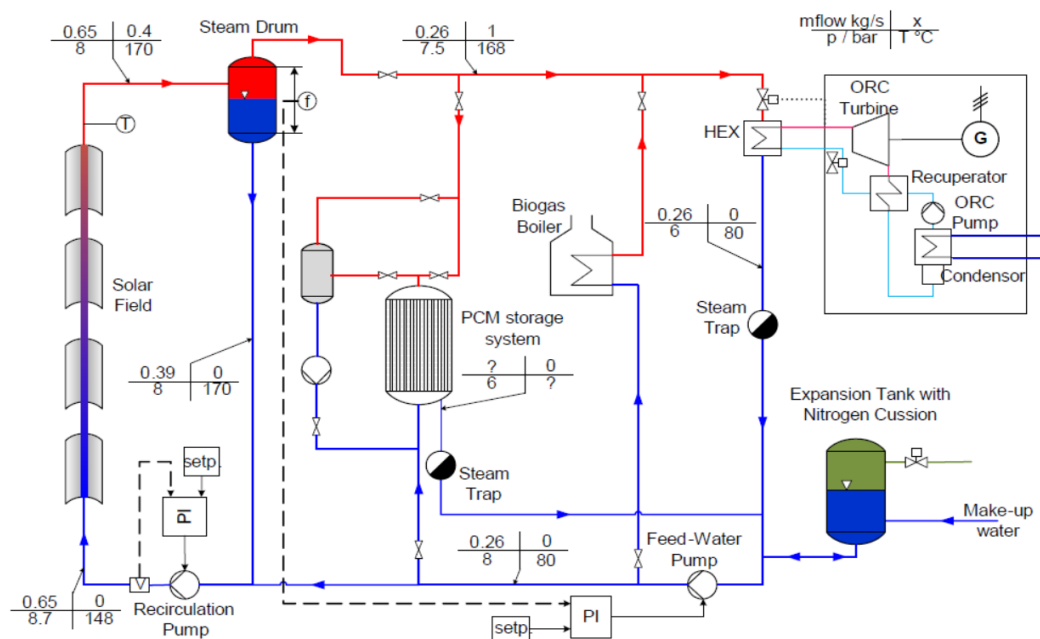

Fig. 6.1 - Layout of the hybrid solar thermal power plant (REELCOOP project)

As said before, CIEMAT as partner of this European project, had the task to investigate and design the storage system of the plant. Thus, the implementation of a test facility in the PSA laboratories was carried out in order to simulate the operating condition of the storage system evaluating its thermal performance.

The test facility for thermal energy storage system is composed of a pump that allows the circulation of the HTF during the charging and discharging processes, an electric boiler to produce steam (to simulate the solar field), a valve to control the pressure at the electric steam boiler outlet, the PCM-TES system based on the configuration of shell and tube heat exchanger and a mixer used as a condenser and considered as the thermal user.

Figures 6.2 and 6.3 show the test facility layout during charge and the discharge process respectively. During charge phase, the water is heated by the electric boiler until reaching the operating conditions of saturated steam (through pressure control), and then enters the TES transferring heat to the PCM material.
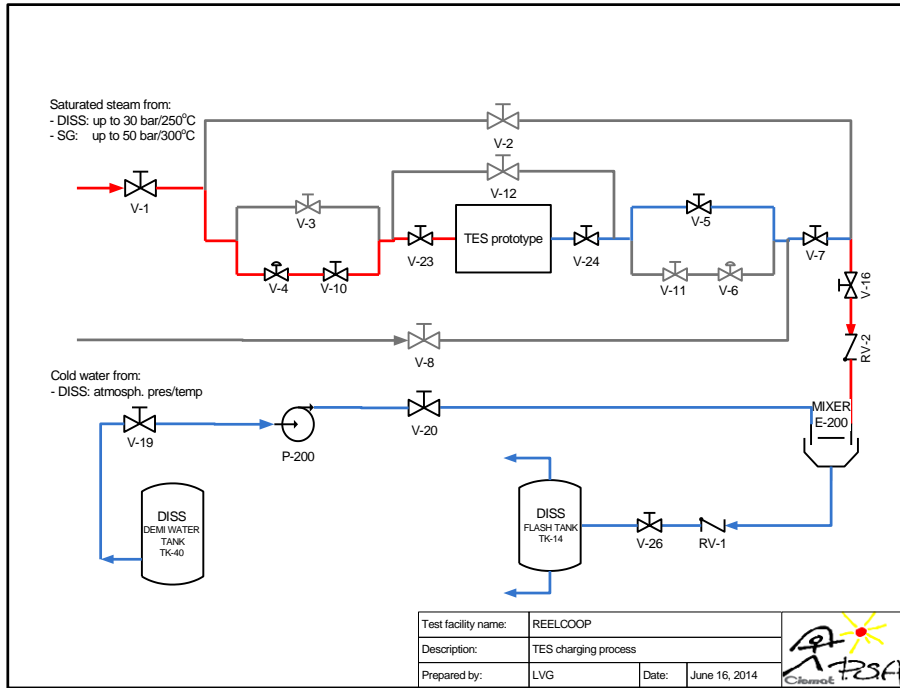
Fig. 6.2 - Test facility layout during charge phase

In the discharging phase, the water enters the TES as saturated liquid (at a given pressure) and receives heat from the PCM material, converting into steam. Subsequently, the water enters the mixer where it condenses. Red and blue lines represent the HTF in vapor and liquid conditions respectively that circulates within the pilot plant.
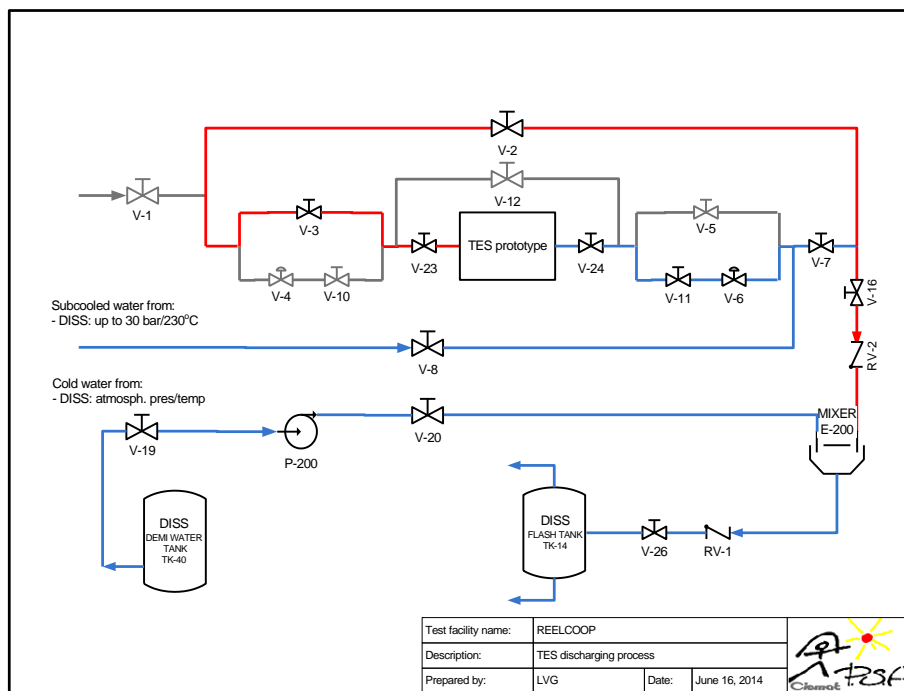

Fig. 6.3 - Test facility layout during discharge phase

During charge phase, steam temperature is equal to 180°C while in discharge phase, the steam at 160°C shall be provided to the ORC. For this temperature range D-Mannitol was selected as PCM. The properties of D-Mannitol have been already shown in Table 4.4.

As part of this project, a dynamic model of the test facility based on latent heat thermal energy storage system was developed using the commercial softwares Matlab and Simulink.

Circulating pump

The pump was used to circulate the HTF within the plant during both charge and discharge processes allowing to reach the operating pressure required.
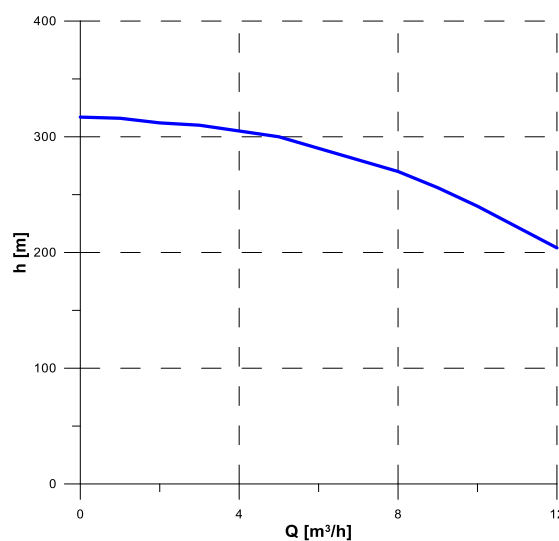
Fig. 6.4 - Pump characteristic curve head-flow

The pump characteristic curve head-flow is reported in Figure 6.4 and from which the Equation (6.1) is obtained:

$$h = -0.0157 \cdot Q^3 - 0.5639 \cdot Q^2 - 0.4148 \cdot Q + 316.66 \tag{6.1}$$

The model of the pump is presented in Figure 6.5. The pump extracts the water form a tank connected to water supply. Water flow rate, temperature and pressure are the model input, while the operating pressure is the output.
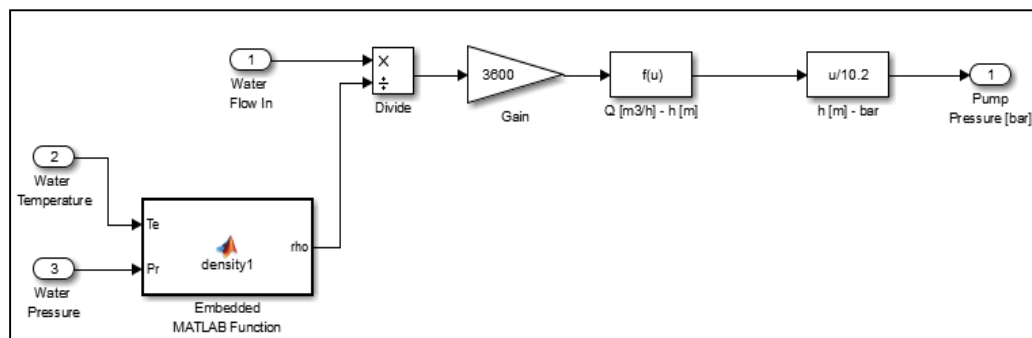
Fig. 6.5 - Circulating pump model

Electric steam boiler and regulating valve

Drum boiler dynamics was extensively studied over the years. Model-based control was the common method used by the most of research [87]. Wen Tan et al. [88] and [89] designed a linear controller of a boiler-turbine unit to operate in a carefully selected operating range of a highly non-linear model. Kim [90] investigated the analysis of the response of a thermal power plant using optimal control of drum level. Caifen Fu et al. [91] developed a robust PI controller to study the performance of a benchmark boiler system. Hèctor et al. [92] studied a sliding-mode control to achieve robust tracking of drum-type steam generating units. Bin Li et al. [93] modelled and simulated the start-up behaviour of controlled circulation and natural circulation boilers. Heimo [94] presented a comparison of four finite-volume-algorithms for the dynamic simulation of natural circulation steam generators. Adam et al. [95] developed a mathematical model for drum type boilers using a combination of non-linear equations, to describe the evaporation in the vertical tubes and the phase separation in the steam drum. Zhang et al. [96] studied two phase flow inside the risers, while Emara-Shabaik et al. [97] introduce a model to predict riser's temperature. One of the most complicated task is modelling water level because of the presence of steam below the liquid level in the drum causes the shrink-and-swell phenomena which makes level control difficult. Although the level control is very important for safe operation of boilers, none of the available literature presents a complete model for the system including the drum level. Kim H. and Choi S. [98] and Åström, K.J. and Bell R.D. [99] presented models to describe the volume of steam under the water level which can be used indirectly to evaluate the level.

A schematic picture of a boiler system is presented in Fig. 6.6. The heat, Q, supplied to the risers causes boiling. Feedwater, $\dot{m}_f$, is supplied from the pump to the drum while saturated steam, $\dot{m}_s$, is taken from the drum and sent to the TES system. Drum-type boilers use the principle of natural water circulation, where the density differences causes circulation of water in the down comer riser loop. Addition of heat causes the creation of steam bubbles in the riser tubes which are naturally separated from the saturated water in the drum. The upper part contains saturated steam while the lower part contains a steam/water mixture.
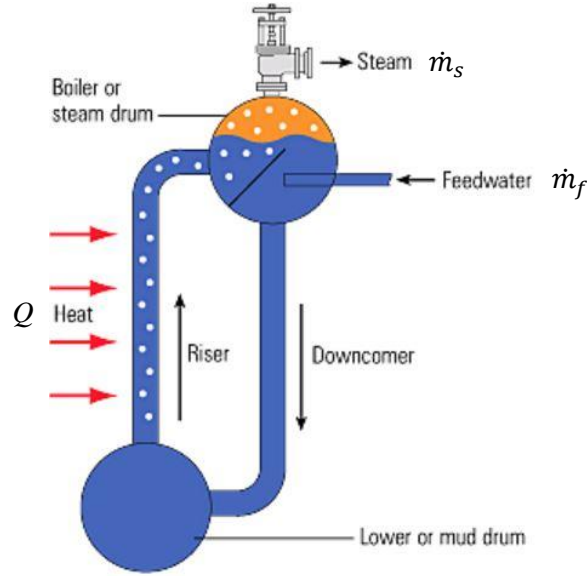
Fig. 6.6 - Schematic picture of a boiler system [99]

The system can be described by a simplified model only using global mass and energy balances [99]. The boiler achieves a very efficient heat transfer due to boiling and condensation. All parts of the system which are in contact with the saturated liquid-vapor mixture will be in thermal equilibrium. Energy stored in steam and water is released or absorbed very rapidly when the pressure changes ensuring that different parts of the boiler change their temperature in the same way. For this reason the dynamics can be captured by models of low order.

The global mass balance is given by Equation 6.2:

$$\frac{d}{dt}(\rho_s V_s + \rho_w V_w) = \dot{m}_f - \dot{m}_s \tag{6.2}$$

while the global energy is given by Equation 6.3:

$$\frac{d}{dt}\left(\rho_s h_s V_s + \rho_w h_w V_w - p V_t + m_{t,m} C_{p,m} T_m\right) = Q + \dot{m}_f h_f - \dot{m}_s h_s \tag{6.3}$$

In the reported equations the subscripts s, w, f, m refer to steam, water, feedwater and metal respectively, while $\dot{m}$ represent the mass flow rate, ρ specific density, V_t total volume , h specific enthalpy, T temperature, p pressure, $C_{p,m}$ specific heat and m_t total mass.

The total volume of the drum, downcomer, and risers, V_t is given by Equation 6.4:

$$V_t = * (V_s + V_w) \tag{6.4}$$

where V_s and V_w represent the total steam and water volumes, respectively. Equations (6.2), (6.3) and (6.4) are combined with saturated steam tables in order to obtain the boiler model that, mathematically, represents a differential algebraic system.

Pressure and total volume of water inside the boiler are the state variables from which are derived the following state equations, used to built the model developed in Simulink environment as reported in Figure 6.7. Using saturated steam tables, the variables ρ_s, ρ_w, h_s, and h_w are expressed as functions of steam pressure.

$$e_{11}\frac{dW_w}{dt} + e_{12}\frac{dp}{dt} = \dot{m}_f - \dot{m}_s \tag{6.5}$$

$$e_{21}\frac{dW_w}{dt} + e_{22}\frac{dp}{dt} = Q + \dot{m}_f h_f - \dot{m}_s h_s \tag{6.6}$$

where:

$$e_{11} = \rho_w - \rho_s \tag{6.7}$$

$$e_{12} = V_w\frac{\partial \rho_w}{\partial p} + V_s\frac{\partial \rho_s}{\partial p} \tag{6.8}$$

$$e_{21} = \rho_w h_w - \rho_s h_s \tag{6.9}$$

$$e_{22} = V_w\left(h_w\frac{\partial \rho_w}{\partial p} + \rho_w\frac{\partial h_w}{\partial p}\right) + V_s\left(h_s\frac{\partial \rho_s}{\partial p} + \rho_s\frac{\partial h_s}{\partial p}\right) - V_t + m_t C_p\frac{\partial t_s}{\partial p} \tag{6.10}$$

This model (Eqs. 6.5-6.10) describes the response of drum pressure to changes in input power, feedwater flow rate and steam flow rate.

Two PI controllers are used in the system using Cohen-Coon method. Proportional-integral-derivative (PID) controllers are the main types of feedback control and are widely used in industry due to their simplicity and easy to tuning. A PID controller calculates an error value as the difference between a measured process variable and a desired set-point. The output of PID controller is a linear combination of the input, the derivative of the input and the integral of the input.

The Cohen-Coon tuning method requires the response of an open-loop system to an input step change. The response generates a process reaction curve, which can adequately be represented by a first order system with dead time. From the generated curve, the static gain (K_c), the time constant (τ_I) and the dead time (τ_D) can all be estimated and used in the rules summarized in Table 6.2 to find the controller parameters.

Table 6.2- Cohen-Coon Formulas

Controller Type	Controller Gain K_c	Reset Time τ_I	Derivative Time τ_D
P	$K_c = \left(\frac{1}{K_p}\right)\left(\frac{\tau_p}{t_d}\right)\left(1 + \frac{t_d}{3\tau_p}\right)$		

$$\text{PI} \qquad K_c = \left(\frac{1}{K_p}\right)\left(\frac{\tau_p}{t_d}\right)\left(\frac{9}{10} + \frac{t_d}{12\tau_p}\right) \quad \tau_I = t_d \left(\frac{30 + \frac{3t_d}{\tau_p}}{9 + \frac{20t_d}{\tau_p}}\right)$$

$$\text{PID} \qquad K_c = \left(\frac{1}{K_p}\right)\left(\frac{\tau_p}{t_d}\right)\left(\frac{4}{3} + \frac{t_d}{4\tau_p}\right) \quad \tau_I = t_d \left(\frac{32 + \frac{6t_d}{\tau_p}}{13 + \frac{8t_d}{\tau_p}}\right) \quad \tau_D = t_d \frac{4}{11 + \frac{2t_d}{\tau_p}}$$

The controller attempts to minimize the error by adjusting the process through the use of a manipulated variable. In this case, the first PID controls the outside pressure by manipulating boiler power. The second PID controls the steam flow rate by manipulated flow coefficient of a valve situated at the boiler output.

The valve allows adjustment of the inlet pressure to the electric boiler. It is represented by the Equation 6.11:

$$\dot{m} = K_v \cdot \sqrt{\Delta P_v} \tag{6.11}$$

The K_v coefficient represent the opening degree of the valve and it can assume values between 0 (fully closed valve) and 1 (fully opened valve).
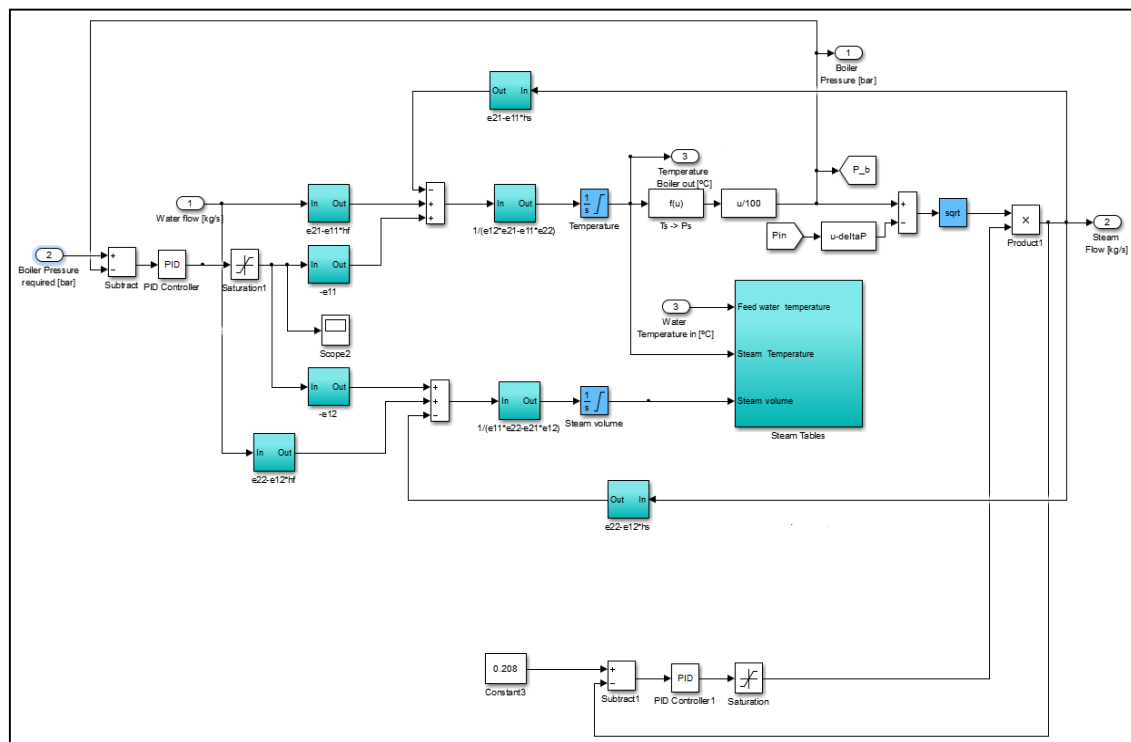

Fig. 6.7 - Model of the boiler implemented in Simulink

Mixer

A mixer (Fig. 6.8) is used to calculate the steam quality of the flow leaving the boiler. This flow is mixed with a saturated water flow that enters in the mixer with a certain temperature.
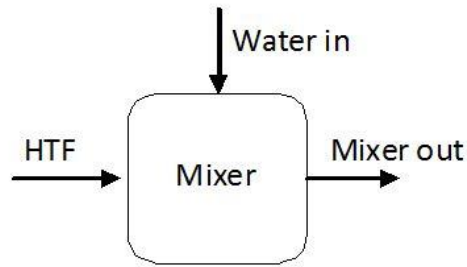
Fig. 6.8 - Schematic picture of the mixer

The global mass and energy balances are given by equation 6.12 and 6.13:

$$\dot{m}_{htf} + \dot{m}_{w,in} = \dot{m}_{mix,out} \tag{6.12}$$

$$\dot{m}_{HTF}(t)\big[h_{HTF,s}x(t) + h_{HTF,w}\big(1 - x(t)\big)\big] + \dot{m}_{w,in}(t)h_{w,in} = \dot{m}_{mix,out}(t)h_{mix,out} \tag{6.13}$$

where $h_{HTF,s}$ and $h_{HTF,w}$ are the specific enthalpies of the HTW in vapor or liquid condition respectively, functions of the temperature and pressure at boiler outlet. Figure 6.9 reports the mixer model developed in Simulink environment. The parameter $h_{w,in}$ is the specific enthalpy of the water at the mixer inlet, while $h_{mix,out}$ is the specific enthalpy of the mixture flow at the mixer outlet. The temperature $T_{w,in}$ of the water that entering into the mixer is evaluated in order to achieve the saturated liquid condition of the mixture flow at the mixer outlet.

Fig. 6.9 - Mixer model implemented in Simulink

6.3 Conclusions

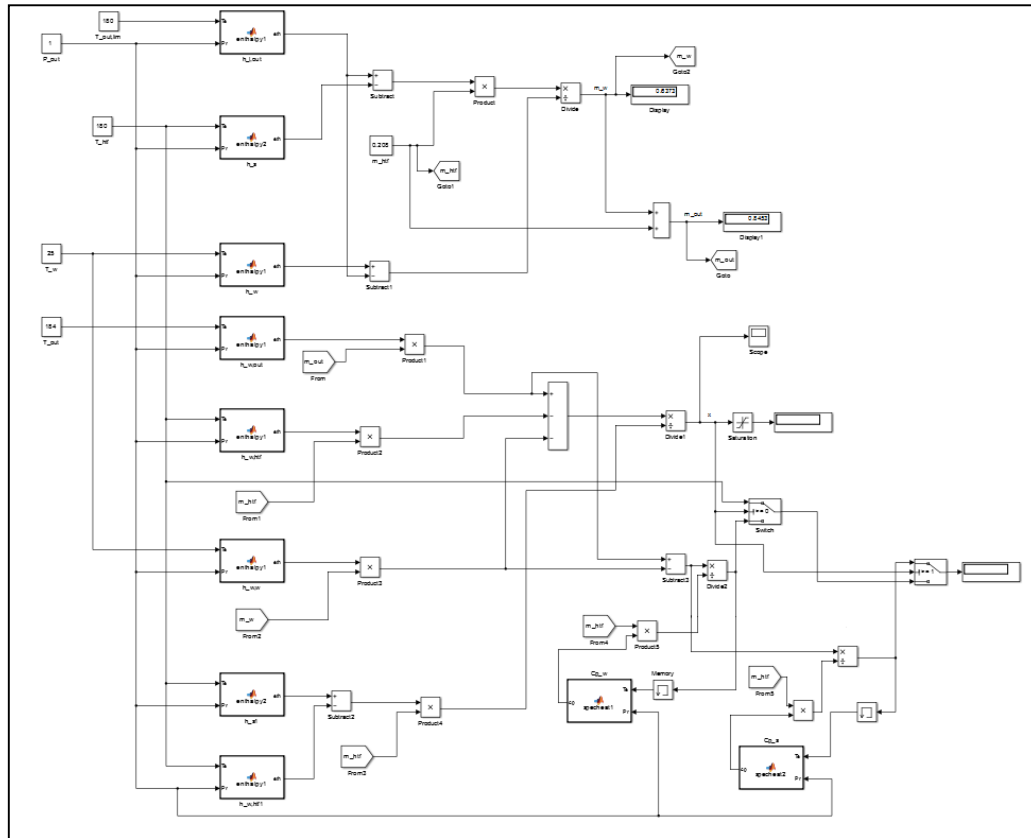In chapter 6 the performance analysis of a test facility based on latent heat thermal energy storage system was presented. This study was carried out with the collaboration of the research center of the "PSA-Plataforma Solar de Almeria" in the framework of the European project REELCCOP. A simplified numerical model was developed using the commercial softwares Matlab and Simulink to simulate the complete system behaviour (steam generator, a TES system and a cooling system) during the charge and discharge process of a PCM-TES system. At the time of writing the present PhD thesis, the plant is still under development.

Program changes and updates of research activity led by project management needs determined by partnerships between different European subjects, have delayed the implementation and realization phases of the project. Nevertheless acquired skill and technique have led contributions on research and experimental activities in the laboratories of the University of Cagliari. In fact, experimental data will assist in the validation of the model that could be used for future analysis on the effects of design parameters on the performance of the system. The model will be adapted to allow the simulation of the test rig designed and implemented in the laboratory for TES technologies of the DIMCM-University Cagliari presented in Chapter 5.

Chapter 7

Conclusions and future research

Energy storage plays an important roles in conserving available energy and improving its utilization, since many energy sources are intermittent in nature. Among the different methods used to store thermal energy, latent heat storage systems, which involve storing and recovery heat through the solid-liquid transition of phase change materials (PCM), is one of the most attractive option. These systems have various advantages with respect the others: the latent heat of most materials is much higher than their sensible heat, thus requiring a smaller mass of storage medium to storing/recovering a given amount of thermal energy with a consequent reduction of costs; the phase change process occurs at a nearly constant temperature, which is a fundamental aspect for efficient operation of most thermal systems.

In this framework, the investigation of thermal energy storage systems based on latent heat concept for renewable energy and other non programmable energy sources, industrial processes and heat and power generation for intermediate temperature applications (150-250 °C) was carried out. Main objective of this work is framed in the analysis of the performance of PCM-TES devices with respect to energy stored/released, time and efficiency during repeated cycles of charge/discharge, the analysis on different materials, geometries and heat transfer enhancement techniques in order to optimize the entire process. This work is based on two parts: the first part concerns the development of numerical models for simulating the transient behaviour of the PCM-TES, to predict the energy balance in space and time and the TES overall performances and their application to several test cases. The second part concerns the design and the implementation of a test rig specifically built for experimental investigation of heat storage devices.

These models were developed using 2D and 3D numerical simulation codes specifically implemented in the COMSOL Multiphysics environment. Two different approaches were analyzed to perform the behavior of PCM during phase transition. The first approach considers heat transfer only by conduction in both solid and liquid PCM phases. The second approach considers heat transfer by conduction and natural convection in liquid PCM domain. To model the phase transition, the apparent heat capacity formulation was used in both approaches. In this method, the latent heat was implemented by increasing the heat capacity of the material, while the phase change process was modelled by assuming that the transition takes place in a narrow range of temperature rather than at a fixed temperature. The two approaches were separately evaluated for two different cases and then were validated by comparing the numerical results with experimental data. For each model temperature behavior, phase change evolution and melting fraction were evaluated and analyzed for both charge and discharge processes.

The numerical codes, adopted to different PCM materials and TES geometries prove to be suitable for the simulation of the latent heat thermal energy storage systems. Furthermore, the numerical results demonstrate a good agreement with the experimental result for both approaches, also showing that the second approach was more accurate. Main differences between them concern the shape and the motion of solid-liquid interface were evaluated during transition

process. These two aspects depend on the heat transfer process considered. In fact, in melting process the heat transfer is dominated by convection, while in solidification process the heat transfer is dominated by conduction. Considering first approach, the solid-liquid interface moves uniformly around an heat source surface, while in the second approach, natural convection and buoyancy force cause a change of the shape of the melting/solidification front.

First approach was used to simulate a PCM-TES device based on the configuration of a shell and tube heat exchanger using Hydroquinone as PCM material. The results obtained showed that the PCM nearest to the shell was the last that undergoes the transition in both charge and discharge phases. With the first approach, the convection and the buoyancy force in liquid PCM domain were not considered, so the solid-liquid interface moves around the tubes uniformly.

Second approach was used to perform a comparison between three different storage devices, a double tube heat exchanger (Case 1), a triplex heat exchanger (Case 2) and a triplex with finned surfaces (Case 3), using D-Mannitol as PCM. These systems were used to determine which configurations are capable of enhancing thermal response between heat source and a PCM. As expected, the Case 2 and Case 3 were the solutions that allowed the faster response of the TES device during the charge and discharge processes. The insertion of fins allowed, in particular, not only an increase in the heat exchange surface of the inner HTF tube, but also the creation of cells in the PCM volume that determined faster melting/solidification of the PCM. Furthermore, it was found that the different configurations of this three systems considered have a strong impact on the shape of melting-solidification front as well as natural convection and buoyancy forces. In Case 1 the solid-liquid interface moves parallel and radially from the centre to the wall of the TES but it slopes gradually from the top. In Case 2 the interface assumed a monotonic shape, while in Case 3 various cells with liquid PCM formed during the process.

Furthermore, the effect of the number of fins on the melting rate was investigated comparing five different cases (0, 2, 4, 6, 8 fins). A big influence of the fins number on reducing the melting time was found. Considering the 85% of total melting, a reduction of 18.6% of melting time was estimated for the case with 8 fins with respect to the case without fins. The relative percentage difference of melting time $\Delta MT\%$ presents a maximum value of -7.2% for TES with four fins, while for higher number of fins this parameter decreases. Whereby, on the one hand the fins increased heat transfer rate by increasing the total surface area available for heat transfer by conduction, on the other high number of fins reduces the formation of convective cells decreasing the amount of heat transfer by convection.

Finally, the validation of these two methods was carried out using a storage system based on the configuration of a double tube with finned surfaces and paraffin as PCM. In order to evaluate which one of the two proposed approaches show more accuracy during charge and discharge processes, a comparison with the results obtained with two experimental tests, with different HTF flow rate values, was carried out. These tests were performed in the laboratories of the research center GREA Innovació Concurrent (University of Lleida, Spain). Overall, a good agreement with the experimental temperature profiles during charge and discharge phase was obtained. However, it was found that heat transfer mode influences the interface shape and motion during both the melting and solidification processes. In fact, natural convection in melt region drives and improves the heat transfer rate increasing the velocity of the solid-liquid interface. At the end of charge phase, the temperature profile obtained with the second approach shows a good agreement with respect to the experimental results, while the first approach is less accurate. Instead, the numerical prediction of both approaches appears very similar to the experimental results during discharge process. Same considerations for melting fraction. Comparing the melting fraction

values, a difference of 0.14 and 0.2 between second and first approach were obtained for experiment 1 and 2 respectively at the end of charge process, while a difference of 0.04 was obtained for both experiments at the end of discharge phase. Considering the solid-liquid interface, it can be noticed that it moves parallel and radially from the centre to the wall of the TES in the first approach, while in the second approach, due to natural convection and buoyancy force, this boundary slopes gradually from the top, inward during melting and outward during solidification.

Finally, the first approach was simple and required relatively low computational resources but it was proven less accurate. A good agreement was obtained using the second approach that was more closer to the experimental results thus, natural convection plays a significant role in phase change process and it must be taken into account. The effects of natural convection on the shape and the motion of solid-liquid interface can not be neglected. However, it must be considered that the addition of natural convection implies a major requirement of computational resources.

The second part, as said before, concerns the design and the implementation of a test rig specifically built for experimental investigation of heat storage devices. The test rig, now implemented in the laboratory for TES technologies of the Department of Mechanical, Chemical and Materials Engineering (DIMCM) of the University of Cagliari, was conceived and designed not only to validate all the developed numerical models, but also to carry out a considerable research activity in the field of thermal energy storage based on modeling, control and testing of innovative TES systems for industrial applications. The experimental facility is composed of an electrical heater, a pump, an aircooler and a thermal energy storage system accurately selected for the specific application. It allows to operate at a maximum temperature and pressure conditions up to 350 °C and 15 bar respectively. A PCM-TES prototype was specially designed and build as latent heat thermal energy storage device based on the configuration of shell and tube heat exchanger. The design was carried out by means of iterative technique using a LMTD method. At the time of writing the test rig is already build while the storage system is still under construction.

In future works, a new 3D numerical model based on the configuration of the PCM-TES build for the test rig using second approach (i.e. natural convection and buoyancy force) will be developed. Moreover, the analysis and simulation with different geometries and configuration of the storage systems and the study of others PCM materials will be carried out. Further analysis will be based on the optimization with respect to the number, the pitch, the thickness, the length and the shape of the fins, as well as the effects of different flow rate and fins number on the TES thermal performance will be studied. Finally, an accurate both numerical and experimental investigation on partial load condition will be carried out in order to study the behaviour and the thermal performance of PCM-TES under this fundamental aspect regarding most of industrial applications.

Concerning the experimental facility, the implementation of the PCM-TES device will be carried out in the short term. Then, the implementation of data acquisition system will be realized in order to complete the test rig and start the experimental tests.

References

[1]   INTERGOVERNMENTAL PANEL ON CLIMATE CHANGE 2014 *CLIMATE CHANGE 2014 - Impacts, Adaptation, and Vulnerability*

[2]   Gil A, Medrano M, Martorell I, Lázaro A, Dolado P, Zalba B and Cabeza L F 2010 State of the art on high temperature thermal energy storage for power generation. Part 1-Concepts, materials and modellization *Renew. Sustain. Energy Rev.* **14** 31–55

[3]   Medrano M, Gil A, Martorell I, Potau X and Cabeza L F 2010 State of the art on high-temperature thermal energy storage for power generation. Part 2—Case studies *Renew. Sustain. Energy Rev.* **14** 56–72

[4]   Luo X, Wang J, Dooner M and Clarke J 2015 Overview of current development in electrical energy storage technologies and the application potential in power system operation q *Appl. Energy* **137** 511–36

[5]   Hameer S and Niekerk J L Van 2015 A review of large-scale electrical energy storage 1179–95

[6]   Sharma A, Tyagi V V, Chen C R and Buddhi D 2009 Review on thermal energy storage with phase change materials and applications **13** 318–45

[7]   Chen H, Ngoc T, Yang W, Tan C and Li Y 2009 Progress in electrical energy storage system : A critical review *Prog. Nat. Sci.* **19** 291–312

[8]   Cot-gores J, Castell A and Cabeza L F 2012 Thermochemical energy storage and conversion : A-state-of-the-art review of the experimental research under practical conditions *Renew. Sustain. Energy Rev.* **16** 5207–24

[9]   Gil A, Oró E, Miró L, Peiró G, Ruiz Á, Salmerón J M and Cabeza L F 2013 Experimental analysis of hydroquinone used as phase change material (PCM) to be applied in solar cooling refrigeration *Int. J. Refrig.* **9** 1–9

[10]   Benz N, Hennecke K, Zentrum D, Dlr V, Höhe L and Germany K THE POTENTIAL OF SOLAR HEAT IN INDUSTRIAL PROCESSES. A STATE OF THE ART REVIEW FOR SPAIN AND PORTUGAL

[11]   Vannoni C, Battisti R and Drigo S 2008 *Potential for Solar Heat in Industrial Processes*

[12]   Farid M M, Khudhair A M, Ali S and Razack K 2004 A review on phase change energy storage : materials and applications **45** 1597–615

[13]   Kalaiselvam S and Parameshwaran R 214AD *Thermal Energy Storage Technologies for Sustainability: Systems Design, Assessment and Applications* ed Elsevier

[14]   Cabeza L F 2014 *Advances in Thermal Energy Storage Systems_ Methods and Applications* (Woodhead Publishing Series in Energy)

[15]   Kuravi S, Trahan J, Goswami D Y, Rahman M M and Stefanakos E K 2013 Thermal energy storage technologies and systems for concentrating solar power plants *Prog. Energy Combust. Sci.* **39** 285–319

[16]   Mehling H and Cabeza L F 2008 *Heat and cold storage with PCM: an up to date introduction into basics and applications*

[17]   Gil A, Ferna A I, Cabeza L F, Olives R, Py X, Navarro M E and Martı M 2012 Solar Energy Materials & Solar Cells Selection and characterization of recycled materials for sensible thermal energy storage **107** 131–5

[18]   Abedin A H and Rosen M A 2011 A Critical Review of Thermochemical Energy Storage Systems 42–6

[19]   Abedin A H 2010 Thermochemical Energy Storage Systems : Modelling , Analysis and Design By

[20]   N'Tsoukpoe K E, Liu H, Le Pierrès N and Luo L 2009 A review on long-term sorption solar energy storage *Renew. Sustain. Energy Rev.* **13** 2385–96

[21]   Bombač U 2014 Description and Analysis of Adsorption Heat Storage Device **60** 619–28

[22]   Sciuto Giacomo 2012 Innovative Latent Heat Thermal Storage Elements Design based on Nanotechnologies 145

[23]   Zalba B, Marín J M, Cabeza L F and Mehling H 2003 *Review on thermal energy storage with phase change : materials , heat transfer analysis and applications* vol 23

[24]   Liu M, Saman W and Bruno F 2012 Review on storage materials and thermal performance enhancement techniques for high temperature phase change thermal storage systems *Renew. Sustain. Energy Rev.* **16** 2118–32

[25]   Tamme R, Taut U, Streuber C and Kalfa H 1991 Energy storage development for solar thermal processes *Sol. Energy Mater.* **24** 386–96

[26]   Lopez J, Caceres G, Palomo Del Barrio E and Jomaa W 2010 Confined melting in deformable porous media: a first attempt to explain the graphite/salt composites behaviour *Int. J. Heat Mass Transf.* **53** 1195–207

[27]   Pincemin S, Olives R, Py X and Christ M 2008 Highly conductive composites made of phase change materials and graphite for thermal storage *Sol. Energy Mater. Sol. Cells* **92** 603–13

[28]   Nomura T, Okinaka N and Akiyama T 2010 Technology of latent heat storage for high temperature application: a review *ISIJ Int.* **50** 1229–39

[29]   Zhao C Y and Wu Z G 2011 Heat transfer enhancement of high temperature thermal energy storage using metal foams and expanded graphite *Sol. Energy Mater. Sol. Cells* **95** 636–43

[30]   Wu Z G and Zhao C Y 2011 Experimental investigations of porous materials in high temperature thermal energy storage systems *Sol. Energy* **85** 1371–80

[31]   Zhao C Y and Zhang G H 2011 Review on Micro-encapsulated Phase Change Materials (MEPCMs): Fabrication , Characterization and Applications **15** 3813–32

[32]   Adinberg R, Zvegilsky D and Epstein M 2010 Heat transfer efficient thermal energy storage for steam generation *Energy Convers. Manag.* **51** 9–15

[33]   Anon 1999 High temperature thermal energy storage an experimental study **9** 9–15

[34]   Shabgard H, Bergman T L, Sharifi N and Faghri A 2010 International Journal of Heat and Mass Transfer High temperature latent heat thermal energy storage using heat pipes *Int. J. Heat Mass Transf.* **53** 2979–88

[35]   Farid M M and Kansawa A 1989 Thermal performance of a heat storage module using PCM's with different melting temperatures: mathematical modeling *J. Sol. Energy Eng.* **111** 152–7

[36]   Farid M, Kim Y and Kansawa A 1990 Thermal performance of a heat storage module using PCM's with different melting temperature: experimental *J. Sol. Energy Eng.* **112** 125–31

[37]   Adine H A and El Qarnia H 2009 Numerical analysis of the thermal behaviour of a shell-and-tube heat storage unit using phase change materials *Appl. Math. Model.* **33** 2132–44

[38]   Carslaw S H and Jaeger J C *Conduction of Heat in Solid* ed Clarendon (Oxford)

[39]   Hashemi H T and Sliepcevich C M 1994 A numerical method for solving two-dimensional problems of heat conduction with change of phase *Chem. Eng. Prog. Symp. Ser.* **63** 34–41

[40]   Comini G, Del Guidice S, Lewis R W and Zienkiewicz O C 1974 Finite element solution of non-linear heat conduction problems with special reference to phase change *Int. J. Numer. Meth. Eng* **8** 613–24

[41]   Poirier D and Salcudean M 1988 On numerical methods used in mathematical modeling of phase change in liquid metals *Trans. ASME J. Heat Transf.* **110** 562–70

[42]   Gil A, Oró E, Peiró G, Álvarez S and Cabeza L F 2013 Material selection and testing for thermal energy storage in solar cooling *Renew. Energy* **57** 366–71

[43]   Sharma S D and Sagara K 2005 Latent Heat Storage Materials and Systems: A Review *Int. J. Green Energy* **2** 1–56

[44]   Gallego a. J, Ruíz-Pardo a., Cerezuela-Parish a., Sánchez J, Martín-Macareno C, Cabeza L F, Camacho E F and Oró E 2013 Mathematical modeling of a PCM storage tank in a solar cooling plant *Sol. Energy* **93** 1–10

[45]   Longeon M, Soupart A, Fourmigué J, Bruch A and Marty P 2013 Experimental and numerical study of annular PCM storage in the presence of natural convection *Appl. Energy* **112** 175–84

[46]   Ismail K A R, Grac M and Silva E 2003 Numerical solution of the phase change problem around a horizontal cylinder in the presence of natural convection in the melt region **46** 1791–9

[47]   Agyenim F, Hewitt N, Eames P and Smyth M 2010 A review of materials , heat transfer and phase change problem formulation for latent heat thermal energy storage systems (LHTESS) **14** 615–28

[48]   Dubovsky V, Ziskind G and Letan R 2011 Analytical model of a PCM-air heat exchanger *Appl. Therm. Eng.* **31** 3453–62

[49]   Castell A, Solé C, Medrano M, Roca J, Cabeza L F and García D 2008 Natural convection heat transfer coefficients in phase change material (PCM) modules with external vertical fins *Appl. Therm. Eng.* **28** 1676–86

[50]   Khalifa A, Tan L, Date A and Akbarzadeh A 2014 A numerical and experimental study of solidi fi cation around axially fi nned heat pipes for high temperature latent heat thermal energy storage units *Appl. Therm. Eng.* **70** 609–19

[51]   Zhang Y and Khalifa A 1996 Heat transfer enhancement in latent heat thermal energy storage system by using the internally finned tube *Int. J. Heat Mass Transf.* **39** 3165–73

[52]   Mehling H, Hiebler S and Ziegler F 2000 Latent Heat Storage using a PCM-graphite Composite Material *Terrastock 2000, 8th Int. Conf. Therm. Energy Storage* 375–80

[53]   Gil A, Barreneche C, Moreno P, Solé C, Inés Fernández a. and Cabeza L F 2013 Thermal behaviour of d-mannitol when used as PCM: Comparison of results obtained by DSC and in a thermal energy storage unit at pilot plant scale *Appl. Energy* **111** 1107–13

[54]   Barreneche C, Gil A, Sheth F, Inés Fernández a. and Cabeza L F 2013 Effect of d-mannitol polymorphism in its thermal energy storage capacity when it is used as PCM *Sol. Energy* **94** 344–51

[55]   Burger A, Henck J O, Hetz S, Rollinger J M, Weissnicht A a. and Stöttner H 2000 Energy/temperature diagram and compression behavior of the polymorphs of D-mannitol *J. Pharm. Sci.* **89** 457–68

[56]   Bruni G, Berbenni V, Milanese C and Girella a 2009 Physico-chemical characterization of anhydrous D-mannitol *J. Therm. nalysis Calorimetrynalysis Calorim.* **95** 871–6

[57]   Kumaresan G, Velraj R and Iniyan S 2011 Thermal Analysis of D-mannitol for Use as Phase Change Material for Latent Heat Storage *J. Appl. Sci.* **11** 3044–8

[58]   Dow Company Syltherm800 - product brochure 1–28

[59]   Samara F, Groulx D and Biwole P H 2012 Natural Convection Driven Melting of Phase Change Material: Comparison of Two Methods *COMSOL Conf.* 1–8

[60]   Medrano M, Yilmaz M O, Nogués M, Martorell I, Roca J and Cabeza L F 2009 Experimental evaluation of commercial heat exchangers for use as PCM thermal storage systems *Appl. Energy* **86** 2047–55

[61]   Rahimi M, Ranjbar A A, Ganji D D, Sedighi K and Hosseini M J 2014 Experimental Investigation of Phase Change inside a Finned-Tube Heat Exchanger **2014**

[62]   Rahimi M, Ranjbar A A, Ganji D D, Sedighi K, Hosseini M J and Bahrampoury R 2014 Analysis of geometrical and operational parameters of PCM in a fin and tube heat exchanger *Int. Commun. Heat Mass Transf.* **53** 109–15

[63]   Anon The Heat Transfer Module User's Guide

[64]   Rolander N, Rambo J, Joshi Y, Allen J K and Mistree F 2006 An Approach to Robust Design of Turbulent Convective Systems *J. Mech. Des* **128** 844–55

[65]   Buddhi D 1977 *Thermal performance of a shell and tube PCM storage heat exchanger for industrial waste heat recovery*

[66]   Trp A, Lenic K and Frankovic B 2006 Analysis of the influence of operating conditions and geometric parameters on heat transfer in watereparaffin shell-andtube latent thermal energy storage unit *Appl. Therm. Eng.* **26**

[67]   Morcos V 1990 Investigation of a latent heat thermal energy storage system. *Sol. Wind Technol* **7** 197–202

[68]   Hosseini M J, Rahimi M and Bahrampoury R 2014 Experimental and computational evolution of a shell and tube heat exchanger as a PCM thermal storage system *Int. Commun. Heat Mass Transf.* **50** 128–36

[69]   Agyenim F, Eames P and Smyth M 2009 A comparison of heat transfer enhancement in a medium temperature thermal energy storage heat exchanger using fins *Sol. Energy* **83** 1509–20

[70]   Agyenim F, Eames P and Smyth M 2010 Heat transfer enhancement in medium temperature thermal energy storage system using a multitube heat transfer array *Renew. Energy* **35** 198–207

[71]   Kakaç S and Liu H 2002 *Heat exchangers: Selection, Rating and Thermal Design* ed C P LLC

[72]   Jesumathy S P, Udayakumar M and Suresh S 2012 Heat transfer characteristics in latent heat storage system using paraffin wax † **26** 14–6

[73]   Wang Y, Amiri A and Vafai K 1999 An experimental investigation of the melting process in a rectangular enclosure **42**

[74]   KERN D Q 1950 *Process Heat Transfer* (McGraw-Hill)

[75]   Solé A, Neumann H, Niedermaier S, Martorell I, Schossig P and Cabeza L F 2014 Stability of sugar alcohols as PCM for thermal energy storage *Sol. Energy Mater. Sol. Cells* **126** 125–34

[76]   Eck M, Zarza E, Eickhoff M, Rheinländer J and Valenzuela L 2003 Applied research concerning the direct steam generation in parabolic troughs *Sol. Energy* **74** 341–51

[77]   Bayón R, Rojas E, Valenzuela L, Zarza E and León J 2010 Analysis of the experimental behaviour of a 100 kW th latent heat storage system for direct steam generation in solar thermal power plants *Appl. Therm. Eng.* **30** 2643–51

[78]   Markus E, Zarza E, Eickhoff M, Rheinländer J and Valenzuela L 2003 Applied research concerning the direct steam generation in parabolic troughs *Sol. Energy* **74** 341–51

[79]   Eduardo Z, Valenzuela L, Leon J, Hennecke K, Eck M, Weyers H D and Eickhoff M 2004 Direct steam generation in parabolic troughs: Final results and conclusions of the DISS project *Energy* **29** 635–44

[80]   Cárdenas B and León N 2014 Latent heat based high temperature solar thermal energy
         storage for power generation *Energy Procedia* **57** 580–9

[81]   Galione P A, Pérez-segarra C D, Rodríguez I, Oliva A and Rigola J 2015 Multi-layered
         solid-PCM thermocline thermal storage concept for CSP plants . Numerical analysis and
         perspectives *Appl. Energy* **142** 337–51

[82]   Galione P a, Lehmkuhl O, Rigola J and Oliva a 1991 Numerical simulations of thermal
         energy storage systems with phase change materials

[83]   Galione P, Pérez-segarra C, Rodríguez I, Torras S and Rigola J 2015 Numerical evaluation
         of multi-layered solid-PCM thermocline-like tanks as thermal energy storage systems for
         CSP applications *Energy Procedia* **69** 832–41

[84]   Rodrıguez I 2015 Multi-layered solid-PCM thermocline thermal storage for CSP .
         Numerical evaluation of its application in a 50 MWe plant **119** 134–50

[85]   Goswami Y and Florida S 2011 Development of Low Cost Industrially Scalable PCM
         Capsules for Thermal Energy Storage in CSP Plants

[86]   Laing D, Bahl C, Bauer T and Lehmann D 2011 Thermal energy storage for direct steam
         generation *Sol. Energy* **85** 627–33

[87]   Tawfeic S R 2013 BOILER DRUM-LEVEL MODELING *J. Eng. Sci.* 1812–29

[88]   Tan W, Marquez H J, Tongwen C and Jizhen L 2005 Analysis and control of a nonlinear
         boiler-turbine unit *J. Process Control* **15** 883–91

[89]   Tan W, Fang F, Tian L, Fu C and Liu J 2008 Linear control of a boilerturbine unit:
         Analysis and design *ISA Trans.* **47** 189–97

[90]   Kim E G 1990 Control system design of boiler drum level *Proc. ISL winter Work.* **3** 43–54

[91]   Fu C, Liu J and Tan W 2004 Robust PI design for a benchmark nonlinear boiler *5th Asian
         Control Conf.* **1** 304–8

[92]   Hèctor G C, Alfredo C D, Jose A R and Palazoglu A 1995 Variable Structure Control with
         a Second Order Sliding Condition: Application to a steam generator *Automatica* **31** 1157–
         68

[93]   Li B, Chen T, Li D Y, Chen T and Yang D 2005 A computer program for simulation of
         controlled circulation boiler and natural circulation boiler start up behavior *Energy
         Convers. Manag.* **46** 533–49

[94]   Heimo W 2007 Dynamic simulation of natural circulation steam generators with the use of
         finite-volume-algorithms – A comparison of four algorithms *Simul. Model. Pract. Theory*
         15 565–88

[95]   Adam E J and Marchetti J L 1999 Dynamic simulation of large boilers with natural
         recirculation *Comput. Chem. Eng.* **23** 1031–40

[96]   Zhang M H, Chu K W, Wei F and Yu A B 2008 CFD–DEM study of the cluster behavior
         in riser and downer reactors *Powder Technol.* **184** 151–65

[97]   Emara-Shabaik H E, Habib M A and Al-Zaharna I 2008 Prediction of risers tubes
        temperature in water tube boiler *Appl. Math. Model.* **33** 1323–36

[98]   Kim H and Choi S 2005 model on water level dynamics in natural circulation drum-type
        boiler *Int. Commun. Heat Mass Transf.* **32** 768–96

[99]   Bell R D and Åström K J 2000 Drum-boiler dynamics *Automatica* **36** 363–78